
THE ASEAN

JOURNAL OF RADIOLOGY

Highlight

- Original Article
- Case Report
- Pictorial Essay
- ASEAN Movement in Radiology
- Memorial

Official Journal of The



Royal College of Radiologists of Thailand



Radiological Society of Thailand



Foundation for Orphan and Rare Lung Disease



Thai Society of Vascular and Intervention Radiology



ASEAN Association of Radiology

ASEAN
JOURNAL OF RADIOLOGY

ISSN 2672-9393



The ASEAN Journal of Radiology

Editor:	<i>Wiwatana Tanomkiat, M.D.</i>
Associate Editors:	<i>Pham Minh Thong, M.D., Ph.D.</i> <i>Narufumi Suganuma, M.D., Ph.D.</i> <i>Kwan Hoong Ng, Ph.D.</i> <i>Shafie Abdullah, M.D.</i> <i>Siriporn Hirunpat, M.D.</i> <i>Chang Yueh Ho, M.D.</i> <i>Maung Maung Soe, M.D.</i> <i>Kyaw Zaya, M.D.</i>
Assistant Editor:	<i>Nucharin Supakul, M.D.</i>
Statistical Consultant:	<i>Alan Frederick Geater, B.Sc., Ph.D.</i>
Language Consultant:	<i>Siriprapa Saparat, EIL</i>
Publishing Consultant:	<i>Ratchada Chalarat, M.A.</i>
Editorial Coordinator:	<i>Supakorn Yuenyongwannachot, B.A., M.Sc.</i>
Graphics:	<i>Kowa Saeooi, B.A.</i>
Publisher:	<i>Foundation for Orphan and Rare Lung Disease</i>

CONTENTS

77

From The Editor

Returning to the pre-pandemic situation but still in the years of infections
Wiwatana Tanomkiat, M.D.

80

Original Article

The preoperative factors associated with underestimation of invasive breast cancer in stereotactic vacuum-assisted biopsy-diagnosed DCIS patients
Somchanin Pipatpajong, M.D.
Rachata Tangkulboriboon, M.D.

98

Factors related to bone mineral density in female patients receiving TSH-suppressive doses of levothyroxine for thyroid cancer

Araya Boonyaleepan M.D.
Tarit Taerakul M.D.

122

Comparative study of setup errors between new and reused thermoplastic masks in irradiated head and neck cancer patients

Nipha Chumsuwan, Ph.D.
Lalita Romkedpikun, B.Sc.
Janyaporn Thongthae, B.Sc.
Tanapan Yousuk, B.Sc.

137

Acute changes of superior mesenteric artery pressure after intraarterial bolus injection of prostaglandin-E1

Yukihiro Hama, M.D., Ph.D.

146

Case Report

Superficial siderosis presenting as hemiparesis in a paediatric patient with congenital Factor V deficiency – A case report

Pushkar Mendiratta, M.D., D.N.B.
Samaresh Sahu M.D., D.N.B., F.R.C.R., M.N.A.M.S.
Aneesh Mohimen, M.D., D.M.

155

Pictorial Essay

Pediatric imaging of neuroblastoma-From classic to atypical

Michal Scolnik, M.D.
Luda Glozman M.D.
Noa Mandel-Shorer, M.D.
Michalle Soudack Ben-Nun M.D.
Anat Ilivitzki, M.D.

180

ASEAN Movement in Radiology

Tuberculosis: Important lessons from AOCR 2023, Bangkok, Thailand

Mimi Pakkal, M.D.
Bushra Johari, M.D.
Jin Mo Goo, M.D., Ph.D.
Ki Yeol Lee, M.D., Ph.D.
Kushaljit Singh Sodhi, M.D.
Murali Krishna, M.D.
Wiwatana Tanomkiat, M.D.

199

Memorial

Professor Emeritus Chaleow Piyachon, 1938-2023

From The Editor

Returning to the pre-pandemic situation but still in the years of infections



Received 28 August 2023 ; accepted 24 August 2023
doi:10.46475/aseanjr.v24i2.874

The editor visited Honorary Professor Doctor Ng Kwan Hoong at the exhibition "From Darkness to Clarity: The Evolution of Medical Imaging Through Emeritus Professor Dr. Ng Kwan Hoong's Innovation" held during 7 June-7 August 2023 to honor him at TJ Danarag Medical Library, Universiti Malaya, Kuala Lumpur, Malaysia. Professor Ng is one of the remarkable medical physicists and in the editorial board of The ASEAN Journal of Radiology.

In the aftermath of the Songkran celebrations in Thailand, which concluded on 15 April 2023, the number of Covid-19 inpatients and related deaths has seen a significant increase of 150% in just one week [1,2]. Similarly, COVID infections in Japan increased threefold after the government had eased restrictions on 8 May. However, in June, new COVID-19 infections in Thailand and other countries steadily fell, with fewer fatalities [3]. Death mainly occurs in the 607 group which includes patients over the age of 60 and those living with at least one of the seven chronic diseases. A key risk factor is either not having been vaccinated at all, not having received a booster jab or having received a booster for over three months. Having attended Japan Radiology Congress (JRC) in Yokohama, Japan in April, Eurasia Radiological Forum (EARF) in Astana, Kazakhstan in June, Malaysian Congress of Radiology (MCoR) in Kuala Lumpur, Malaysia in July, and the Vietnamese Society of Radiology and Nuclear Medicine (VSRNM) in Da Nang, Vietnam in August, I perceived the return to the pre-COVID normal situation in those cities and the conferences in which there was no social distancing in both academic and social events. In addition, attendants were not required to wear face masks. People gathered to talk, drink, dine and sing as they did before the pandemic.



Professor Pham Minh Thong, his family, and the editor at the Gala Dinner of VSRNM on 25 August 2023. Professor Pham Minh Thong is the president of VSRNM and in the editorial board of The ASEAN Journal of Radiology.

Infections remain the rising health issue. From January to August 2023, the Ministry of Public Health of Thailand revealed that the cumulative total of dengue fever cases rose to 65,552, while the cumulative death toll is 58, of which 40 were older children and adults. Death mainly occurs because dengue fever patients often do not think they have caught this disease early on and take nonsteroidal anti-inflammatory drugs (NSAIDs) such as aspirin and ibuprofen to reduce fever, but this leads to easy bleeding with a risk developing dengue shock syndrome [4]. On 14 August, Thailand reported its first monkey pox-related fatality, in a man who was also infected with HIV and syphilis. There had been a total of 189 monkey pox cases reported in Thailand in 161 Thais and 28 foreigners, 82 of whom were also infected with HIV [5].

Thailand lost its famous radiologist, Professor Emeritus Chaleow Piyachon, on 27 May 2023. One of the text books written by Professor Piyachon on emergency

radiology I read when I was a medical student in 1991, the year it was published, is one of my inspirations to become a radiologist. It is thin but clear and eye-opening. Our memory of his is commemorated in this issue.

Wiwatana Tanomkiat, M.D.
Editor,
The ASEAN Journal of Radiology
Email: aseanjournalradiology@gmail.com

References

1. The Tiger [Internet]. Bangkok: Thailand News; c2023 [cited 2023 Aug 28]. Thailand News Covid-19 inpatients and deaths surge by 150% in Thailand after Songkran celebrations. Available from: <https://thethaiger.com/news/national/covid-19-inpatients-and-deaths-surge-by-150-in-thailand-after-songkran-celebrations>
2. Thai PBS World [Internet]. Bangkok: Thailand's Public Broadcasting Service; c2018 [cited 2023 Aug 28]. COVID-19 infections on the rise with 1,811 cases and 10 deaths last week. Available from: <https://www.thaipbsworld.com/covid-19-infections-on-the-rise-with-1811-cases-and-10-deaths-last-week/>
3. Thai PBS World [Internet]. Bangkok: Thai Public Broadcasting Service; c2018 [cited 2023 Aug 28]. COVID infections falling steadily, fewer fatalities over past month. Available from: <https://www.thaipbsworld.com/covid-infections-falling-steadily-fewer-fatalities-over-past-month/>
4. ThaiNewsroom.com [Internet]. Bangkok: Thai News Room; 2023 [cited 2023 Aug 28]. Dengue Fever Cases Climb To 5,000-6,000 A Week. Available from: <https://thainewsroom.com/2023/08/18/dengue-fever-cases-climb-to-5000-6000-a-week/>
5. Thai PBS World [Internet]. Bangkok: Thai Public Broadcasting Service; c2018 [cited 2023 Aug 28]. Thailand's first monkey pox related death reported. Available from: <https://www.thaipbsworld.com/thailands-first-monkey-pox-related-death-reported/>

Original Article

The preoperative factors associated with underestimation of invasive breast cancer in stereotactic vacuum-assisted biopsy-diagnosed DCIS patients

Somchanin Pipatpajong, M.D. ⁽¹⁾

Rachata Tangkulboriboon, M.D. ⁽²⁾

From ⁽¹⁾Department of Radiology, Faculty of Medicine, Chulalongkorn University, Bangkok, Thailand.

⁽²⁾Department of Radiology, King Chulalongkorn Memorial Hospital, The Thai Red Cross Society, Bangkok, Thailand.

Address correspondence to S.P. (e-mail: somchanin.p@chula.ac.th)

Received 22 April 2023; revised 2 July 2023; accepted 2 July 2023
doi:10.46475/aseanjr.v24i2.778

Abstract

Objective: To determine preoperative factors associated with underestimation of invasive breast cancer, where stereotactic vacuum-assisted biopsy (VAB) diagnosed as ductal carcinoma in situ (DCIS).

Materials and Methods: Data from 95 patients diagnosed with DCIS by stereotactic VAB, including their clinical, radiological, and pathological findings between November 2010 and May 2021, were analyzed retrospectively. The clinical, radiological, and pathological features were analyzed.

Results: The underestimation rate was 30.5 %. Three preoperative features were significantly associated with the underestimation of invasive breast cancer in multivariable analysis, including palpability (OR, 11.51; 95% CI: 1.817-72.897;

P = 0.009), BI-RADS category (OR, 3.705; 95% CI: 1.214-11.303; P = 0.021), and visibility of a mammographically detected lesion at ultrasonography (OR, 7.115; 95% CI: 1.977-25.611; P = 0.003). The calcification morphology was statistically significant in an univariable analysis but not in a multivariable analysis.

Conclusion: Preoperative variables significantly associated with underdiagnosis of invasive breast cancer, including palpability, BI-RADS category, and visibility of mammographically detected lesions at ultrasonography, could aid in assessing the risk of developing invasive breast cancer and conducting treatment selection.

Keywords: Breast cancer, Ductal carcinoma in situ, Stereotactic vacuum-assisted biopsy, Underestimation.

Introduction

Ductal carcinoma in situ (DCIS) of the breast is a pathological entity where malignant cells originate from and line within the breast ducts without evidence of invasion. This entity is a non-obligate precursor of invasive breast cancer. Three-fourths of patients with DCIS lesions presented with breast calcifications. Up to 23 percent had a breast mass or asymmetry, and roughly 12 percent were associated with a palpable abnormality [1]. The standard treatment for patients with a biopsy-confirmed diagnosis of DCIS is lumpectomy with radiation or total mastectomy. A sentinel lymph node biopsy (SLNB) should be considered for mastectomy or lumpectomy, of which the anatomic location likely compromises the performance of a future SNLB [2].

Diagnosis of DCIS by biopsy potentially leads to an underestimate of invasive breast cancer in subsequent surgical excision. The reported underestimation rates varied from 14.1-42.7 percent [3-7]. The one from a meta-analysis was 25.9 percent (95% confidence interval (CI): 22.5-29.5), indicating the considerable number of patients with invasive breast cancer being undertreated [3].

Several studies have sought to identify factors associated with DCIS lesion upstaging to invasive cancer following surgical excision [3-7]. The most frequently reported risk factors for underestimation were palpability, histologic grading, biopsy device, and some radiological features, e.g., lesion size, mass on mammogram or ultrasonogram, and the Breast Imaging Reporting and Data System (BI-RADS) score. However, there is a paucity of reported data on radiological features which composed BI-RADS scores.

The gold standard procedure for tissue diagnosis is excisional biopsy. This procedure is generally costly and associated with morbidity, so other less invasive interventions should be considered [8,9]. Vacuum-assisted biopsy (VAB) is an alternative intervention to obtain some tissue of mammographically detected lesions, especially microcalcifications. The VAB procedure was considered safe and cost-effective compared to the surgical biopsy. VAB also provided high-quality specimens and low rates of false-negative results [8,9]. The reported underestimation rate for VAB was 6.1-29.0 percent [8-13].

Our study aimed to identify the preoperative factors associated with underestimated invasive breast cancer and estimate the extent of this underestimation at King Chulalongkorn Memorial Hospital.

Materials and methods

Patient

The King Chulalongkorn Memorial Hospital institutional review board, has approved the study and waived the informed consent process.

We used data from the hospital systems of King Chulalongkorn Memorial Hospital, including the Hospital Information System (HIS), the Radiological Information System (RIS), and the Picture Archiving and Communication System (PACS). A total of 136 female patients had been diagnosed with any subtype of

DCIS by VAB. It subsequently underwent breast surgery of either wide excision or mastectomy, irrespective of sentinel lymph node biopsy (SLNB) at the hospital on 1 November 2010 and 31 May 2021, were identified. Of those patients, 41 patients were excluded due to the following criteria- unavailable or inconclusive pathological data [22], multifocal or multicentric DCIS by VAB [13], and the longer-than-90-day interval between biopsy and surgery [3] and between mammography and biopsy [2]. Thus, 95 patients (mean age \pm standard deviation, 53.9 ± 10.9) were included in the study (Figure 1). Clinical data with radiological and pathological findings were then collected and reviewed (Table 1).

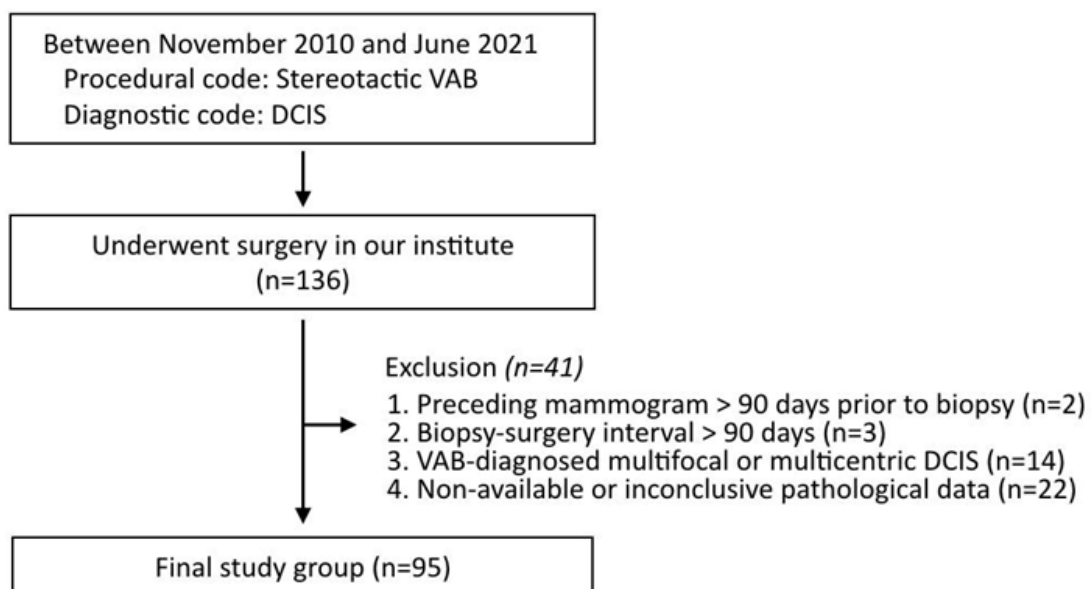


Figure 1. Flowchart of patient selection.

The radiologists performed stereotactic VABs, using either a 9- or 10-gauge vacuum-assisted device (Mammotome; Ethicon-Endosurgery, Cincinnati, OH). Patients with a longer-than-90-day interval between mammography and biopsy, VAB-diagnosed multifocal or multicentric DCIS, and unavailable or inconclusive pathological data were excluded.

Table 1. *Data collection.*

Clinical data	Radiological findings	Histological findings
Age	Morphology	DCIS,
Presentations	Distribution	DCIS with microinvasion
Mass characteristics	Amount of calcification	Invasive breast cancer
Previous history of breast cancer	Presence of mass	DCIS grading
	Architectural distortion	
	Asymmetry	
	Skin Retraction	
	Nipple retraction	
	Axillary lymphadenopathy	
	Ultrasonographic visibility	
	BI-RADS score	

The underestimated invasive breast cancer was defined as identifying the invasive part in subsequent surgical excision. Microinvasive carcinoma was defined as any foci of cancer cells sized in 1 millimeter or less infiltrating into the stroma. This microinvasion subtype was not classified as an underestimation as it was treated the same as others with pure DCIS [2, 14].

Two researchers independently reviewed the imaging findings. All clinical and histopathological data were blinded during the review to prevent bias. In case of disagreement between the two researchers, a consensus was made.

Statistical analysis

All variables were compared between the non-underestimation and underestimation groups, using Pearson's Chi-square or Fisher's exact test for categorical variables and Student's t-test for continuous ones.

Univariate analyses were initially performed to identify determinants of the underestimation. The statistically significant variables (P-value of less than 0.05) in

the univariate analyses were then included in the multivariate analysis. Backward stepwise regression was used to gradually eliminate variables from the regression model to find a reduced model that best explains the data. All statistical analyses were performed using SPSS Statistics version 22.0 (IBM, Armonk, NY). P-values of less than 0.05 was considered statistically significant.

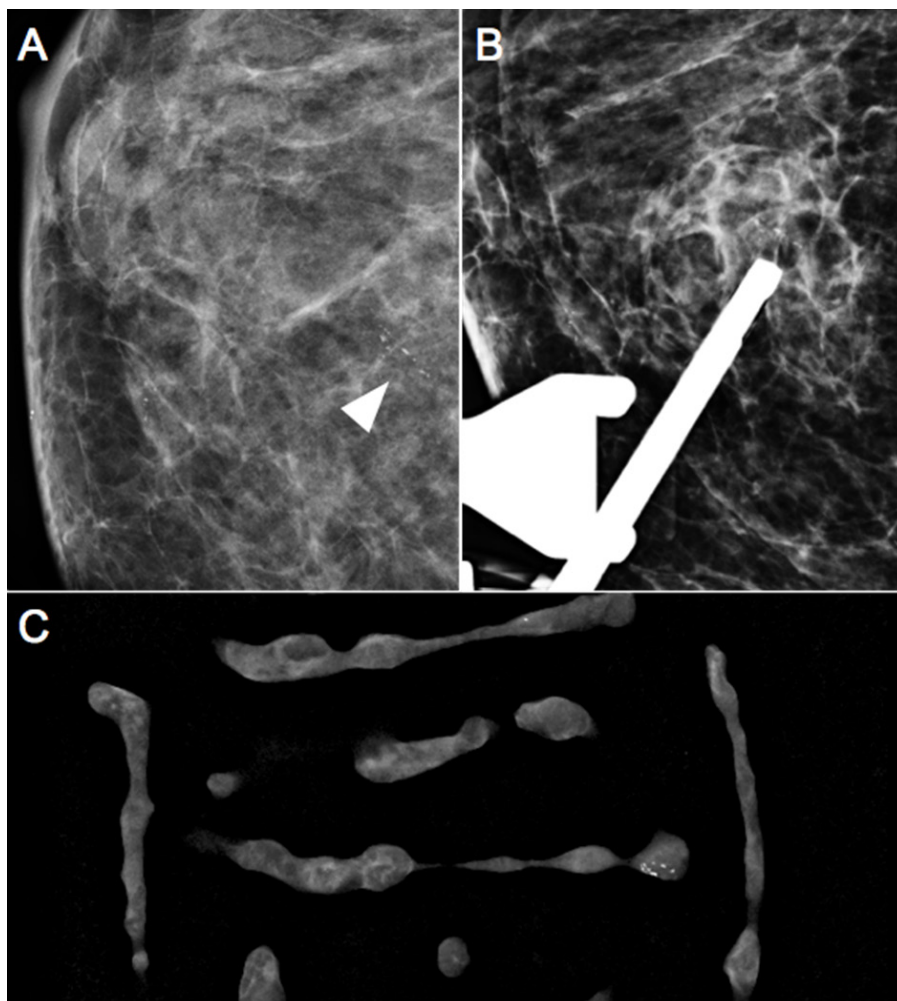


Figure 1. Screening mammogram (A) of a 68-year-old patient shows fine-linear microcalcifications in a linear distribution at the right central region: pre-biopsy image (B) and specimengraphy (C) obtained during stereotactic 9G VAB. High-grade DCIS was identified on pathology. Following that, a wide excision was performed, and histology confirmed IDC.

Results

Patient characteristic

The baseline characteristics are summarized in Table 2. Twenty-nine of 95 patients with VAB-diagnosed DCIS had invasive breast cancer on the surgical excision and were included in the underestimated group, accounting for 30.5% of the underestimation rate. Almost all patients in this underestimated group were diagnosed with DCIS with invasive ductal carcinoma at the excision pathology, except the only patient diagnosed with DCIS with invasive lobular carcinoma. Sixty-six patients were included in the non-underestimated group, 62 with pure DCIS and 4 with DCIS with microinvasion, which was also included in the non-underestimated group because the treatment and follow-up were the same as pure DCIS.

Of the 95 DCIS diagnoses at stereotactic VAB, there are 79 (83.2%) with screening mammograms, 16 (16.8%) with symptoms, 9 (9.5%) with a palpable lesion, and 20 (21.1%) with history of breast cancer. Most tissue pathology from stereotactic VAB was DCIS with intermediate grade (55.8%) and not specified (24.2%). The collection of the comedo subtype was initially intended; however, the majority of pathological reports did not include information on the comedo subtype. As a result, the comedo subtype is not reported in this article. Following the biopsies, 71 DCIS patients (74.7%) underwent surgical excision without SLNB. Of the underestimated group, 20 (69.0%) underwent surgical excision without SLNB.

Table 2. Baseline patient characteristics in the included patients.

Baseline characteristic	All (n = 95)	Underestimated invasive breast cancer		P value
		No (n = 66)	Yes (n = 29)	
Age (y)*	53.93±10.9 (33-76)	54.0±10.8 (33-76)	53.7±10.9 (35-75)	0.470
Age categories				0.275
< 45	21 (22.1)	13 (19.7)	8 (27.6)	
≥ 45	74 (77.9)	53 (80.3)	21 (72.4)	
Presentation				0.063
Screening	79 (83.2)	58 (87.9)	21 (72.4)	
Symptoms	16 (16.8)	8 (12.1)	8 (27.6)	
Palpability				0.003
No	86 (90.5)	64 (97.0)	22 (75.9)	
Yes	9 (9.5)	2 (3.0)	7 (24.1)	
History of breast cancer				0.407
No	75 (78.9)	53 (80.3)	22 (75.9)	
Yes	20 (21.1)	13 (19.7)	7 (24.1)	
Grade at VAB				0.816
Low	13 (13.7)	9 (13.6)	4 (13.8)	
Intermediate	53 (55.8)	33 (50.0)	20 (69.0)	
High	11 (11.6)	8 (12.1)	3 (10.3)	
Not specified	23 (24.2)	16 (24.2)	7 (24.1)	
Type of surgery				0.239
Wide excision	40 (42.1)	32 (48.5)	8 (27.6)	
Wide excision with SLND	3 (3.2)	2 (3.0)	1 (3.4)	
Mastectomy	31 (32.6)	19 (28.8)	12 (41.4)	
Mastectomy with SLND	21 (22.1)	13 (19.7)	8 (27.6)	

Data are means ± standard deviations.

Radiographic features

Table 3 shows the radiologic findings of all DCIS patients. All of them had any suspicious morphology of calcification, of which the majority were non-linear (86.3%). Grouped calcification was the most common, followed by segmental and linear calcification. This sequence of the distribution was indifferent between the non-underestimated and underestimated groups. Other radiological findings were rarely discovered, including architectural distortion (3.2%), focal asymmetry (2.1%), skin retraction (1.1%), nipple retraction (1.1%), and axillary lymphadenopathy (1.1%). In addition, mass, skin thickening, or trabecular thickening were radiologically undetected. The distribution of the BI-RADS category was 4.2% BI-RADS 4a, 47.4% BI-RADS 4b, 38.9% BI-RADS 4c, and 9.5% BI-RADS 5. 18 (18.9%) of all DCIS patients had visibility of the lesion at ultrasonography. The DCIS patients were equally concentrated between the BI-RADS 4A/4B and 4C/5. The BI-RADS distribution was different between the two groups; the non-underestimated group was likely to have a result of BIRADS 4A/4B, whereas the other group was otherwise. Any lesions were ultrasonographically visible in 18 DCIS patients (18.9%). The differences in calcification morphology, BI-RADS, and ultrasonographic visibility between the two groups were significant.

The features with the rate of the most significant difference in the underestimated group compared with the rate in the non-underestimated group were palpable lesion, fine linear/fine-linear branching calcification, BI-RADS 4c and 5, and visibility of the lesion at the US.

Table 3. Radiographic features.

Radiographic features	All (n = 95)	Underestimated invasive breast cancer		P value
		No (n = 66)	Yes (n = 29)	
Mass				
No	95 (100.0)	66 (100.0)	29 (100.0)	
Yes	0	0	0	
Morphology of calcification 0.002				
Non-linear group	82 (86.3)	62 (93.9)	20 (69.0)	
Fine linear/ fine-linear branching	79 (83.2)	58 (87.9)	21 (72.4)	
	13 (13.7)	4 (6.1)	9 (34.6)	
Distribution of calcification 0.120				
Diffuse	0	0	0	
Regional	0	0	0	
Grouped	66 (69.5)	49 (74.2)	17 (58.6)	
Linear	10 (10.5)	5 (7.6)	5 (17.2)	
Segmental	19 (20.0)	12 (18.2)	7 (24.1)	
Amount of calcification 0.173				
No comparison	45 (47.3)	31 (47.0)	14 (48.3)	
Newly developed	20 (21.1)	11 (16.7)	9 (34.6)	
Increased amount	30 (31.6)	24 (36.3)	6 (20.7)	
Architectural distortion 0.669				
No	92 (96.8)	64 (97.0)	28 (96.6)	
Yes	3 (3.2)	2 (3.0)	1 (3.4)	
Asymmetry 0.520				
None	93 (97.9)	65 (98.5)	28 (96.6)	
Asymmetry	0	0	0	
Global	0	0	0	
Focal	2 (2.1)	1 (1.5)	1 (3.4)	
Developing asymmetry	0	0	0	
Skin retraction 0.0695				
No	94 (98.9)	65 (98.5)	29 (100.0)	
Yes	1 (1.1)	1 (1.5)	0	
Nipple retraction 0.305				
No	94 (98.9)	66 (100.0)	28 (96.6)	
Yes	1 (1.1)	0	1 (3.4)	

Radiographic features	All (n = 95)	Underestimated invasive breast cancer		P value
		No (n = 66)	Yes (n = 29)	
Axillary lymphadenopathy				0.305
No	94 (98.9)	66 (100.0)	28 (96.6)	
Yes	1 (1.1)	0	1 (3.4)	
Skin thickening	0	0	0	
Trabecular thickening	0	0	0	
BI-RADS				<0.001
4a and 4b	49 (51.6)	42 (63.6)	7 (24.1)	
4c and 5	46 (48.4)	24 (36.3)	22 (75.9)	
Visibility of the lesion in the US				<0.001
No	77 (81.1)	61 (92.4)	16 (55.2)	
Yes	18 (18.9)	5 (7.6)	13 (44.8)	

Risk for underestimation

Table 4 shows the univariate and multivariate analysis results of the risk for underestimation. Morphology of calcification was a significant determinant of the underestimation in univariate analysis but not in multivariate analysis. In multivariable analysis, palpability (OR, 11.51; 95% CI: 1.817-72.897; P = 0.009), BI-RADS category (OR, 3.705; 95% CI: 1.214-11.303; P = 0.021), and visibility of a mammographically detected lesion at ultrasonography (OR, 7.115; 95% CI: 1.977-25.611; P = 0.003) were significantly associated with the underestimation.

Table 3. Radiographic features.

Patient and lesion characteristics	Analysis for underestimated breast cancer					
	Univariable analysis			Multivariable analysis		
	OR	95% CI	P value	OR	95% CI	P value
Age (y)*						
< 45	1					
≥ 45	0.644	0.233-1.777	0.395			
Presentation						
Screening	1					
Symptoms	2.762	0.920-8.295	0.070			
Palpability						
No	1			1		
Yes	10.182	1.966-52.722	0.006	11.510	1.817-72.897	0.009
History of breast cancer						
No	1					
Yes	1.297	0.456-3.687	0.625			
Morphology of calcification						
Non-linear	1			-	-	-
Fine linear/fine-linear branching	1.911	1.247-2.928	0.003	-	-	-
Distribution of calcification						
Grouped	1					
Linear	2.882	0.742-11.195	0.126			
Segmental	1.681	0.569-4.967	0.347			
BI-RADS						
4a & 4b (<50%)	1			1		
4c & 5 (≥ 50%)	5.500	2.049-14.763	<0.001	3.705	1.214-11.303	0.021
Visibility of the lesion in the US						
No	1			1		
Yes	9.912	3.079-31.910	<0.001	7.115	1.977-25.611	0.003

Discussion

Our analysis shows that the underestimation rate of invasive breast cancer among the patients with VAB-diagnosed DCIS was 30.5%, which is higher than the previously reported rates ranging from 11.2% to 18.0% [7,10,14]. This could be attributed to the initial implementation of the VAB technique at the hospital, where staff might not be highly experienced. It is also noted that ethnicity differs across these studies. A direct comparison between them should be made with caution. Other previous studies demonstrating various underestimation rates are incomparable because of different study populations or biopsy methods [3,4,5,6,8,11,12,15].

Preoperative risk factors for an underestimated diagnosis of invasive breast cancer comprised palpability, BIRADS category, and visibility of mammographically detected lesions on an ultrasound. These findings partly correspond with previous studies [3-5]. Palpability was reported as the risk factor in the earlier studies where the ultrasound-guided biopsy was included. Palpability or palpated mass could imply that the lesion is considerably large and thus likely to be invasive breast cancer. The presence of a mass more significant than 20 mm in size at imaging was significantly associated with the underestimation of invasive breast cancer in the prior studies [3, 4, 7].

BIRADS category was another reported factor in our study; the higher BIRADS scores had an increased likelihood of underestimating invasive breast cancer among patients with VAB-diagnosed DCIS compared to the lower ones [3,5]. It should be noted that our patients were classified into two groups – the group of 4A/4B, where the likelihood of being malignant is less than 50%, and the other group of 4C/5, where it is otherwise. This classification is unique as BIRADS 4 was not subcategorized elsewhere [3,5]. The last factor of visibility of mammographically detected lesions on ultrasound is strongly associated with the underestimation of invasive breast cancer in this study. Still, it is inconsistent with the meta-analysis, which included various biopsy methods and devices [3].

Despite no demonstrable association between distribution with the morphology of calcifications and underestimation of invasive breast cancer, the morphology of suspicious calcification and other features of calcification (e.g., distribution and increased amount/new development of suspicious calcification) give rise to a higher BI-RADS score on the radiologist consideration [14].

Age is not a predictor of an underestimated diagnosis of invasive breast cancer for our patients, similar to previous literature [3, 5, 7, 14]. In addition, we failed to demonstrate the association between certain mammographic features, including architectural distortion, asymmetry, skin and nipple retraction, axillary lymphadenopathy, and the risk of underestimation. However, those features are significantly associated with breast cancer [16,17]. A possible explanation could be the small number of patients in our study.

Four patients of DCIS with microinvasion were classified as pure DCIS and given the same management for DCIS, irrespective of microinvasion. These 4 cases were not an underestimated diagnosis of invasive breast cancer, different previously reported by Chan et al. [7].

The pathologic information of high nuclear grade of DCIS, including the comedo subtype of DCIS and any suspected microinvasive component, was another preoperative factor for underestimating invasive breast cancer in the earlier studies [3, 5]. Unfortunately, the analysis of this piece of information was not feasible for this study. This limitation arose from the non-specific report of nuclear grading in up to 24.2% of cases and the absence of information regarding the comedo subtype in the majority of pathological reports.

This study has some limitations. The data were retrospectively collected and analyzed in a single tertiary hospital. Our small sample size might affect the reliability of our results; some findings are not statistically significant as they would otherwise be due to lack of power. Our study's high underestimation rate might not reflect our current practice's quality. This could be attributed to the initial implementation of the VAB technique, potentially resulting in a lack of extensive

experience among the staff involved. Clinical data were not able to be verified due to retrospective data collection. For example, palpated mass might not be the same lesion where VAB was performed. Some pathological reports were not feasible to analyze due to non-specific results in nuclear grading and the absence of information regarding the comedo subtype, as described earlier.

Our study has crucial clinical implications. We have provided helpful clinical clues to the detection of invasive breast cancer in the patients who were diagnosed with DCIS by VAB. This could enable physicians to make sound judgments, preventing undertreatment and re-operation for those patients.

Conclusion

In conclusion, according to our retrospective analysis, invasive breast cancer was underdiagnosed by 30.5 % in VAB-diagnosed DCIS. Preoperative risk factors significantly associated with underestimated invasive breast cancer, including palpability, BI-RADS category, and visibility of mammographically detected lesions at ultrasonography, have been summarized. This could help physicians identify patients more likely to have invasive breast cancer when diagnosed with DCIS on VAB, as well as preoperative guide discussions regarding the risk of underdiagnosis and treatment alternatives, such as axillary procedure selection at the time of surgical excision or repeat biopsy.

References

1. Parikh U, Chhor CM, Mercado CL. Ductal carcinoma in situ: the whole truth. *AJR Am J Roentgenol* 2018;210:246-55. doi: 10.2214/AJR.17.18778.
2. NCCN Clinical Practice Guidelines in Oncology: Breast Cancer (Version 3.2019) [Internet]. NCCN;2019 Sept 6 [cited 2023 Jul 2]. Available from: https://www2.tri-kobe.org/nccn/guideline/archive/breast2019/english/breast_v3.pdf
3. Brennan ME, Turner RM, Ciatto S, Marinovich ML, French JR, Macaskill P, et al. Ductal carcinoma in situ at core-needle biopsy: meta-analysis of underestimation and predictors of invasive breast cancer. *Radiology* 2011; 260:119-28. doi: 10.1148/radiol.11102368.
4. Kim J, Han W, Lee JW, You JM, Shin HC, Ahn SK, et al. Factors associated with upstaging from ductal carcinoma in situ following core needle biopsy to invasive cancer in subsequent surgical excision. *Breast* 2012 ;21:641-5 . doi: 10.1016/j.breast.2012.06.012.
5. Meurs CJC, van Rosmalen J, Menke-Pluijmers MBE, Ter Braak BPM, de Munck L, et al. A prediction model for underestimation of invasive breast cancer after a biopsy diagnosis of ductal carcinoma in situ: based on 2892 biopsies and 589 invasive cancers. *Br J Cancer* 2018;119:1155-62. doi: 10.1038/s41416-018-0276-6.
6. Jakub JW, Murphy BL, Gonzalez AB, Connors AL, Henrichsen TL, Maimone S 4th, et al. A validated nomogram to predict upstaging of ductal carcinoma in situ to invasive disease. *Ann Surg Oncol* 2017;24:2915-24. doi: 10.1245/s10434-017-5927-y.
7. Chan MY, Lim S. Predictors of invasive breast cancer in ductal carcinoma in situ initially diagnosed by core biopsy. *Asian J Surg* 2010;33:76-82. doi: 10.1016/S1015-9584(10)60013-9.

8. Esen G, Tutar B, Uras C, Calay Z, İnce Ü, Tutar O. Vacuum-assisted stereotactic breast biopsy in the diagnosis and management of suspicious microcalcifications. *Diagn Interv Radiol* 2016;22:326-33. doi: 10.5152/dir.2015.14522.
9. Luparia A, Durando M, Campanino P, Regini E, Lucarelli D, Talenti A, et al. Efficacy and cost-effectiveness of stereotactic vacuum-assisted core biopsy of nonpalpable breast lesions: analysis of 602 biopsies performed over 5 years. *Radiol Med* 2011;116:477-88. English, Italian. doi: 10.1007/s11547-011-0625-x.
10. Jackman RJ, Burbank F, Parker SH, Evans WP 3rd, Lechner MC, Richardson TR, et al. Stereotactic breast biopsy of nonpalpable lesions: determinants of ductal carcinoma in situ underestimation rates. *Radiology* 2001;218:497-502. doi: 10.1148/radiology.218.2.r01fe35497.
11. Pandelidis S, Heilman D, Jones D, Stough K, Trapeni J, Suliman Y. Accuracy of 11-gauge vacuum-assisted core biopsy of mammographic breast lesions. *Ann Surg Oncol* 2003;10:43-7. doi: 10.1245/aso.2003.05.004.
12. Kettritz U, Rotter K, Schreer I, Murauer M, Schulz-Wendtland R, Peter D, et al. Stereotactic vacuum-assisted breast biopsy in 2874 patients: a multicenter study. *Cancer* 2004;100:245-51. doi: 10.1002/cncr.11887.
13. Lee CH, Carter D, Philpotts LE, Couce ME, Horvath LJ, Lange RC, et al. Ductal carcinoma in situ diagnosed with stereotactic core needle biopsy: can invasion be predicted?. *Radiology* 2000;217:466-70. doi: 10.1148/radiology.217.2.r00nv08466.
14. Kim M, Kim HJ, Chung YR, Kang E, Kim EK, Kim SH, et al. Microinvasive carcinoma versus ductal carcinoma in situ: a comparison of clinicopathological features and clinical outcomes. *J Breast Cancer* 2018;21:197-205. doi: 10.4048/jbc.2018.21.2.197.

15. Houssami N, Ciatto S, Ellis I, Ambrogetti D. Underestimation of malignancy of breast core-needle biopsy: concepts and precise overall and category-specific estimates. *Cancer* 2007;109:487-95. doi: 10.1002/cncr.22435.
16. Jiang L, Ma T, Moran MS, Kong X, Li X, Haffty BG, et al. Mammographic features are associated with clinicopathological characteristics in invasive breast cancer. *Anticancer Res* 2011;31:2327-34.
17. Wadhwa A, Majidi SS, Cherian S, Dykstra DS, Deitch SG, Hansen C, et al. Architectural Distortion on Screening Digital Breast Tomosynthesis: Pathologic Outcomes and Indicators of Malignancy. *J Breast Imaging* 2021;3:34-43.

Original Article

Factors related to bone mineral density in female patients receiving TSH-suppressive doses of levothyroxine for thyroid cancer

Araya Boonyaleepan M.D.

Tarit Taerakul M.D.

From Department of Radiology, Rajavithi Hospital, Bangkok, Thailand.

Address correspondence to A.B.(arayaboonyaleepan@yahoo.com)

Received 17 October 2022; revised 17 July 2023; accepted 17 July 2023
doi:10.46475/aseanjr.v24i2.191

Abstract

Background: Patients with thyroid cancer receive a high-dose thyroid hormone therapy after total thyroidectomy for suppression of thyroid stimulating hormone (TSH); this may affect bone mineral density (BMD). Identifying the common factors that affect BMD (including the duration of a high dose of thyroid hormone treatment) may, therefore, aid the delivery of appropriate and comprehensive care in such cases.

Objective: To identify the factors related to BMD in female patients with thyroid cancer.

Materials and Methods: This cross-sectional study evaluated data pertaining to the BMD and demographic characteristics of female patients with thyroid cancer. The patients were aged at least 40 years and received a high-dose thyroid hormone replacement therapy after total thyroidectomy at the Rajavithi Hospital between January 2004 and December 2019. The relationships between BMD and associated factors were analyzed using Pearson's correlation and multiple linear regression. A p-value of less than 0.05 was considered statistically significant.

Results: A total of 100 female patients with a mean age of 55.37 ± 11.36 (40-82) years and mean body mass index (BMI) of 24.8 ± 4.96 (15-40) were included; 60 and 56 of them were postmenopausal and coffee drinkers, respectively. High-dose thyroid hormone replacement therapy was received for a mean duration of 94.59 ± 50.36 (3-210) months and 13 patients had a history of fractures; 60%, 30%, and 10% had normal BMD, osteopenia, and osteoporosis, respectively. The factors affecting BMD included the BMI (p-value <0.001) and postmenopausal status (p-value <0.001). Subgroup analyses showed the BMI to be the factor affecting BMD in the premenopausal group (p-value <0.001). Age, BMI, and calcium supplement intake were found to have an effect on the BMD in the postmenopausal group (p-value= 0.003, 0.002, and 0.020, respectively). The duration of high-dose thyroid hormone intake had no effect on the BMD in both the overall population (p-value= 0.558) and the subgroups based on the menopausal status (p-value = 0.437 and 0.380 in premenopausal and postmenopausal groups, respectively).

Conclusion: In female patients who were treated for thyroid cancer, the factors affecting the BMD included the BMI in the premenopausal group and the age, BMI, and calcium supplementation in the postmenopausal group.

Keywords: Bone mineral density, BMD, High-dose thyroid hormone, Thyroid cancer, TSH-suppressive dose of thyroxine.

Introduction

Osteoporosis is a disease characterized by a reduction in bone mineral density (BMD) [1]. It is more common in postmenopausal women, and its incidence and severity increase with age. In Thailand, more than 50% of women aged over 70 years are affected by this disease [2]; it increases the likelihood of fractures, which are a major source of medical expenses in the elderly, and result in both increased morbidity and mortality [3-10]. Notably, the hospital mortality rate in Thailand is 2.1% [11], and the average cost of treatment for osteoporotic hip fractures was 116,458.60 Baht in 2004 [12].

Thyroid hormones affect bone resorption rather than formation, leading to a decrease in BMD and potentially leading to osteoporosis [13]. Patients with thyroid cancer are treated by surgical removal of the entire thyroid gland, after which they receive a radioactive iodine therapy to destroy the residual thyroid gland and remaining cancer. This is typically followed by high doses (thyroid stimulating hormone [TSH]-suppressive dose) of thyroid hormone therapy for more than 1 year. Investigating the impact of the duration of the high-dose thyroid hormone therapy on the BMD, and identifying the common factors affecting BMD in these patients, may, therefore, be useful in delivering appropriate and comprehensive care in such cases. The factors considered in this study included basic demographic characteristics, details pertaining to thyroid hormone treatment, and data collected for calculation of the FRAX score [14,15]; these included the age, BMI, income, the educational level, the menopausal status, coffee consumption, alcohol consumption, smoking habits, exercise habits, calcium intake, vitamin D intake, the duration of a high-dose thyroid hormone therapy, the duration of normal-dose thyroid hormone replacement before BMD measurement, the history of fractures in adulthood, the history of hip fractures in parents, the receipt of steroid medication, the history of rheumatoid arthritis, and the presence of secondary osteoporosis.

The objective of this study was to determine factors related to the BMD in patients with thyroid cancer who were receiving a high-dose thyroid hormone therapy after total thyroidectomy.

Operational definitions

The BMD is the quantity of mineral in the bone; it affects the bone strength, and is expressed in terms of the mineral mass per square centimeter of bone (gm/cm^2). The T-score is a numerical value obtained by comparing the patient's BMD (BMD_p) with that of a healthy young adult having a peak bone mass (BMD_y), and is calculated as follows: $\text{T-score} = (\text{BMD}_p - \text{BMD}_y) / \text{SD}_y$, with SD_y denoting the standard deviation in BMD of a healthy young adult. The Z-score is a numerical value obtained by comparing the patient's BMD (BMD_p) with that of age-matched

individuals (BMD_{am}), and is calculated based on the following formula: $Z\text{-score} = (BMD_p - BMD_{am})/SD_{am}$, with SD_{am} indicating the standard deviation of BMD in age-matched individuals.

A normal BMD is diagnosed when the T-score is ≤ -1 . An abnormal BMD encompasses 2 entities, namely, osteopenia and osteoporosis. Osteopenia is diagnosed when the T-score is between -1 and -2.5 and osteoporosis is diagnosed when the T-score is ≥ -2.5 . For the spine, the L1–L4 region is used unless focal artifacts (such as spurs) require exclusion of individual vertebra to avoid falsely high BMD.

The BMI is a measure of obesity in adults aged 20 years and over and is calculated using the following formula: $BMI = \text{body weight (kg)} / (\text{height [m]})^2$. The premenopausal group included all women who menstruated until menopause. The postmenopausal group included all women who had been menopausal for more than a year.

Coffee consumption, alcohol consumption, smoking habits, exercise habits, calcium intake, vitamin D intake, and the receipt of steroid medication were evaluated based on the current status. In cases where any factor was present, further details were obtained regarding the amount or frequency. In this context, a unit of alcohol varies slightly between different countries, and contains 8-10 g of alcohol. This is equivalent to a standard glass of beer (285 ml), a single measure of spirits (30 ml), a medium-sized glass of wine (120 ml), or a single measure of an aperitif (60 ml).

High-dose thyroid hormone (TSH-suppressive dose of levothyroxine) therapy is administered to patients at higher than normal levels to suppress TSH levels to below $0.3 \mu\text{IU/ml}$ [1].

Patients were considered to have a history of previous fractures in adulthood if they had a history of fracture from any cause. A history of hip fractures in the parents was considered to be positive in cases where the patient's mother or father had a history of hip fracture. Rheumatoid arthritis was considered to be present in

cases with a confirmed diagnosis of rheumatoid arthritis. Secondary osteoporosis was considered to be present in cases where the patient had a disorder strongly associated with osteoporosis. These included: type I (insulin dependent) diabetes, osteogenesis imperfecta in adults, untreated long-standing hyperthyroidism, hypogonadism or premature menopause (<45 years), chronic malnutrition, malabsorption, and chronic liver disease.

Materials and methods

This was a cross-sectional study. Bone density measurements and other data were obtained from female patients who were aged at least 40 years and were receiving a high-dose thyroid hormone therapy after total thyroidectomy for thyroid cancer at the Rajavithi Hospital between January 2004 and December 2019.

The data collected included independent variables, namely, age, BMI, income, the educational level, the menopausal status, coffee consumption, alcohol consumption, smoking habits, exercise habits, calcium intake, vitamin D intake, the duration of high-dose thyroid hormone treatment (to maintain TSH < 0.3 μ IU/mL), the duration of normal-dose thyroid hormone replacement before BMD measurement, the history of fractures in adulthood, the history of hip fractures in parents, the receipt of steroid medication, the history of rheumatoid arthritis, and the presence of secondary osteoporosis. The dependent variables comprised of the BMD; T-score; and Z-scores of the lumbar spine (L1-L4 vertebrae), total hip, and femoral neck. The BMD was measured by dual-energy X-ray absorptiometry (DXA) using the Prodigy system, GE Healthcare, USA.

Statistical analysis

The sample size for this study was calculated using the mean difference (mean change) from high-dose thyroid hormone treatment estimation formula (Wayne WD, 1995) [16]:

$$n = \frac{(Z_{\alpha/2})^2 \times (SD)^2}{d^2}$$

n = sample size

*Z*_{α/2} = statistical value under the standard curve when
the level of statistical significance (α = 0.05) is 1.96

SD = standard deviation

d = precision estimate from 20% change in mean BMD from
high-dose thyroid hormone treatment.

In the study by Kim et al. [17], the post-treatment BMD of the lumbar spine had a mean (±standard deviation) value of 1.161±1.278; where *d* = 20% of mean (*d* = 1.161×0.20=0.232)

$$n = \frac{(1.96)^2 \times (1.278)^2}{(0.232)^2}$$

$$n = 97$$

The sample group (*n*=100) was selected by systematic sampling based on the hospital number.

Descriptive statistics

Categorical data have been reported as numbers and percentages. Normally distributed continuous data have been reported as the mean with standard deviation, while non-normally distributed continuous data have been presented as the median (with minimum and maximum).

Inferential statistics

Kolomogorov- Smirnov test was used for testing the normality of the data distribution. It was found that p-value = 0.200, interpreted that the data were normal distribution. The lowest T-score was used to represent the individual BMD value for analysis. The relationships between the BMD and associated factors were analyzed using Pearson's correlation and multiple linear regression. A p-value of less than 0.05 was considered statistically significant.

Ethical considerations

This study was approved by the Human Research Ethics Committee, Rajavithi Hospital.

The certificate of approval number was 64115.

Results

A total of 100 female patients who had undergone total thyroidectomy for thyroid cancer and subsequently received a high-dose thyroid hormone therapy were included. The mean age was 55.37 ± 11.36 (40-82) years, mean BMI was 24.8 ± 4.96 (15-40), and median income was 10,000 (600 - 300,000) Baht per month; 70, 27, and 3 participants received education up to the undergraduate level, the bachelor's degree, and the postgraduate level, respectively. A total of 40 and 60 participants were premenopausal and postmenopausal, respectively, and 56 were coffee drinkers who had an average intake of 5.2 ± 2.87 (0.5-14) cups per week. Ten of the subjects consumed alcohol, but none consumed more than 3 units per day. None of the patients smoked, and 63 were physically active; 20 exercised more than 3 days a week. Among the 56 patients taking calcium supplements, the average intake was $2,389 \pm 1,978$ (250 to 9,000) mg/day. A total of 30, 17 and 13 patients received vitamin D, D2, and D3 supplementation, respectively. The mean duration

of the high-dose thyroid hormone treatment was 94.59 ± 50.36 (3 - 210) months and the average period of normal-dose thyroid hormone replacement before BMD measurement was 29.74 ± 39.97 (0 - 216) months. Thirteen patients had a history of fractures and 4 reported a history of fractures in their parents; 1 patient each had rheumatoid arthritis and secondary osteoporosis, and none received steroids (Table 1).

Table 1. Demographic data and clinical characteristics of the study population.

Characteristics	Patients (n = 100)
Age (years), mean \pmSD	55.37 \pm 11.36
BMI (kg/m²) mean \pmSD	24.81 \pm 4.96
<18.0, n (%)	3 (3.0)
18.0-23.0, n (%)	43 (43.0)
>23.0, n (%)	54 (54.0)
Monthly income median (min-max)	10,000.0 (600-300,000.0)
Less than 10,000 Baht, n (%)	53 (53.0)
10,001 to 15,000 Baht, n (%)	18 (18.0)
15,001 to 20,000 Baht, n (%)	10 (10.0)
Over 20,001 Baht, n (%)	19 (19.0)
Education	
Lower than bachelor degree, n (%)	70 (70.0)
Bachelor degree, n (%)	27 (27.0)
Higher than bachelor degree, n (%)	3 (3.0)
Postmenopausal	
No, n (%)	40 (40.0)
Yes, n (%)	60 (60.0)

Characteristics	Patients (n = 100)
Coffee drinkers	
No, n (%)	44 (44.0)
Yes, n (%)	56 (56.0)
Amount (cups/week), mean \pm SD (min-max)	5.21 \pm 2.87 (0.5-14.0)
Alcohol drinkers	
No, n (%)	90 (90.0)
Yes, n (%)	10 (10.0)
Smokers	
No, n (%)	100 (100.0)
Yes, n (%)	0 (0.0)
Exercise	
No, n (%)	37 (37.0)
Yes, n (%)	63 (63.0)
Exercise more than 3 days (n=63)	
No, n (%)	43 (68.3)
Yes, n (%)	20 (31.7)
Calcium supplements	
No, n (%)	44 (44.0)
Yes, n (%)	56 (56.0)
Amount of intake (mg/day) mean \pm SD. (min-max)	2,389.8 \pm 1978.1 (250-9,000)
Vitamin D supplements	
No, n (%)	70 (70.0)
Yes, n (%)	30 (30.0)
- Vitamin D2, n (%)	17 (56.7)
- Vitamin D3, n (%)	13 (43.3)

Characteristics	Patients (n = 100)
Duration of high-dose thyroxine (months) mean \pmSD (min-max)	94.59 \pm 50.36 (3-210)
Duration of normal-dose thyroxine (months) mean \pmSD (min-max)	29.74 \pm 39.97 (0-216)
History of fracture	
No, n (%)	87 (87.0)
Yes, n (%)	13 (13.0)
History of fracture in parents	
No, n (%)	96 (96.0)
Yes, n (%)	4 (4.0)
Receipt of steroids	
No, n (%)	100 (100.0)
Yes, n (%)	0 (0.0)
Rheumatoid arthritis	
No, n (%)	99 (99.0)
Yes, n (%)	1 (1.0)
Secondary osteoporosis	
No, n (%)	99 (99.0)
Yes, n (%)	1 (1.0)

*Data are presented as the number (%) or mean \pm SD. or median (min-max)
 BMI = body mass index, SD = standard deviation*

The results of analysis of the BMD, T-scores, and Z-scores at the lumbar spine, total hip, and femoral neck are shown in Table 2. A total of 60 patients were diagnosed with normal BMD. The remaining 40 patients had abnormal BMD, with 30 and 10 demonstrating the presence of osteopenia and osteoporosis, respectively (Figure 1).

Table 2. Bone mineral density of female patients with thyroid cancer after administration of TSH-suppressive doses of levothyroxine (n = 100).

Bone mineral density	Mean	Standard Deviation	Minimum	Maximum
Lumbar BMD(gm/cm ²)	1.073	0.19	0.657	1.514
Lumbar T-score	-0.3	1.57	-3.8	3.4
Lumbar Z-score	0.8	1.34	-2.1	4.1
Total hip BMD(gm/cm ²)	0.935	0.16	0.479	1.298
Total hip T-score	-0.2	1.24	-3.8	2.7
Total hip Z-score	0.7	1.10	-2.1	3.0
Femoral neck BMD (gm/cm ²)	0.864	0.15	0.444	1.157
Femoral T-score	-0.4	1.20	-3.9	2.0
Femoral Z-score	0.7	1.01	-1.9	2.8

BMD = Bone mineral density

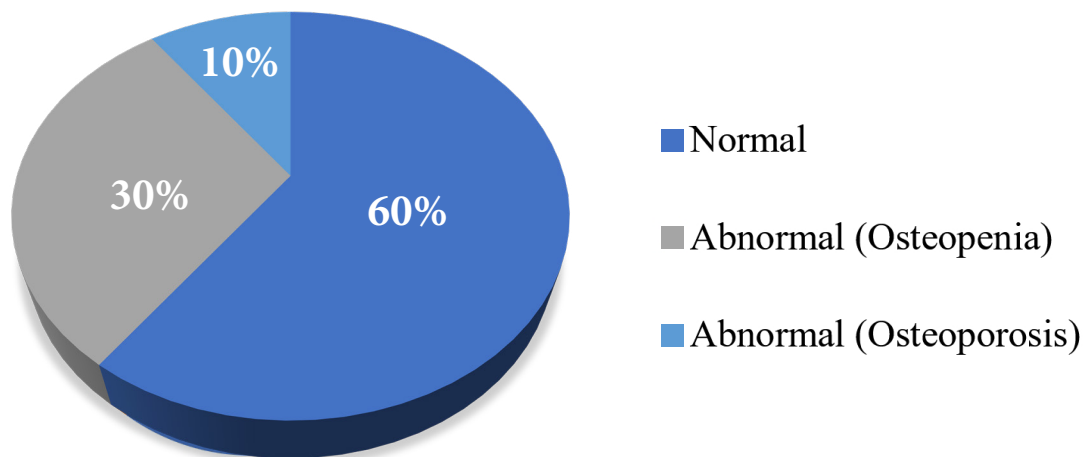


Figure 1. Diagnosis on BMD measurement.

Table 3 shows the results of Pearson’s correlation analysis between the BMD and various factors. The BMI ($r=0.571$, p -value <0.001) and coffee consumption ($r=0.210$, p -value $=0.036$) were found to be the factors with statistically significant positive correlation with the BMD. The factors showing statistically significant negative correlation with the BMD included age ($r=-0.535$, p -value <0.001), the duration of a high-dose hormone therapy (months) ($r=-0.510$, p -value <0.001) and the postmenopausal status ($r=-0.510$, p -value <0.001).

Table 3. Correlation between BMD and various factors.

Factors	Bone mineral density	
	Correlation (r)	p-value
Duration of high-dose thyroid hormone therapy (months)	-0.510	$<0.001^*$
Age (years)	-0.535	$<0.001^*$
BMI (kg/m^2)	0.571	$<0.001^*$
Monthly income (Baht)	0.031	0.764
Education	0.010	0.919
Coffee consumption	0.210	0.036*
Vitamin D supplementation	0.094	0.352
Alcohol consumption	0.080	0.430
Calcium supplementation	0.083	0.412
Exercise	0.024	0.809
Postmenopausal status	-0.510	$<0.001^*$
Fracture history	-0.141	0.163

*Significant at $p < 0.05$

As shown in Table 4, multiple linear regression of the various factors that correlated with the BMD showed the BMI to have a statistically significant positive correlation (p-value <0.001); conversely, postmenopausal status demonstrated a statistically significant negative correlation with the BMD (p-value <0.001). The duration of high-dose hormone therapy and coffee consumption showed no correlation with the BMD (p>0.05).

Table 4. Factors associated with BMD on multiple linear regression.

Factors	B	Standard error	Standard beta	p-value
BMI	0.107	0.021	0.422	<0.001*
Duration high-dose thyroid hormone therapy	-0.001	0.002	-0.046	0.558
Coffee consumption	0.321	0.193	0.127	0.100
Postmenopausal status	-0.917	0.207	-0.359	<0.001*
(Constant)	-2.943	0.609		

$R = 0.678$, $R^2 = 0.460$, $p\text{-value} < 0.001$, $B = \text{regression coefficient}$

Table 5 shows the results of Pearson's correlation analysis between the premenopausal and postmenopausal subgroups. In the premenopausal group, the BMI was found to be the factor demonstrating a statistically significant positive correlation with the BMD (r=0.651, p-value <0.001). In the postmenopausal group, age demonstrated a statistically significant negative correlation with the BMD (r=-0.426, p-value <0.001); however, the BMI (r=0.411, p-value <0.001), coffee consumption (r=0.315, p-value <0.014), and calcium supplementation (r=0.289, p-value <0.025) showed a statistically significant positive correlation with the BMD.

Table 5. Correlation between the BMD and various factors in the premenopausal and postmenopausal subgroups.

Factors	Bone mineral density			
	Premenopausal subgroup		Postmenopausal subgroup	
	Correlation (r)	p-value	Correlation (r)	p-value
Duration of high-dose thyroid hormone therapy (months)	-0.126	0.437	-0.115	0.380
Age (years)	0.202	0.211	-0.426	0.001*
BMI (kg/m ²)	0.651	<0.001*	0.411	0.001*
Monthly income (Baht)	-0.138	0.397	0.008	0.955
Education	-0.215	0.183	0.003	0.982
Coffee consumption	0.074	0.648	0.315	0.014*
Vitamin D supplementation	0.116	0.474	0.147	0.263
Alcohol consumption	-0.130	0.423	0.062	0.636
Calcium supplementation	0.064	0.695	0.289	0.025*
Exercise	-0.294	0.066	0.001	0.999
Fracture history	0.152	0.350	-0.244	0.060

*Significant at $p < 0.05$

Table 6 shows the results of multiple linear regression analysis in the postmenopausal subgroup. Age, BMI, and calcium supplementation demonstrated a statistically significant correlation with the BMD (p-value <0.001).

Table 6. Factors associated with BMD in the postmenopausal group (on multiple linear regression).

Factors	B	Standard error	Standard beta	p-value
Age	-0.040	0.013	-0.327	0.003*
BMI	0.097	0.030	0.336	0.002*
Coffee consumption	0.485	0.248	0.208	0.055
Calcium supplementation	0.599	0.249	0.249	0.020*
(Constant)	-1.753	1.157		

$R = 0.644$, $R^2 = 0.415$, $p\text{-value} < 0.001$, $B = \text{regression coefficient}$

Discussion

In the present study, the 100 female patients with thyroid cancer had a mean age of 55.37 ± 11.36 (40–82) years and a mean BMI of 24.81 ± 4.96 . The mean duration of the high-dose thyroid hormone treatment extended for 94.59 ± 50.36 (3-210) months, and 60% of the patients were postmenopausal. The mean values of the measured lumbar spine, total hip, and femoral neck BMD were 1.073, 0.935 and 0.864 g/cm², respectively; the respective mean T-scores were -0.3, -0.2 and -0.4, respectively, and the corresponding mean Z-scores were 0.8, 0.7 and 0.7, respectively. The majority (60%) of patients were found to have a normal BMD; 30% and 10% had osteopenia and osteoporosis, respectively.

In their study, Limpaphayom et al. [18] evaluated the BMD in 1773 Thai women aged 11 to 80 years and found the highest BMD in the age range of 30-34 years. The mean BMD of the spine and femoral neck were found to be 0.957 and 0.814 g/cm², respectively. The BMD declined significantly after the age of 35 years, and there was rapid deterioration by the age of 50 years. In their study, Gomes et al. [19] compared 109 postmenopausal women who received high-dose thyroid hormone therapy for thyroid cancer with women of the same age who had a

normal thyroid status. The mean age of the patients was 58.4 ± 8.3 years; the mean TSH level was 0.21 ± 0.28 $\mu\text{IU/ml}$ and the lumbar spine and total femur T-scores were -1.09 ± 1.43 and -0.12 ± 1.18 , respectively. No differences were found between the lumbar spine and total femur T-scores of the subjects and controls.

This study found that the BMI had a direct effect on the BMD; this is in agreement with the findings reported by Fawzy et al. [20]. They evaluated the relationship between the BMI and BMD in a sample of 101 individuals, 39 and 62 of whom had normal and low BMD, respectively. A low BMD was observed in 82.4% of the normal BMI group; in the overweight and obese groups, the corresponding proportions were 78.1% and 44.2%, respectively. Notably, the latter figure was statistically significant ($p < 0.001$). Hariri et al. [21] studied 198 patients with type 2 diabetes mellitus who were aged 50 to 90 years and found a positive relationship between the BMI and BMD T-scores in the hip and spine regions. They concluded that a low BMI ($< 18.5 \text{ kg/m}^2$) may be a risk factor for osteoporosis in adults with diabetes, whereas a normal/high BMI could protect them against this disease. In their cross-sectional study, Ma et al. [22] analyzed data from the datasets of the National Health and Nutrition Examination Survey 2005–2006, 2007–2008, 2009–2010, 2013–2014, and 2017–2018. A total of 10,910 participants (5,654 males and 5,256 females) aged over 50 years were enrolled. In addition to finding a simple linear positive association between the BMI and BMD, they observed the existence of a saturation value, which persisted during site-, sex-, age-, and race-specific subgroup analyses. They, therefore, concluded that maintaining the BMI at a reasonable value (approximately 26 kg/m^2) may provide the most significant benefit in older adults in terms of maintenance of an optimal BMD and reduction of other obesity-related diseases.

In postmenopausal women, estrogen deficiency increases the rate of both bone resorption and formation; the rate of resorption is much higher, resulting in a rapid decline in the BMD. The present study confirmed that a postmenopausal status correlates with a decrease in the BMD. In this context, Finkelstein et al. [23] conducted a longitudinal cohort study in 1902 African-American, Caucasian, Chinese, and Japanese women who were premenopausal or early perimenopausal

at baseline. The BMD of the lumbar spine and total hip was evaluated across a maximum of six annual visits. Changes in the BMD during the premenopausal or early perimenopausal period were minimal. However, the values declined substantially in the late perimenopausal period, with an average loss of 0.018 and 0.010 g/cm²·yr from the spine and hip, respectively ($P < 0.001$ for both). In the postmenopausal subgroup, the rates of loss from the spine and hip were 0.022 and 0.013 g/cm²·yr, respectively ($P < 0.001$ for both).

On subgroup analysis in our study, the factors associated with BMD in the postmenopausal group were the BMI, age, and calcium supplementation. Our results were consistent with those reported by Chen et al. [24]. Their retrospective study included 69 Taiwanese women (44 premenopausal and 25 postmenopausal) with differentiated thyroid cancer who had undergone a regular thyroid hormone suppressive therapy for more than 3 years (mean: 7.3 +/- 3.0 years; range: 3 to 15 years). They found a strong correlation between the BMD and age, BMI, and serum calcium levels. However, no correlation was found with the degree of TSH suppression or the duration of TSH suppression therapy. In their prospective study, Kung et al. [25] evaluated 46 postmenopausal women with thyroid carcinoma for 2 years; they evaluated the rate of bone loss and assessed whether calcium supplementation with or without intranasal calcitonin could decrease the rate of bone loss. All patients were receiving a stable dose of thyroxine (170 +/- 60 micrograms/day or 3.0 +/- 1.4 micrograms/kg/day) for more than one year and all had TSH levels of 0.03 µIU/L or less; the BMD was measured at 6-month intervals. The subjects were randomized into three groups: 1) intranasal calcitonin (200 IU daily) for 5 days/week with 1000 mg calcium daily, 2) calcium alone, or 3) placebo. The results showed that at the end of the second year, both groups 1 and 2 had stable bone mass; however, group 3 showed a significant loss in bone mass (lumbar spine: 5.0%, hip: 6.7%, trochanter: 4.7%, and Ward's triangle: 8.8%; $P < 0.05$).

The negative impact of TSH-suppressive doses of thyroxine on BMD has been debated. In 2017, Chang et al. [26] performed a retrospective study using data from the Korea National Health and Nutrition Examination Survey between 2008 and 2011. Among the 18618 patients included, 80 (11 male and 69 female) had

thyroid cancer; no significant difference was found between the groups with and without thyroid cancer in terms of the incidence of osteopenia and osteoporosis ($p = 0.783$). Subgroup analyses of women and postmenopausal women also showed similar results ($p = 0.685$ and $p = 0.095$, respectively).

In their study, Zhang et al. [1] investigated the effects of thyrotropin suppression on lumbar spine density in 225 postmenopausal women with differentiated thyroid carcinoma. The patients were divided into 2 groups; 154 received TSH-suppressive doses of thyroxine (median TSH $<0.3 \mu\text{IU/ml}$) and 71 (control group) did not receive TSH-suppressive doses (median TSH $>0.3 \mu\text{IU/ml}$). There was no significant difference between either group in terms of the lumbar spine BMD at baseline and at 6, 12, and 24 months before and after treatment ($t=1.37$, $p=0.17$; $t=-0.128$, $p=0.89$; and $t=-0.547$, $p=0.89$ at 6, 12, and 24 months, respectively). Comparison of the BMD before and 2 years after TSH-suppressive therapy demonstrated a 1.9% reduction; at 24 months, a significant difference was found between the TSH-suppressed and control groups in terms of the number of patients with osteopenia and osteoporosis (103/152 vs. 32/68, $\chi^2=2.88$, $p=0.004$). However, no significant difference was found at either 6 months (72/154 vs. 35/70, $\chi^2=0.45$, $p=0.65$) or 12 months (71/154 vs. 30/69, $\chi^2=0.36$, $p=0.72$).

In 1996, Ongphiphadhanakul et al. [27] studied the effect of TSH-suppressive doses of levothyroxine on BMD in Thai women. The study included 27 (18 premenopausal and 9 postmenopausal) women, who received at least 150 micrograms of thyroxine per day for over two years for the treatment of nodular thyroid disease. Comparison of their Z-scores with those of 54 age-matched healthy controls showed that postmenopausal women who received thyroxine for a prolonged period demonstrated a statistically significant reduction in anteroposterior spinal (-0.69 ± 0.20 vs 0.05 ± 0.17 , $p < 0.01$), femoral neck (-0.61 ± 0.35 vs 0.18 ± 0.24 , $p < 0.05$), and femoral trochanter (-0.64 ± 0.37 vs 0.13 ± 0.22 , $p < 0.05$) BMD; no significant difference was found in premenopausal women. In 2006, Mazokopakis et al. [28] performed a comparative study on the femoral BMD in premenopausal women with thyroid cancer who received TSH-suppressive doses of thyroxine. On measuring the BMD before and at 12 and

48 months after receiving thyroxine, they concluded that administration of the TSH-suppressive therapy for at least one year may lower the BMD in the femoral neck, femoral trochanter, and Ward's triangle in premenopausal women.

In their systemic review, Yoon et al. [29] identified and analyzed data from 11 published controlled cross-sectional studies (including approximately 571 patients with well differentiated thyroid cancer and 836 controls). TSH suppression was associated with a lower total hip (weighted mean difference: -0.023; 95% confidence interval: -0.047 to 0.000; $p=0.050$) and spine (weighted mean difference: -0.041; 95% confidence interval: -0.057 to -0.026; $p<0.001$) BMD in postmenopausal women with differentiated thyroid cancer; however, no such association was found in male and premenopausal female patients. In our study, no correlation was observed between the duration of TSH-suppressive doses of thyroxine and BMD. Subgroup analyses in the premenopausal and postmenopausal groups showed the same results. Other factors that did not have any effect on the BMD included income, the educational level, coffee consumption, alcohol consumption, smoking habits, exercise habits, vitamin D intake, the duration of normal-dose thyroid hormone replacement before BMD measurement, the history of fractures in adulthood, the history of hip fractures in parents, the receipt of steroid medication, history of rheumatoid arthritis, and presence of secondary osteoporosis.

This study has certain limitations, which may partly be attributed to the retrospective design. First, patients who had osteoporosis before treatment for thyroid cancer could not be excluded, as almost all patients had never undergone testing for BMD. A proportion of the patients consumed calcium and vitamin D owing to postoperative hypoparathyroidism. Second, TSH testing was performed every 3-6 months during the follow-up visits; there may have, therefore, been some discrepancy in the recorded duration of TSH-suppressive therapy. Third, although we had initially planned to only include insufficiency fractures in adulthood, difficulties in identification of such cases prompted the inclusion of all fractures irrespective of the cause.

Although this study had only 100 samples, the analysis results from the G*Power software showed that there was a high level of power (0.996).

The findings from this study showed that the duration of TSH-suppressive levothyroxine administration had no effect on the BMD. This provides a valuable reference for decision-making during the treatment. The BMI demonstrated a positive correlation with the BMD; patients should, therefore, be advised not to maintain a BMI that is considerably low. As calcium supplementation had a positive effect on the BMD in postmenopausal patients, calcium supplementation may be useful for preventing osteoporosis in postmenopausal patients with low BMI.

Conclusion

In female patients with thyroid cancer, the BMI and postmenopausal status were found to be related to the BMD. In the premenopausal group, the BMD was affected by the BMI. However, the age, BMI, and calcium supplementation were found to affect the BMD in the postmenopausal group. The majority of the subjects had normal BMD.

The period of receiving high doses of levothyroxine had no effect on BMD, so in the cases of patients with high thyroglobulin (Tg) who require high doses of levothyroxine over a long period of time, patients and their physicians may not have to worry as much about the negative effects on BMD. In postmenopausal patients with low BMI, calcium supplementation should be considered to prevent osteoporosis.

References

1. Zhang P, Xi H, Yan R. Effects of thyrotropin suppression on lumbar bone mineral density in postmenopausal women with differentiated thyroid carcinoma. *Onco Targets Ther* 2018;11: 6687-92. doi: 10.2147/OTT.S171282.
2. Thangwijitra S, Sakondhavat C, Soontrapa S, Kaewrudee S, Somboonporn W. Prevalence of osteoporosis in postmenopausal women at Srinagarind Hospital, Khon Kaen University. *Thai J Obstet Gynaecol* 2010;18:26-34.
3. Johnell O. The socioeconomic burden of fractures: today and in the 21st century. *Am J Med* 1997;103:20S-5S. doi: 10.1016/s0002-9343(97)90023-1.
4. Kanis JA, Oden A, Johnell O, Jonsson B, de Laet C, Dawson A. The burden of osteoporotic fractures: a method for setting intervention thresholds. *Osteoporos Int* 2001;12:417-27. doi: 10.1007/s001980170112.
5. Johnell O, Kanis JA. An estimate of the worldwide prevalence, mortality and disability associated with hip fracture. *Osteoporos Int* 2004;15:897-902. doi: 10.1007/s00198-004-1627-0.
6. Pasco JA, Sanders KM, Hoekstra FM, Henry MJ, Nicholson GC, Kotowicz MA. The human cost of fracture. *Osteoporos Int* 2005;16:2046-52. doi: 10.1007/s00198-005-1997-y.
7. Johnell O, Kanis JA. An estimate of the worldwide prevalence and disability associated with osteoporotic fractures. *Osteoporos Int* 2006;17:1726-33. doi: 10.1007/s00198-006-0172-4.
8. Suriyawongpaisal P, Siriwongpairat P, Loahachareonsombat W, Angsachon T, Kumpoo U, Sujaritputtangkul S, et al. A multicenter study on hip fractures in Thailand. *J Med Assoc Thai* 1994;77:488-95.

9. Suriyawongpaisal P, Chariyalertsak S, Wanvarie S. Quality of life and functional status of patients with hip fractures in Thailand. *Southeast Asian J Trop Med Public Health* 2003;34:427-32.
10. Chariyalertsak S, Suriyawongpisal P, Thakkinstain A. Mortality after hip fractures in Thailand. *Int Orthop* 2001;25:294-7. doi: 10.1007/s002640100270.
11. Woratanarat P, Wajanavisit W, Lertbusayanukul C, Loahacharoensombat W, Ongphiphatanakul B. Cost analysis of osteoporotic hip fractures. *J Med Assoc Thai* 2005;88 Suppl 5:S96-104.
12. Pongchaiyakul C, Songpattanasilp T, Taechakraichana N. Burden of osteoporosis in Thailand. *J Med Assoc Thai* 2008;91:261-7.
13. Bassett JH, Williams GR. Role of Thyroid Hormones in Skeletal Development and Bone Maintenance. *Endocr Rev* 2016;37:135–87. doi: 10.1210/er.2015-1106.
14. Hillier TA, Cauley JA, Rizzo JH, Pedula KL, Ensrud EK, Bauer DC, et al. WHO Absolute Fracture Risk Models (FRAX): Do Clinical Risk Factors Improve Fracture Prediction in Older Women Without Osteoporosis? *J Bone Miner Res* 2011;26:1774-82. doi: 10.1002/jbmr.372.
15. Kanis JA, Johansson H, Harvey NC, McCloskey EV. A brief history of FRAX. *Arch Osteoporos* 2018;13:118. doi: 10.1007/s11657-018-0510-0.
16. Daniel WW.. *Biostatistics: A foundation of analysis in the health sciences*. 6th ed. New York: John Wiley and Sons; 1995.
17. Kim CW, Hong S, Oh SH, Lee JJ, Han JY, Hong S, et al. Change of bone mineral density and biochemical markers of bone turnover in patients on suppressive levothyroxine therapy for differentiated thyroid carcinoma. *J Bone Metab* 2015; 22:135-41. doi: 10.11005/jbm.2015.22.3.135.

18. Limpaphayom KK, Taechakraichana N, Jaisamrarn U, Bunyavejchevin S, Chaikittisilpa S, Poshyachinda M, et al. Bone mineral density of lumbar spine and proximal femur in normal Thai women. *J Med Assoc Thai* 2000;83:725-31.
19. de Melo TG, da Assumpção LV, Santos Ade O, Zantut-Wittmann DE.. Low BMI and low TSH value as risk factors related to lower bone mineral density in postmenopausal women under levothyroxine therapy for differentiated thyroid carcinoma. *Thyroid Res* 2015;8:7. doi: 10.1186/s13044-015-0019-1.
20. Fawzy T, Muttappallymyalil J, Sreedharan J, Ahmed A, Alshamsi SO, Al Ali MS, et al. Association between body mass index and bone mineral density in patients referred for dual-energy x-ray absorptiometry scan in Ajman, UAE. *J Osteoporos* 2011; 2011:876309. doi: 10.4061/2011/876309.
21. Hariri AF, Almatrafi MN, Zamka AB, Babaker AS, Fallatah TM, Althouwaibi OH, et al. Relationship between body mass index and t-scores of bone mineral density in the hip and spine regions among older adults with diabetes: a retrospective review. *J Obes* 2019;2019:9827403. doi: 10.1155/2019/9827403.
22. Ma M, Feng Z, Liu X, Jia G, Geng B, Xia Y. The saturation effect of body mass index on bone mineral density for people over 50 years old: a cross-sectional study of the US population. *Front Nutr* 2021;8:763677. doi: 10.3389/fnut.2021.763677.
23. Finkelstein JS, Brockwell SE, Mehta V, Greendale GA, Sowers MR, Ettinger B, et al. Bone mineral density changes during the menopause transition in a multiethnic cohort of women. *J Clin Endocrinol Metab* 2008;93:861-8. doi:10.1210/jc.2007-1876.
24. Chen CH, Chen JF, Yang BY, Liu RT, Tung SC, Chien WY, et al. Bone mineral density in women receiving thyroxine suppressive therapy for differentiated thyroid carcinoma. *J Formos Med Assoc* 2004;103:442-7.

25. Kung AW, Yeung SS. Prevention of bone loss induced by thyroxine suppressive therapy in postmenopausal women: the effect of calcium and calcitonin. *J Clin Endocrinol Metab* 1996; 81:1232-6. doi: 10.1210/jcem.81.3.8772604.
26. Chang MC. Bone mineral density in thyroid cancer patients: data from the Korea National Health and Nutrition Examination Survey. *J Endocr Surg* 2017;17(4):153-9.
27. Ongphiphadhanakul B, Puavilai G, Rajatanavin R. Effect of TSH-suppressive doses of levothyroxine on bone mineral density in Thai women. *J Med Assoc Thai* 1996; 79:563-7.
28. Mazokopakis EE, Starakis IK, Papadomanolaki MG, Batistakis AG, Papadakis JA. Changes of bone mineral density in pre-menopausal women with differentiated thyroid cancer receiving L-thyroxine suppressive therapy. *Curr Med Res Opin* 2006; 22:1369-73. doi: 10.1185/030079906X115612.
29. Yoon BH, Lee Y, Oh HJ, Kim SH, Lee YK. Influence of thyroid-stimulating hormone suppression therapy on bone mineral density in patients with differentiated thyroid cancer: a meta-analysis. *J Bone Metab* 2019;26:51-60. doi: 10.11005/jbm.2019.26.1.51.

Original Article

Comparative study of setup errors between new and reused thermoplastic masks in irradiated head and neck cancer patients

Nipha Chumsuwan, Ph.D.

Lalita Romkedpikun, B.Sc.

Janyaporn Thongthae, B.Sc.

Tanapan Yousuk, B.Sc.

From Department of Radiology, Faculty of Medicine, Prince of Songkla University, Songkhla, Thailand.

Address correspondence to N.C.(noknipha@hotmail.com)

Received 25 April 2023; revised 19 August 2023; accepted 19 August 2023
doi:10.46475/aseanjr.v24i2.808

Abstract

Background: The accuracy and precision of patient setup are important in radiotherapy. The thermoplastic mask is used to immobilize head and neck cancer patient. However, the mask is reused for low-income patients. Therefore, the setup error should be evaluated to approve that these patients remain in the exact position during treatment.

Objective: To investigate setup errors with the use of thermoplastic masks in head and neck cancer patients and to compare setup errors of new and reused thermoplastic masks.

Materials and Methods: Eighty patients who underwent volumetric modulated arc radiotherapy (VMAT) for head and neck cancer lesions were retrospectively evaluated. The setup error, population systematic error, and population random error were calculated. Subsequently, setup errors in patients using the new and reused thermoplastic masks were compared.

Results: The population systematic error in the vertical, longitudinal, and lateral directions for new masks was 2.02, 2.27, and 2.13 mm, respectively, and that for reused masks was 2.37, 1.96, and 2.33 mm, respectively. The population random error in the vertical, longitudinal, and lateral direction for new masks was 1.46, 1.54, and 1.57 mm, respectively, and that for reused masks was 1.65, 1.63, and 1.87 mm, respectively. The results showed no statistically significant difference supported by p value > 0.05 in the setup error between using the new and reused thermoplastic masks in all directions.

Conclusion: For head and neck radiotherapy, the population setup errors were < 3 mm in all directions. Moreover, thermoplastic masks can be reused in patients with head and neck cancer.

Keywords: Setup error, Head and neck cancer, Image-guided radiotherapy, Thermoplastic mask.

Introduction

There are many treatment methods for cancer, including radiotherapy, surgery, chemotherapy, and hormone therapy. Treatments can be used individually or in a combination. Radiotherapy is one of the most common methods for treatment of head and neck cancer [1-3]. Modern techniques are used in radiotherapy, including image-guided radiotherapy (IGRT), which uses an imaging system in the treatment room before or during radiotherapy [4-7]. This is a tool for improving the accuracy and precision of treatment delivery. In addition, immobilization devices are used to ensure the accurate positioning and repositioning of patients during treatment delivery, which can reduce the setup margin. Therefore, immobilization devices are necessary, especially thermoplastic masks for head and neck cancer [8-9].

A head-and-shoulder mask that covers the length from the head to the shoulder is used to immobilize the patient in the supine position [10-11]. However, the high cost of cancer treatment is related to the treatment techniques and immobilization devices. A thermoplastic mask is a device that is relatively expensive. Consequently, the mask is reused once more for low-income patients. However, accuracy and precision should be considered in patients undergoing radiotherapy. Therefore, the setup error should be evaluated to approve that the patient remains in the exact position during treatment delivery. The random errors are the deviations between different fractions that can vary in direction. Random errors introduced by organ motion and patient setup. The systematic errors are the deviations between the planned patient position and the average patient position over the entire course of treatment, which occurs in the same direction. Systematic errors introduced by target volume delineation, organ motion, and patient setup. The current study is a retrospective analysis aimed to investigate the setup errors in head and neck cancer patients with thermoplastic masks and to compare the setup errors of patients with new and reused thermoplastic masks.

Materials and methods

Institutional Review Board Statement: The study protocol was approved by Ethics Committee of Faculty of Medicine (REC 63-566-7-2), date of approval; 13/01/2021.

Treatment procedure

Eighty head and neck cancer patients were retrospectively evaluated. The number of patients with new and reused thermoplastic masks was 40 and 40 cases, respectively. The reused masks were reused only once. The masks were warmed and flattened using water bath before being moulded on the patient's skin. Computed tomography (CT) images were received using the Brilliance CT Big Bore (Philips, Amsterdam, The Netherlands), and a head-and-shoulder thermoplastic mask (Type-STM, CIVCO, IA, U.S.A.) was used to immobilize the

patients with head and neck cancer. An example of the head-and-shoulder mask used in a patient is shown in Figure 1. The VMAT treatment plans were performed using the Eclipse treatment planning system (Varian Medical Systems, Palo Alto, CA, USA). Patients were treated with 6 MV photon beams using TrueBeam STx and Unique machines (Varian Medical Systems, Inc., Palo Alto, CA). For treatment delivery, patients were positioned and immobilized in the same manner as in CT planning. Imaging, including electronic portal imaging device (EPID), 2D-kV planar (AP-Lat), or cone beam CT (CBCT), were performed on the first three fractions then weekly. The images were acquired more than 5 times in each patient. The registration was first performed automatically by the system and was then manually checked by radiological technologists and confirmed by treating oncologists to ensure that the matching was accurate. The registration between the acquired images and planning images was performed according to the bony and soft tissue anatomy. The patient positioning was modified using delta couch shift. The treatment couch was capable of shifting direction vertically (up and down), longitudinally (in and out), and laterally (right and left) without a rotational direction.



Figure 1. *An example of a head-and-shoulder thermoplastic mask used to immobilize the patient.*

Setup error quantification

Simulation images and pretreatment images (EPID, 2D-kV, or CBCT) were compared to calculate the setup errors. For all matches, the ARIA oncology information system with offline review (Varian Medical Systems, Inc., Palo Alto, CA) was used. The example of matching images during IGRT in offline review is shown in Figure 2. The setup errors, systematic error, population systematic error, random error, and population random error in the patients with head and neck cancer were determined. The setup errors or setup displacement is the difference between the actual and planned position of the patient. The mean of the averages and the standard deviation (SD) per axis were calculated. The systematic error (Σ) for an individual patient was represented by mean values of all the displacements. The population systematic error was estimated from the calculation of SD from the values of mean displacement for all patients. The random error (σ) for individual patient was assessed by SD per axis from calculation of systematic displacement. The population random error is the square root of the average of the sum of the SD^2 per axis for all patients. The PTV margin was calculated using Van Herk's formula ($2.5\Sigma+0.7\sigma$) [12-13]. The 3D vector length was calculated for every patient and averaged to give the mean 3D vector of displacement. Subsequently, the setup errors of patients were calculated by comparing the new and reused thermoplastic masks.

Statistical analysis

IGRT was performed according to the schedule. The positioning translations were determined in three directions: vertical, longitudinal, and lateral. Mean and standard deviation (SD) values were calculated for each patient. Individual systematic and random errors were determined. Subsequently, population systematic and random errors were determined. The systematic and random discrepancies in the population were calculated. Statistically significant differences between the two groups were compared. The normality of the data was checked by using the Shapiro–Wilk test. Significant differences between the two groups were determined using the Mann–Whitney U test [14-15]. Differences were considered statistically significant when p value < 0.05 .



Figure 2. An example of (A) CBCT and (B) 2D kV-OBI matching images during IGRT in Offline review image process.

Results

Patient demographics

Eighty patients with head and neck cancer who underwent VMAT treatment with head-and-shoulder masks were included in this study. Patient demographics are summarized in Table 1. The median value BMI was 19.99 kg/m² (range, 13.6 to 37.17 kg/m²). The most common treatment site was the tongue, followed by the nasopharynx, tonsil, and pyriform sinus in 12, 10, 9, and 9 patients, respectively. The median number of images obtained per treatment was 9 (range, 4–22). Finally, 760 images were collected for analysis.

Table 1. Correlation between BMD and various factors.

Characteristics (N = 80)	
Age; years, median (range)	55.5 (25-87)
Gender; Male, n (%)	74 (92.50)
Female, n (%)	6 (7.50)
BMI; kg/m ² , median (range)	19.99 (13.6-37.17)
<18.5, n (%)	25 (31.25)
18.5-23, n (%)	36 (45.00)
≥23, n (%)	19 (23.75)
Imaging acquisition; number, median (range)	9 (4-22)
Imaging modality; n (%)	
EPID	20 (25.0)
2D-kV	6 (7.5)
CBCT	54 (67.5)
Treatment sites; n (%)	
Tongue	12 (15.00)
Nasopharynx	10 (12.50)
Tonsil	9 (11.25)
Pyriform sinus	9 (11.25)

Individual systematic error and individual random error

The individual systematic errors in the vertical, longitudinal, and lateral directions ranged from -3.8 to 2.7 mm, -2.9 to 3.5 mm, and -3.0 to 3.1 mm, respectively, for patients using new masks. The individual systematic error in the vertical, longitudinal, and lateral directions ranged from -4.4 to 2.1 mm, -2.0 to 4.4 mm, and -3.8 to 2.8 mm, respectively, for patients using reused masks. Individual systematic errors in the vertical, longitudinal, and lateral directions are shown in Figure 3.

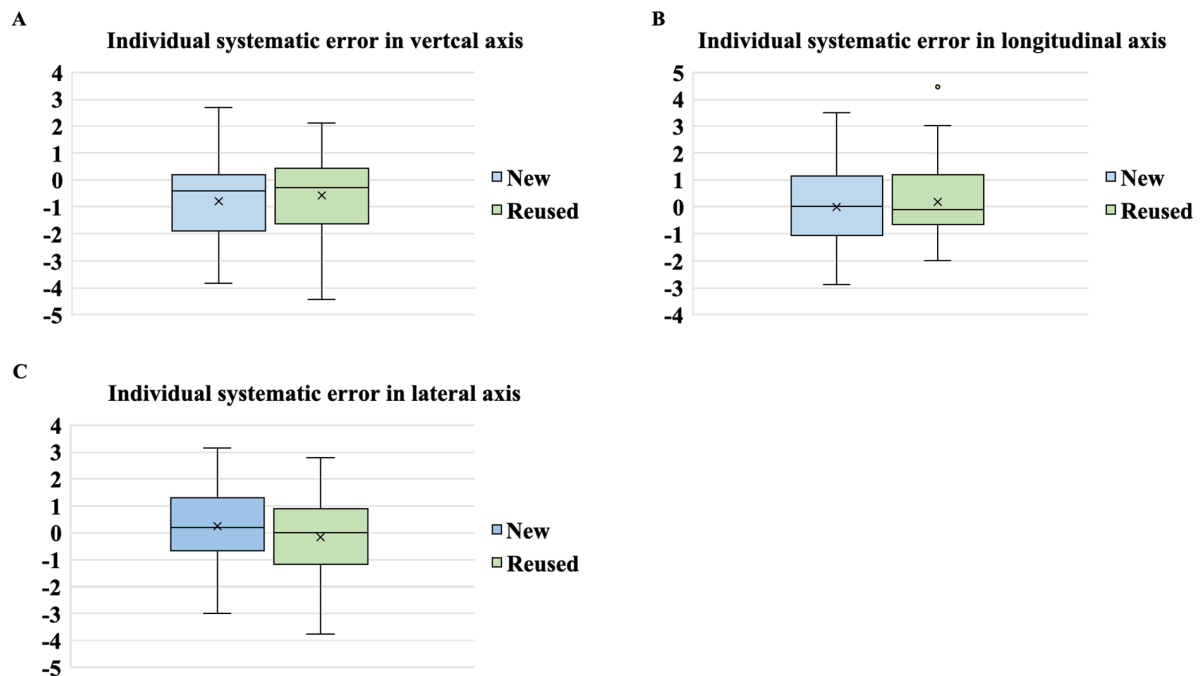


Figure 3. Box plots of the individual systematic error in the (A) vertical, (B) longitudinal, and (C) lateral directions.

The individual random error in the vertical, longitudinal, and lateral directions for patients using new masks ranged from 0.0 to 3.2 mm, 0.5 to 3.4 mm, and 0.5 to 3.3 mm, respectively. The individual random error in the vertical, longitudinal, and lateral directions for patients using reused masks ranged from 0.7 to 3.5 mm, 0.8 to 3.7 mm, and 0.5 to 5.9 mm, respectively. The individual run errors in the vertical, longitudinal, and lateral directions are shown in Figure 4.

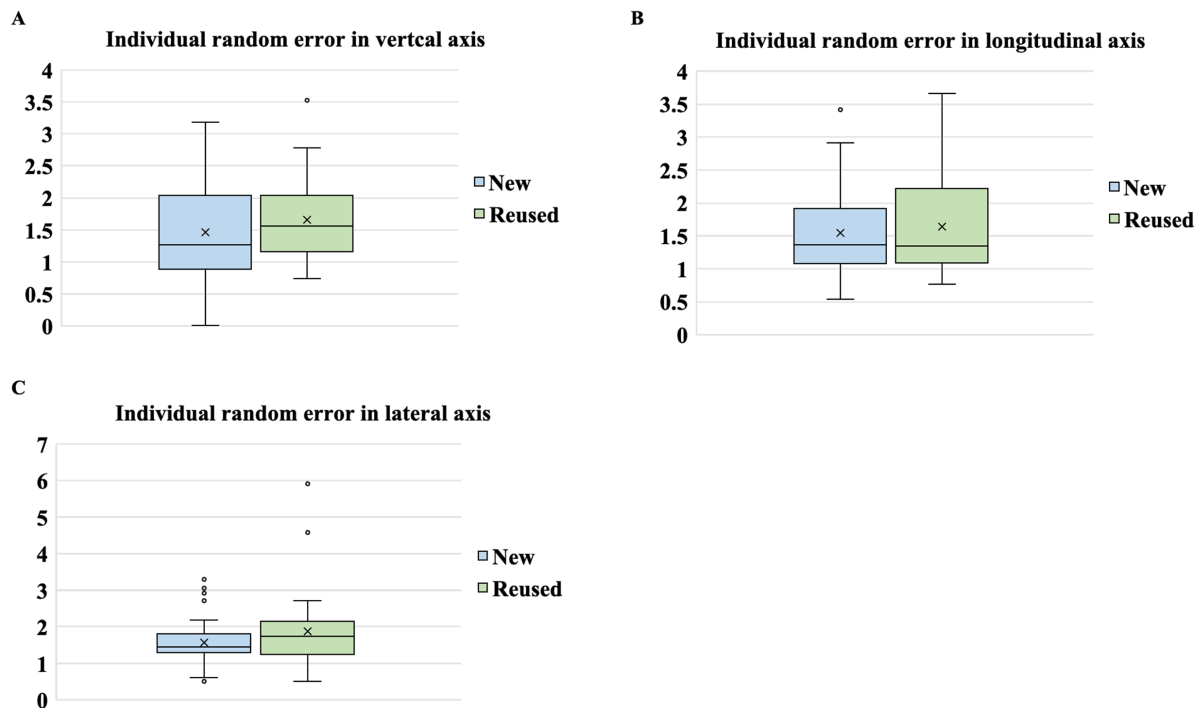


Figure 4. Box plots of the individual random error in the (A) vertical, (B) longitudinal, and (C) lateral directions.

Population systematic error and population random error

The population systematic error for patients using the new masks ranged from 2.02 to 2.27 mm, and for those with reused masks ranged from 1.96 to 2.37 mm. The population random error for patients using the new masks ranged from 1.46 to 1.57 mm and for those with reused ranged from 1.63 to 1.87 mm. The population systematic and random errors and CTV to PTV margins for patients using new and reused masks are shown in Table 2. The 3D vectors for combining setup errors in all directions of the new and reused masks were 6.8 mm and 7.2 mm, respectively.

Table 2. Population systematic and random error and CTV to PTV margins in three directions.

Axis	Population setup error (mm)				CTV to PTV margins (mm)	
	Systematic error		Random error		New	Reuse
	New	Reuse	New	Reuse		
Vertical	2.02	2.37	1.46	1.65	6.072	7.080
Longitudinal	2.27	1.96	1.54	1.63	6.703	6.041
Lateral	2.13	2.33	1.57	1.87	6.424	7.134

Setup error between using the new and reused thermoplastic masks

The differences in systematic and random errors between the new and reused thermoplastic masks are listed in Table 3. No statistically significant difference was found in the individual systematic error along the vertical, longitudinal and lateral directions between the new and reused masks.

Table 3. The difference in systematic and random error between using the new and reuse thermoplastic masks.

Setup error	Axis	Mask	Mean Rank	Mann-Whitney U	p value
Systematic	Vertical	New	-0.805	-0.700	0.486
		Reuse	-0.573		
Systematic	Longitudinal	New	-0.004	-0.595	0.553
		Reuse	0.189		
Systematic	Lateral	New	0.227	1.208	0.231
		Reuse	-0.177		
Random	Vertical	New	1.457	-1.237	0.220
		Reuse	1.651		
Random	Longitudinal	New	1.538	-0.605	0.547
		Reuse	1.630		
Random	Lateral	New	1.566	-1.660	0.101
		Reuse	1.868		

No statistically significant difference was found in individual random error along the vertical, longitudinal and lateral directions between the new and reused masks as shown in Table 3.

Discussion

Eighty patients who underwent VMAT radiotherapy for head and neck lesions with 760 images were analyzed. Setup errors in patients with head and neck cancer using head-and-shoulder thermoplastic masks were determined. Furthermore, the setup errors of patients using new and reused thermoplastic masks were compared. Individual systematic errors for patients using new masks were found to have maximum values of 3.8, 3.5, and 3.1 mm in the vertical, longitudinal, and lateral directions, respectively. For patients using reused masks, systematic errors were determined to have maximum values of 4.4, 4.4 and 3.8 mm in the vertical, longitudinal, and lateral directions, respectively. Individual random errors for patients using new masks had maximum values of 3.2, 3.4 and 3.3 mm in the vertical, longitudinal, and lateral directions, respectively. For patients using reused masks, the random errors in the vertical, longitudinal, and lateral directions were 3.5, 3.7 and 5.9 mm, respectively. The systematic and random error values were comparable. Individual errors of up to 5.9 mm were observed, which is consistent with a previous study that revealed a maximum individual error value of 6.8 mm [16].

The current study observed that the population systematic error for patients using new masks ranged between 2.02 and 2.27 mm. The values for patients using reused masks varied from 1.96 to 2.37 mm. The random population error for patients using the new mask was 1.46 - 1.57 mm. For patients using reused masks, the random error was 1.63 - 1.87 mm. The error in the longitudinal direction was highest for patients using new masks, which is consistent with a previous study that indicated that the error in the longitudinal direction was the largest [13]. However, our findings showed that the error in the vertical direction was highest for patients using reused masks. In a previous study that evaluated setup errors in three directions, it was reported that the setup error was < 3 mm for head and neck radiotherapy treatment, which is consistent with the findings of this study for both patients using new and reused masks. In addition, this research is consistent with previous research, which investigated setup errors in different types of masks, and showed that the setup errors were < 2.4 mm [17-20].

Several mathematical formulae have been introduced for calculating CTV to PTV margins. Van Herk' formula seems to be the most appropriate as it ensures that the patients receive the optimal CTV dose for target coverage. In the present study, the CTV to PTV margins in all directions for new and reused masks were less than 7 and 7.5 mm, respectively. The suggestion when using reused masks is setup margins that are larger than new masks. On analyzing the statistical difference between the two types of masks, it was noted that the individual systematic errors in the vertical, longitudinal, and lateral directions had p values of 0.319, 0.553, and 0.231, respectively. The p-values for the individual random errors in the vertical, longitudinal, and lateral directions were 0.220, 0.855, and 0.161, respectively. Thus, the systemic and random errors associated with the use of new masks and reused masks were not significantly different ($p < 0.05$).

Conclusion

For head and neck radiotherapy, the population setup errors were < 3 mm in all directions. Most errors associated with the reuse of masks were larger than those associated with the new masks. However, the errors were not significantly different. Consequently, they may be considered appropriate alternatives. Nevertheless, in terms of limitations of this study, the reused masks were reused only once because the number of times that a mask was reused influenced its elasticity. Furthermore, the patient setup was corrected in three translational directions without the rotational direction. The results of this research can be used as guidelines for selecting masks for low-income patients or patients who use fundamental techniques.

References

1. Iyer NG, Tan DS, Tan VK, Wang W, Hwang J, Tan NC, et al. Randomized trial comparing surgery and adjuvant radiotherapy versus concurrent chemoradiotherapy in patients with advanced, nonmetastatic squamous cell carcinoma of the head and neck: 10-year update and subset analysis. *Cancer* 2015;121:1599-607. doi:10.1002/cncr.29251.
2. Alterio D, Marvaso G, Ferrari A, Volpe S, Orecchia R, Jereczek-Fossa BA. Modern radiotherapy for head and neck cancer. *Semin Oncol* 2019;46:233-45. doi:10.1053/j.seminoncol.2019.07.002.
3. Corvò R. Evidence-based radiation oncology in head and neck squamous cell carcinoma. *Radiother Oncol* 2007;85:156-70. doi:10.1016/j.radonc.2007.04.002.
4. Sterzing F, Engenhart-Cabillic R, Flentje M, Debus J. Image-guided radiotherapy: a new dimension in radiation oncology. *Dtsch Arztebl Int* 2011;108:274-80. doi:10.3238/arztebl.2011.0274.
5. Dawson LA, Jaffray DA. Advances in image-guided radiation therapy. *J Clin Oncol* 2007 ;25:938-46. doi: 10.1200/JCO.2006.09.9515.
6. Bujold A, Craig T, Jaffray D, Dawson LA. Image-guided radiotherapy: has it influenced patient outcomes? *Semin Radiat Oncol* 2012;22:50-61. doi: 10.1016/j.semradonc.2011.09.001.
7. Kang H, Lovelock DM, Yorke ED, Kriminski S, Lee N, Amols HI. Accurate positioning for head and neck cancer patients using 2D and 3D image guidance. *J Appl Clin Med Phys* 2010;12:3270. doi:10.1120/jacmp.v12i1.3270.
8. Hong TS, Tomé WA, Chappell RJ, Chinnaiyan P, Mehta MP, Harari PM. The impact of daily setup variations on head-and-neck intensity-modulated radiation therapy. *Int J Radiat Oncol Biol Phys* 2005;61:779-88. doi: 10.1016/j.ijrobp.2004.07.696.

9. Sharp L, Lewin F, Johansson H, Payne D, Gerhardsson A, Rutqvist LE. Randomized trial on two types of thermoplastic masks for patient immobilization during radiation therapy for head-and-neck cancer. *Int J Radiat Oncol Biol Phys* 2005;61:250-6. doi: 10.1016/j.ijrobp.2004.04.047.
10. Linthout N, Verellen D, Tournel K, Storme G. Six dimensional analysis with daily stereoscopic x-ray imaging of intrafraction patient motion in head and neck treatments using five points fixation masks. *Med Phys* 2006;33:504-13. doi: 10.1118/1.2165417.
11. Rotondo RL, Sultanem K, Lavoie I, Skelly J, Raymond L. Comparison of repositioning accuracy of two commercially available immobilization systems for treatment of head-and-neck tumors using simulation computed tomography imaging. *Int J Radiat Oncol Biol Phys* 2008;70:1389-96. doi: 10.1016/j.ijrobp.2007.08.035.
12. Badajena A, Raturi VP, Sirvastava K, Hojo H, Ohyoshi H, Bei Y, et al. Prospective evaluation of the setup errors and its impact on safety margin for cervical cancer pelvic conformal radiotherapy. *Rep Pract Oncol Radiother* 2020;25:260-65. doi: 10.1016/j.rpor.2020.02.006.
13. Gupta T, Chopra S, Kadam A, Agarwal JP, Devi PR, Ghosh-Laskar S, et al. Assessment of three-dimensional set-up errors in conventional head and neck radiotherapy using electronic portal imaging device. *Radiother Oncol* 2007;2:44. doi: 10.1186/1748-717X-2-44.
14. SPSS Tutorials. SPSS Shapiro-Wilk Test [software] . 2023 [cited 2023 Aug 19]. Available from: <https://www.spss-tutorials.com/spss-shapiro-wilk-test-for-normality/>
15. Mann Whitney U Test (Wilcoxon Rank Sum Test) [Internet]. 2017 [cited 2023 Aug 19]. Available from: https://sphweb.bumc.bu.edu/otlt/mph-modules/bs/bs704_nonparametric/bs704_nonparametric4.html.

16. Mandair D, Quoc-Anh H, Bets W, Gia J, Roe D, Watchman CJ, et al. Comparison of two thermoplastic immobilization mask systems in daily volumetric image guided radiation therapy for head and neck cancers. *Biomed Phys Eng Express* 2018;4:055007.
17. Gilbeau L, Octave-Prignot M, Loncol T, Renard L, Scalliet P, Grégoire V. Comparison of setup accuracy of three different thermoplastic masks for the treatment of brain and head and neck tumors. *Radiother Oncol* 2001;58:155-62. doi:10.1016/s0167-8140(00)00280-2.
18. Jeon SH, Kim JH. Positional uncertainties of cervical and upper thoracic spine in stereotactic body radiotherapy with thermoplastic mask immobilization. *Radiat Oncol J* 2018;36:122-8. doi:10.3857/roj.2017.00591.
19. Tryggestad E, Christian M, Ford E, Kut C, Le Y, Sanguineti G, et al. Inter- and intrafraction patient positioning uncertainties for intracranial radiotherapy: a study of four frameless, thermoplastic mask-based immobilization strategies using daily cone-beam CT. *Int J Radiat Oncol Biol Phys* 2011;80:281-90. doi:10.1016/j.ijrobp.2010.0.
20. Rosenfelder NA, Corsini L, McNair H, Pennert K, Aitken A, Lamb CM, et al. Comparison of setup accuracy and intrafraction motion using stereotactic frame versus 3-point thermoplastic mask-based immobilization for fractionated cranial image guided radiation therapy. *Pract Radiat Oncol* 2013; 3:171-9. doi:10.1016/j.prro.2012.06.004.

Original Article

Acute changes of superior mesenteric artery pressure after intraarterial bolus injection of prostaglandin-E1

Yukihiro Hama, M.D., Ph.D.

From Department of Radiology, Tokyo Edogawa Cancer Center, Edogawa Hospital,
2-24-18 Higashikojiwa, Edogawaku, Tokyo 133-0052, Japan.

Address correspondence to Y.H.(yjhama2005@yahoo.co.jp)

Received 22 January 2023; revised 21 August 2023; accepted 21 August 2023
doi:10.46475/aseanjr.v24i2.206

Abstract

Background: A bolus injection of prostaglandin-E1 (PGE1) into the superior mesenteric artery (SMA) immediately before SMA-portography can effectively visualize the portal vein.

Objective: The purpose of this study was to obtain basic pharmacoangiographical data and evaluate the hemodynamic changes following intra-arterial bolus injection of PGE1.

Materials and Methods: Forty-four consecutive patients undergoing transcatheter arterial chemoembolization (TACE) for liver cancer were retrospectively evaluated. SMA-portography was performed prior to TACE. An intra-arterial bolus injection of PGE1 was performed immediately before SMA-portography. Both SMA pressure and left brachial artery pressure were measured before, 1, 2, 3, 4, and 5 minutes after SMA-portography.

Results: Systolic pressure in the SMA decreased significantly 3 minutes after SMA-portography and remained low for 5 minutes. The maximum reduction rates in systolic and diastolic blood pressure in the SMA were 4.8% (4 minutes after SMA-portography) and 6.8% (5 minutes after SMA-portography), respectively. The left brachial artery pressure decreased similarly to the SMA. There were no significant changes in pulse pressure before or after PGE1 injection in either the SMA or brachial arteries.

Conclusion: A bolus injection of PGE1 into the SMA was shown to decrease blood pressure in the SMA and brachial arteries, but the pulse pressure remained constant.

Keywords: Interventional radiology, Pharmacodynamics, Catheterization.

Introduction

Superior mesenteric arterial portography (SMA-portography) or CT during arterial portography (CTAP) allows noninvasive visualization of blood flow to normal liver tissue as well as portosystemic shunts [1,2]. Prostaglandin-E1 (PGE1), a vasodilator, binds to prostaglandin receptors on smooth muscle cells which triggers the adenylate cyclase conversion of adenosine triphosphate to cyclic adenosine monophosphate (cAMP) [3]. Elevated cAMP results in reduction of cytosolic calcium and relaxation of smooth muscle. PGE1 is administered intra-arterially immediately before angiography to improve the contrast effect on the portal vein, but there are few data on arterial pressure change after bolus injection of PGE1 [4]. The purpose of this study was to obtain basic pharmacoangiographical data and evaluate the hemodynamic changes following intra-arterial bolus injection of PGE1.

Materials and methods

All procedures were in accordance with the ethical standards of the institutional and/or national research committee and with the 1964 Helsinki Declaration and its later amendments or comparable ethical standards. Our institutional review board granted a waiver of consent for this retrospective chart review study. Informed consent was obtained from the patients for the use of clinical data.

Patients

We retrospectively reviewed endovascular treatment charts of 44 consecutive patients (M/F 33/11) who had undergone transcatheter arterial chemoembolization (TACE) for liver cancer in the past 10 months at our institution. The median age of the patients was 68 years (interquartile range [IQR] 61-73 years). Of the 44 patients, 28 (63.6%) were diagnosed with hypertension but had stopped taking antihypertensive medication 24 hours prior to the angiogram.

Data collection

Approximately 10 mL of local anesthetic agent (1% lidocaine without epinephrine) was injected around the right femoral artery site, which was cannulated with Seldinger technique, and SMA-portography was performed prior to TACE. A 4-Fr sheath 11 cm in length and a 4-Fr shepherd hook catheter (Clinical Supply, Hashima, Japan) was used. Prior to SMA-portography, 5 micrograms of PGE1 (Alprostadil, Mitsubishi Tanabe Pharma, Osaka, Japan), diluted in 10 ml saline was injected intra-arterially through the catheter. Before intra-arterial administration of PGE1 and 1, 2, 3, 4, and 5 minutes after SMA-portography, SMA pressure was measured using a monitoring device (DX-300, NIHON KOHDEN, Tokyo, Japan), while blood pressure was simultaneously measured in the left upper arm (brachial artery) with a sphygmomanometer every minute. The patients received iodine-based contrast media at a flow rate of 4-5 mL/s and a total dose of 20-30 mL. After confirming portal venous flow on SMA-portography, TACE was performed. Once the 4-Fr guiding catheter was in place, the inner infusion catheter was inserted through the guiding catheter and advanced to the precise location within the artery that supplies the tumor. Then, chemotherapy drugs,

mixed with iodized oil, were injected through the infusion catheter into the tumor-supplying artery. After the mixture was delivered, embolic agents such as microspheres or gelatine sponge particles were injected through the infusion catheter.

Statistical analysis

Data were expressed as mean +/- and standard deviation (SD). Blood pressure and pulse pressure before PGE1 administration and after SMA-portography were compared using a paired t-test. All statistical tests were 2-sided, and group differences were considered statistically significant if $p < 0.05$.

Results

The systolic pressure in the SMA before PGE1 administration was 148.0 +/- 21.8 mmHg (IQR 127.0-167.3 mmHg), whereas at 1, 2, 3, 4, and 5 minutes after SMA-portography, it was 145.1 +/- 20.2 mmHg ($p = 0.23$), 143.1 +/- 21.6 mmHg ($p = 0.07$), 141.8 +/- 20.9 ($p < 0.05$) mmHg, 140.9 +/- 22.2 mmHg ($p < 0.05$), and 141.1 +/- 19.1 mmHg ($p < 0.05$), respectively (Figure 1a).

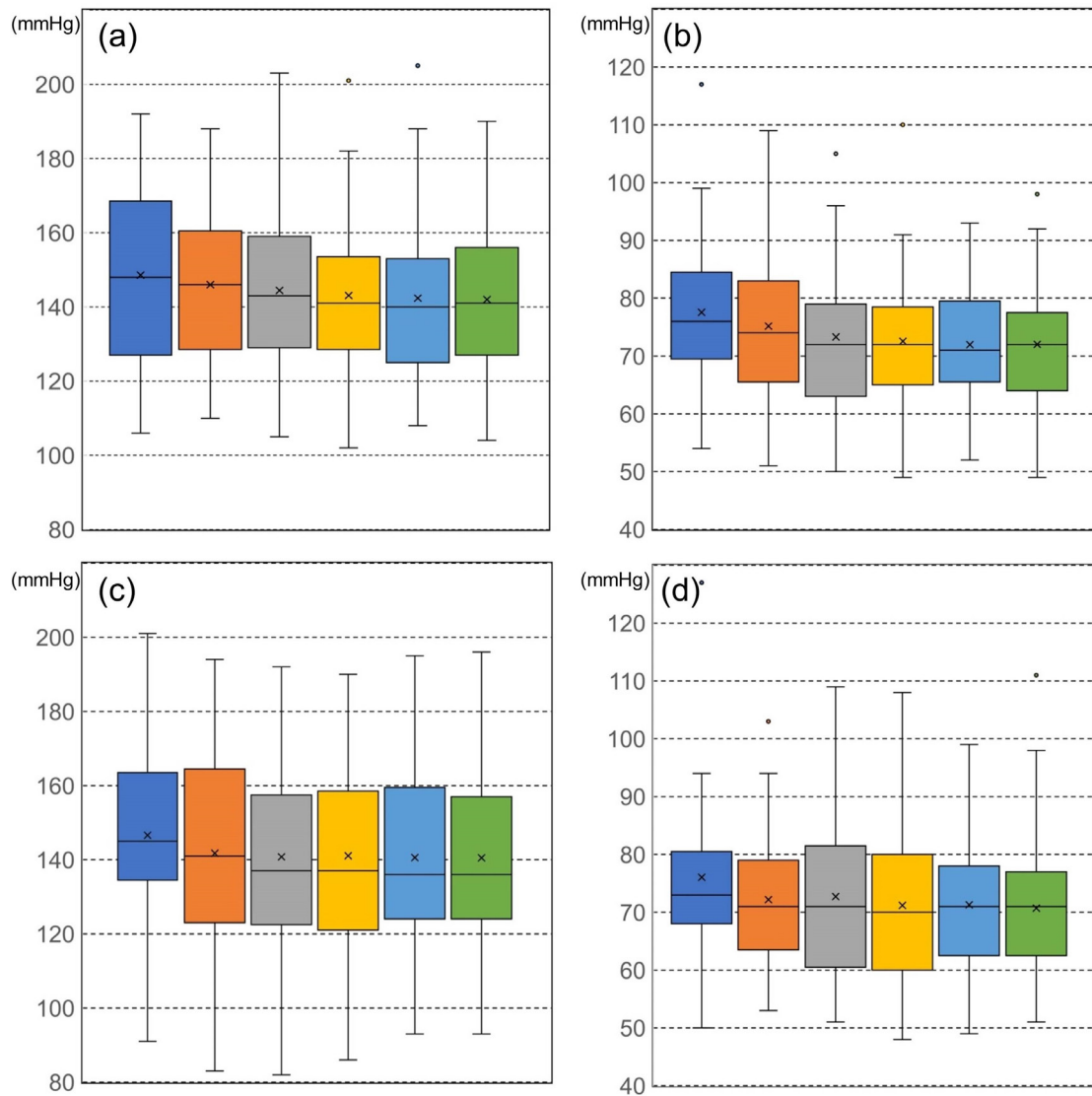


Figure 1. Box plots of blood pressure before intra-arterial injection of prostaglandin-E1 (blue) and 1 (dark brown), 2 (gray), 3 (yellow), 4 (light blue), and 5 (green) minutes after superior mesenteric artery-portography, (a) Systolic pressure in the superior mesenteric artery, (b) Diastolic pressure in the superior mesenteric artery, (c) Systolic pressure in the left brachial artery, (d) Diastolic pressure in the left brachial artery, "x" marks correspond to the means. The central horizontal bars are the medians. The lower and upper limits of the box are the first and third quartiles, respectively. Points above or below the whiskers' upper and lower bounds are outliers.

The diastolic pressure in the SMA before PGE1 administration was 76.7 +/- 12.3 mmHg (IQR 69.8-82.3 mmHg), whereas at 1, 2, 3, 4, and 5 minutes after SMA-portography, it was 74.4 +/- 12.3 mmHg ($p = 0.07$), 72.6 +/- 12.1 mmHg ($p < 0.05$), 71.7 +/- 12.0 mmHg ($p < 0.05$), 71.5 +/- 10.7 mmHg ($p < 0.05$), and 71.4 +/- 10.7 mmHg ($p < 0.05$), respectively (Figure 1b). The left brachial artery systolic pressure was 146.1 +/- 24.7 mmHg (IQR 135.3-159.0 mmHg) before PGE1 administration, whereas it was 140.9 +/- 27.4 mmHg ($p = 0.07$), 139.7 +/- 25.4 mmHg ($p < 0.05$), 140.0 +/- 25.6 mmHg ($p < 0.05$), 139.8 +/- 24.2 mmHg ($p < 0.05$), 139.9 +/- 23.9 mmHg ($p < 0.05$) at 1, 2, 3, 4 and 5 minutes after SMA-portography, respectively (Figure 1c). The left brachial artery diastolic pressure was 74.9 +/- 11.8 mmHg (IQR 68.0-80.0 mmHg) before PGE1 administration, whereas it was 71.5 +/- 11.2 mmHg ($p < 0.05$), 71.9 +/- 12.8 mmHg ($p < 0.05$), 70.4 +/- 12.3 mmHg ($p < 0.05$), 70.7 +/- 12.1 mmHg ($p < 0.05$), 70.1 +/- 11.7 mmHg ($p < 0.05$) at 1, 2, 3, 4 and 5 minutes after SMA-portography, respectively (Figure 1d). The maximum reduction rates in systolic and diastolic blood pressure in SMA were 4.8% (4 minutes after SMA-portography) and 6.8% (5 minutes after SMA-portography), respectively. The maximum reduction rates in systolic and diastolic blood pressure in the left brachial artery were 4.4% (2 minutes after SMA-portography) and 6.4% (5 minutes after SMA-portography), respectively. The pulse pressure in the SMA before PGE1 administration was 71.3 +/- 14.8 mmHg, whereas at 1, 2, 3, 4, and 5 minutes after SMA-portography, it was 70.7 +/- 11.7 mmHg ($p = 0.76$), 70.5 +/- 12.3 mmHg ($p = 0.73$), 70.1 +/- 12.6 ($p = 0.61$) mmHg, 69.4 +/- 14.5 mmHg ($p = 0.44$), and 69.7 +/- 11.1 mmHg ($p = 0.43$), respectively. The pulse pressure in the left brachial artery before PGE1 administration was 71.2 +/- 21.2 mmHg, whereas at 1, 2, 3, 4, and 5 minutes after SMA-portography, it was 69.4 +/- 19.8 mmHg ($p = 0.50$), 67.8 +/- 16.7 mmHg ($p = 0.19$), 69.6 +/- 15.9 ($p = 0.54$) mmHg, 69.1 +/- 15.3 mmHg ($p = 0.42$), and 69.7 +/- 16.1 mmHg ($p = 0.58$), respectively. After intra-arterial injection of PGE1, systolic and diastolic blood pressure decreased significantly in both SMA and brachial arteries, but pulse pressure did not change significantly.

Discussion

PGE1, also known as alprostadil, has been used to treat patent ductus arteriosus [5], erectile dysfunction [6], thromboangiitis obliterans [7], arteriosclerosis obliterans [8], and skin ulcers caused by diabetes [9]. Because of the safety and rapid vasodilating effect of PGE1, SMA-angiography is performed by bolus injection of PGE1 into the SMA immediately before angiography. Intra-arterial bolus injection of PGE1 induces intestinal peristalsis, which may be complicated by abdominal discomfort, nausea, and vomiting; however, there have been no studies examining acute hemodynamic changes in the SMA or peripheral arteries. As far as we know, this is the first report on changes in SMA and brachial arterial blood pressure after intra-arterial bolus injection of PGE1. According to the results of this study, both SMA and brachial systolic pressure dropped by about 5% after 3 minutes of intra-arterial injection of PGE1. SMA and brachial blood pressure, both systolic and diastolic, were comparable before and 5 minutes after administration. This indicates that PGE1 acts on arteries throughout the whole body and lowers blood pressure, rather than specifically on the target artery in this case SMA.

This study has several strengths. First, there are no reports measuring changes in both peripheral (brachial) and central (superior mesenteric artery) blood pressure after intra-arterial bolus injection of PGE1. The results of this study indicate that PGE1 nonspecifically lowers peripheral and central blood pressure within 3 minutes and maintains its hypotensive effect for at least 5 minutes after injection. Second, despite the high concentration of PGE1 infused into the SMA, there was no significant difference in the blood pressure lowering effect between the brachial artery and SMA. This indicates that temporarily high concentrations of PGE1 passing through an artery do not selectively decrease the blood pressure in that artery. Central blood pressure may be estimated by measuring peripheral blood pressure after PGE1 is injected into the central artery. Knowing that a blood pressure drop of about 5% occurring after intra-arterial infusion of PGE1 would be helpful in differentiating it from other causes of hypotension (e.g., vagal reflex, anaphylactic shock, etc.). This piece of knowledge of the pharmacological effects of PGE1 may contribute to the safe performance of angiography.

This study has some limitations. First, all the subjects in this study were liver cancer patients, and changes in arterial blood pressure in healthy subjects were not evaluated. However, since invasive angiography is not usually performed on healthy subjects, the lack of data on healthy subjects is not a limitation. Second, intestinal blood flow was not directly measured, and it remains a mystery how much the increase in intestinal blood flow contributed to the decrease in peripheral and central arterial blood pressure. The effect of PGE1 on cardiac function after intra-arterial infusion into the central arteries has not yet been evaluated. The effect of intra-arterial bolus injection of PGE1 on cardiovascular hemodynamics remains a topic for future research.

Conclusion

In conclusion, a single cohort study cannot be generalized to others without further scientific validation; however, after intra-arterial bolus infusion of PGE1, both systolic and diastolic blood pressures in the SMA and brachial artery were lower than before PGE1 infusion and remained lower for at least 5 minutes after infusion, while pulse pressure remained constant.

Acknowledgements

The author would like to thank Dr. Yutaka Sakurai for statistical analysis and is grateful to Dr. Shoichi Kusano for data collection and collaboration on the early stages of this work.

References

1. Redvanly RD, Chezmar JL. CT arterial portography: technique, indications and applications. *Clin Radiol* 1997;52:256-68. doi: 10.1016/s0009-9260(97)80051-7.
2. Soyer P. CT during arterial portography. *Eur Radiol* 1996;6:349-57. doi: 10.1007/BF00180609.
3. Owen NE. Effect of prostaglandin E1 on DNA synthesis in vascular smooth muscle cells. *Am J Physiol* 1986;250(4 Pt 1):C584-8. doi: 10.1152/ajpcell.1986.250.4.C584.
4. Davidovic LB, Vranes MR, Lotina SI, Cernak IF, Velimirovic DB, Stojanov PL, et al. Intraarterial perfusion of prostaglandin E1 after lumbar sympathectomy or reconstruction on femoropopliteal segment. *Int Angiol* 1991;10:178-81.
5. Akkinapally S, Hundalani SG, Kulkarni M, Fernandes CJ, Cabrera AG, Shivanna B, et al. Prostaglandin E1 for maintaining ductal patency in neonates with ductal-dependent cardiac lesions. *Cochrane Database Syst Rev* 2018;2: CD011417. doi: 10.1002/14651858.CD011417.pub2.
6. Urciuoli R, Cantisani TA, Carlini M, Giuglietti M, Botti FM. Prostaglandin E1 for treatment of erectile dysfunction. *Cochrane Database Syst Rev* 2004;(2): CD001784. doi: 10.1002/14651858.CD001784.pub2.
7. Cacione DG, Macedo CR, do Carmo Novaes F, Baptista-Silva JC. Pharmacological treatment for Buerger's disease. *Cochrane Database Syst Rev* 2020;5:CD011033. doi: 10.1002/14651858.CD011033.pub4.
8. Ambrus JL, Taheri P, Killion D, Donaldson G. Clinical experience with prostaglandin E1 in the treatment of arteriosclerosis obliterans. A preliminary report. *J Med* 1983;14:1-15.
9. Miyata T, Yamada N, Miyachi Y. Efficacy by ulcer type and safety of lipo-PGE1 for Japanese patients with diabetic foot ulcers. *J Atheroscler Thromb* 2010;17:805-16. doi: 10.5551/jat.3608.

Case Report

Superficial siderosis presenting as hemiparesis in a paediatric patient with congenital Factor V deficiency – A case report

Pushkar Mendiratta, M.D., D.N.B.

Samaresh Sahu M.D., D.N.B., F.R.C.R., M.N.A.M.S.

Aneesh Mohimen, M.D., D.M.

From Department of Radiodiagnosis and Imaging, Command Hospital Air Force,
Bangalore, India.

Address correspondence to P.M.(email: pushkar_indian@yahoo.co.in)

Received 23 October 2021; revised 8 May 2023; accepted 8 May 2023
doi:10.46475/aseanj. v24i2.157

Abstract

Superficial siderosis is a rare abnormality caused by deposition of hemosiderin in the subpial or subarachnoid spaces of the brain, cranial nerves, and spinal cord. It results from chronic repetitive bleeding in the subpial/subarachnoid space. Magnetic resonance imaging of the brain is the diagnostic modality of choice. We describe a rare case of an 18-month-old male, a known case of congenital Factor V deficiency, who presented with recurrent vomiting, irritability and right-sided hemiparesis. On Magnetic resonance imaging, there was hypointense coating of the surface of the brainstem and cerebellum with ventricular dilatation. This case emphasizes the fact that superficial siderosis should be specifically looked for when evaluating a patient with a history of previous intracranial bleed followed by a thorough search for the source of the hemorrhage.

Keywords: Superficial siderosis, Paediatric, Magnetic Resonance Imaging, Factor V, Hemosiderin, Intracranial bleed, Subarachnoid bleed.

Introduction

Superficial siderosis is a rare abnormality caused by deposition of hemosiderin in the subpial or subarachnoid layers of the brain, cranial nerves, and spinal cord. It results from chronic repetitive bleeding in the subpial or subarachnoid spaces which is sometimes difficult to differentiate on imaging. The resulting pathological changes include reactive gliosis, neuronal loss and demyelination which result in a progressive debilitating clinical disorder characterised by a clinical triad of sensorineural hearing loss, cerebellar ataxia and pyramidal signs [1]. Headache and seizures have been reported in the paediatric population.

We present a rare case of superficial siderosis in a child with known congenital Factor V deficiency with a previous history of subarachnoid hemorrhage. The description of the findings associated with the case is followed by a brief account of the pathological changes, imaging findings and management of such patients.

Case summary

An 18-month-old male child, a known case of congenital Factor V deficiency developed recurrent episodes of vomiting and irritability followed by right-sided hemiparesis. On a neurological examination, motor power was grade 3 in all groups of muscles on the right side. The patient was also noted to have a tense anterior fontanelle with increased occipito-frontal circumference of 54 cm which was more than the 97th percentile for the age of the patient. The child was born after a full-term (gestational age of 38 weeks) and normal delivery, without a history of birth trauma or any other perinatal complication. Parents gave the history of the child having a subarachnoid hemorrhage at 2½ months of age which was diagnosed by a Magnetic Resonance Imaging (MRI) of brain and was managed conservatively. The images of this MRI were not available for review.

The patient underwent MRI of the brain at our hospital on a Siemens Avanto 1.5T machine. Axial T2 weighted turbo spin echo (TSE), gradient echo sequence (GRE); Coronal T2 weighted TSE; sagittal T2 weighted TSE, T1 MPRAGE (Magnetization Prepared Rapid Acquisition Gradient Echo) and 3D-fast TSE Sampling Perfection with Application optimized Contrasts using different flip angle Evolution (SPACE) sequences with a slice thickness of 5 mm and gap of 0.5 mm were performed. MRI revealed linear uniform hypointense coating of the surface of the brainstem, base and foliae of cerebellum bilaterally on T2 weighted and GRE images (Red arrows; Figure 1a and 1b). In addition, there was associated dilatation of both lateral ventricles with intraventricular blood CSF levels noted bilaterally (Red arrows; Figure 2a and 2b). There was also dilatation of the third ventricle noted (green arrow Figure 2b). These findings are consistent with superficial siderosis, occurring in this case as a consequence of previous subarachnoid hemorrhage, with associated hydrocephalus. The raised intracranial pressure due to hydrocephalus causing the symptoms, was relieved by ventriculoperitoneal shunting. The patient was managed with fresh frozen plasma infusions to replenish the factor V. The patient was advised to undergo a regular follow-up both with the neurosurgeon and the hematologist.

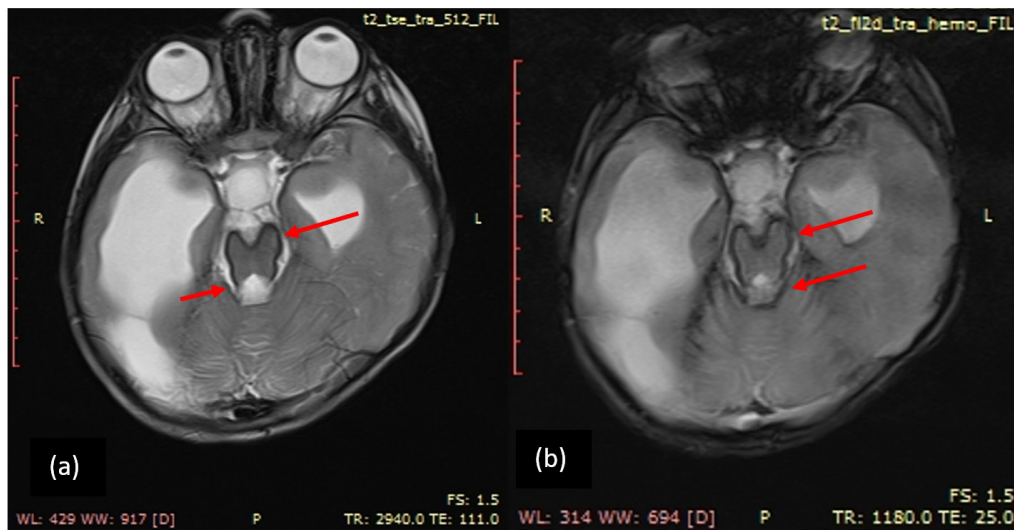


Figure 1. (a) Axial T2 weighted image and (b) axial GRE image at the level of brainstem and cerebellum shows Hypointensity involving brainstem, base and foliae of cerebellum (red arrows).

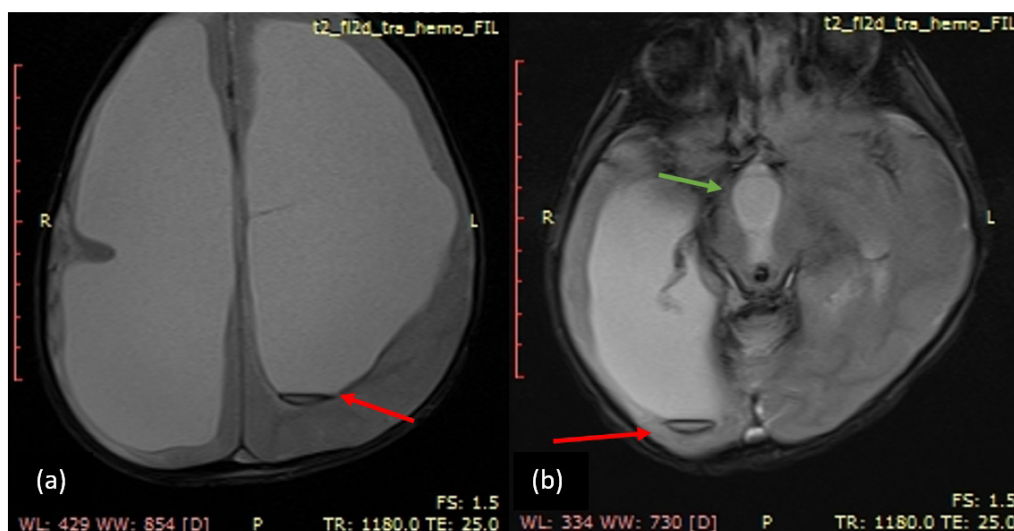


Figure 2. (a)-(b) Gross dilatation of both lateral ventricles with blood fluid levels in the occipital horns of both the lateral ventricles (red arrows). Dilatation of third ventricle (green arrow).

Discussion

Superficial siderosis is a rare clinical condition which results from chronic or repeated bleeding in the subpial or subarachnoid spaces. This leads to hemosiderin deposition in the subpial layer of the brain and spinal cord causing gradual and progressive neurologic deterioration. The common conditions that are associated with the development of superficial siderosis include trauma and neurosurgery. Less common conditions are hemorrhagic neoplasms, vascular malformations, hemorrhagic vasculopathies and cerebral amyloid angiopathy [2]. In up to one third of the cases, etiology remains unknown even after extensive relevant diagnostic imaging.

There are two clinical and pathological types - 'Classical' superficial siderosis which primarily affects the infratentorial regions and the spinal cord and 'cortical' superficial siderosis, which primarily affects the supratentorial compartment and cerebral convexities. The classical subtype has predilection for superior cerebellar vermis, cerebellar folia, brainstem, spinal cord, nerve roots, cranial nerves I and VIII. It is characteristically associated with the clinical triad of slowly progressive sensorineural hearing impairment, cerebellar ataxia and pyramidal signs. Cortical superficial siderosis (cSS), on the other hand, predominantly affects the cortical sulci over the cerebral convexities, sparing the brainstem, cerebellum and spinal cord. It is generally seen in association with cerebral amyloid angiopathy and reversible cerebral vasoconstriction syndrome [3].

The intracellular process of formation of hemosiderin is albeit a complex one too. The heme is broken down to free iron by enzyme heme-oxygenase. Free iron is responsible for cell injury. The free iron not only upregulates ferritin production but also the persistent free iron exposure changes the ferritin production from heavy subunit to light subunit which allows long-term iron storage as hemosiderin deposits. Hemosiderin being insoluble, it gets pulled to the subpial surface by natural gravitational force. While storage in the form of hemosiderin is protective in the short term, prolonged exposure which occurs in repetitive episodes of hemorrhage leads to neuronal loss, reactive gliosis and demyelination [4].

The classical clinical triad consists of sensorineural hearing loss, cerebellar ataxia and pyramidal signs [5]. Symptoms described in paediatric population include seizures, bladder disturbance, headache and extraocular motor palsies while other rare symptoms described in literature are memory loss, backache, bilateral sciatica, anosmia, anisocoria and lower motor neuron signs. However, there is limited literature on the study of the effect of superficial siderosis on neurodevelopmental outcomes. One such retrospective study conducted with 7 infants showed no obvious neurodevelopmental implications of superficial siderosis. However, associated intra/periventricular hemorrhage has been found to be linked with neurosensory impairment and alterations in auditory brain stem responses [6]. The rarity of superficial siderosis in paediatric population is highlighted by limited reported studies and case reports available; however, superficial siderosis developing as a result of subarachnoid bleeding due to factor V deficiency was not encountered on literature research.

Hemosiderin deposition on the surface of neuroparenchyma creates a superficial brownish-yellowish pigmentation, which has shown to have a predilection for superior cerebellar vermis, crests of the cerebellar folia, basal frontal lobe, temporal cortex, brainstem, spinal cord, nerve roots and cranial nerves I and VIII [7]. However, the peripheral nervous system is not involved in superficial siderosis.

Before modern imaging techniques were available, diagnosis could be made on autopsy only. Non-contrast computerized tomography (NCCT) of the head and spine may occasionally point towards the etiology in the form of evidence of trauma or surgery. It may also show atrophy of the cerebellum or rarely hyperattenuated rim along the affected neuroparenchymal surface, which can occur due to calcification at sites of long-standing hemosiderin deposition.

MRI of the brain is the investigation of choice for diagnosing this condition. T2 weighted spin echo images and gradient-echo images (or susceptibility weighted images) show hemosiderin deposition of superficial siderosis fairly well. However, FLAIR images may be useful for identifying acute subarachnoid hemorrhage.

T2-weighted MRI images show a rim of hypointensity around the affected areas predominantly the cerebellum and brain stem. The other preferentially involved areas also show a rim of hypointensity including the cranial nerves. Cerebellar atrophy is often noted with the superior cerebellar vermis and anterior cerebellar hemispheres preferentially involved. A recent episode of sub-arachnoid hemorrhage may appear as a hyperintense rim owing to the presence of methemoglobin. Gradient-echo imaging (GRE) or susceptibility-weighted imaging (SWI) is the most sensitive sequence to look for superficial siderosis which appears as hypointense rim due to magnetic susceptibility effects on these sequences. This effect is also known as blooming artefact, which conspicuously shows the hypointense rim. T1-weighted images may show a subtle partially corresponding hyperintense rim. There is no enhancement noted at the sites of hemosiderin deposition. Tissue damage associated with superficial siderosis may be detectable as atrophy and abnormal signal intensity of the involved regions [8].

The extent and distribution of MRI findings may not correlate with the clinical severity. However, extensive involvement of the brain and spinal cord is usually associated with clinical symptoms.

When superficial siderosis is suspected or diagnosed on MRI, a careful and meticulous search for the source of the hemorrhage should be sought. Hence, in cases where the cause of recurrent bleeding is obscure, additional sequences/ diagnostic techniques may be implemented to look for the source. The routine brain MRI protocol includes T1 weighted, T2 weighted, FLAIR and GRE/SWI sequences. Additional sequences/diagnostic techniques include four-vessel cerebral catheter angiography, spinal angiography, CT myelogram, MR angiography, whole spine MRI, MR myelography and MR cisternography.

The imaging differential diagnoses include normal leptomeningeal melanin, brain surface venous plexuses and bounce point artefact which occurs due to phase cancellation of the MR signals in boundary pixels. Rare imaging differential diagnosis includes meningioangiomas which is a meningovascular hamartomatous cortical lesion in nodular or gyriform configuration and

neurocutaneous melanosis which is a rare phakomatosis with meningeal melanocytosis/meningeal melanomatosis on imaging. Normal leptomeningeal melanin appears generally as a variably thick hypointense rim on the ventral surface of the medulla oblongata on T2-weighted spin-echo images [9].

Treatment consists of obliteration of the bleeding site, which may be the cause of future repetitive bleeding. Medical management has been attempted with corticosteroids, chelating agents like desferrioxamine or trientine but with limited success. CSF shunting may be done as it has been thought to reduce prolonged exposure to blood promoting faster clearance of toxins from CSF.

Conclusion

This rare case of superficial siderosis due to congenital factor V deficiency in a paediatric patient reinforces the importance of keeping an eye out for superficial siderosis in any patient with a history of previous subarachnoid bleed. The recognition of the source of bleed has a vital implication in the management of such patients. Accurate radiological diagnosis and early intervention may benefit the patient in the form of reduced morbidity and mortality.

References

1. Kumar N. Neuroimaging in superficial siderosis: an in-depth look. *AJNR Am J Neuroradiol* 2010; 31:5–14. doi: 10.3174/ajnr.A1628.
2. Linn J, Halpin A, Demaerel P, Ruhland J, Giese AD, Dichgans M, et al. Prevalence of superficial siderosis in patients with cerebral amyloid angiopathy. *Neurology* 2010;74:1346-50. doi: 10.1212/WNL.0b013e3181dad605.
3. Charidimou A, Linn J, Vernooij MW, Opherk C, Akoudad S, Baron JC, et al. Cortical superficial siderosis: detection and clinical significance in cerebral amyloid angiopathy and related conditions. *Brain* 2015;138 (Pt 8):2126–39. doi: 10.1093/brain/awv162.
4. Nanda S, Sharma SG, Longo S. Superficial siderosis – mechanism of disease: an alternative hypothesis. *Ann Clin Biochem* 2010;47(Pt 3):275–8. doi: 10.1258/acb.2010.009226.
5. Cheah WH. Superficial siderosis. *Appl Radiol* 2019;8:40-1.
6. Yilmaz U, Meyer S, Gortner L, Körner H, Türkyilmaz M, Simgen A, et al. Superficial siderosis after doi: 10.3174/ajnr.A4935.
7. Koeppen AH, Michael SC, Li D, Chen Z, Cusack MJ, Gibson WM, et al. The pathology of superficial siderosis of the central nervous system. *Acta Neuropathol* 2008;116:371–82. doi: 10.1007/s00401-008-0421-z.
8. Posti JP, Juvela S, Parkkola R, Roine S. Three cases of superficial siderosis of the central nervous system and review of the literature. *Acta Neurochir* 2011;153:2067–73. doi: 10.1007/s00401-008-0421-z.
9. Gebarski SS, Blaivas MA. Imaging of normal leptomeningeal melanin. *AJNR Am J Neuroradiol* 1996; 17:55–60.

Pictorial Essay

Pediatric imaging of neuroblastoma-From classic to atypical

Michal Scolnik, M.D. ⁽¹⁾

Luda Glozman M.D. ^{(1), (2)}

Noa Mandel-Shorer, M.D. ⁽³⁾

Michalle Soudack Ben-Nun M.D. ⁽⁴⁾

Anat Ilivitzki, M.D. ^{(1), (5)}

From ⁽¹⁾ Department of Radiology, Resident, Rambam Health Care Campus, Haifa, Israel,

⁽²⁾ Pediatric Radiology Unit, ⁽³⁾ Department of Pediatric Hematology-Oncology,

Ruth Rappaport Children's Hospital, Rambam Health Care Campus, Haifa, Israel,

⁽⁴⁾ Pediatric Imaging Section Head, Department of Diagnostic Imaging, Sheba Medical Center, Ramat Gan, Israel,

⁽⁵⁾ The Bruce Rappaport Faculty of Medicine, Technion Israel Institute of Technology, Haifa, Israel.

Address correspondence to M.S.(email: michal.scolnik@gmail.com)

Received 5 April 2023; revised 9 June 2023; accepted 19 June 2023
doi:10.46475/aseanjr.v24i2.313

Abstract

Neuroblastoma (NB) is the most common extracranial solid tumour in children, accounting for approximately eight percent of paediatric cancer and fifteen percent of pediatric cancer deaths. Reaching a correct and timely diagnosis is extremely important, especially in aggressive NB. Prognosis and treatment are based on tumour biology and genetics, patient age and perhaps most importantly, disease stage. The current staging system relies heavily on imaging, and this pictorial essay provides a description of the radiological features of NB, from classic to atypical, and the modalities used to help confirm the diagnosis and staging of NB. Our aim is to provide radiologists with a comprehensive collection of presentations of NB, to help improve diagnostic accuracy and decrease time to diagnose.

Keywords: Neuroblastoma, Imaging, Pediatric, Radiology.

Introduction

Neuroblastoma (NB) is the commonest extracranial solid tumour of the pediatric population [1,2], and the most common neonatal solid tumour [3]. The median age at diagnosis is about 16 months [1], and 90% of the cases are diagnosed by the age of six [2]. NB accounts for eight percent of pediatric cancers, but causes about fifteen percent of childhood cancer deaths [4]. It is mostly diagnosed as a painless abdominal mass; however, it is often metastatic and symptomatic [2]. As the name suggests, NB is derived from neural crest cells of the sympathetic nervous system; thus, it may be found in a sympathetic tissue anywhere in the body [2,4]. Almost half of the NB cases originate in the adrenal glands, and other common sites are sympathetic ganglions of the retroperitoneum and chest [1,5]. The factors influencing prognosis are tumour biology and genetics, the patient's age and, perhaps most importantly, the disease stage [1,2].

Reaching a correct and timely diagnosis is extremely important, especially in aggressive NB. Our aim is to provide radiologists with a comprehensive collection of imaging presentations of NB, to help improve diagnostic accuracy and decrease time to diagnose.

Staging systems

Historically, NB staging was defined by the International Neuroblastoma Staging System (INSS) (Table 1) [1], and although since supplanted, INSS is still used and reported in the literature [3,6]. In 2009, an improved staging system was proposed by the International Neuroblastoma Risk Group (INRG), a conglomerate of investigators from major cooperative oncology groups from North America, Australia–New Zealand, Germany, Japan and China [1], which also includes the Children's Oncology Group (COG), Children's Cancer Group (CCG) and

Pediatric Oncology Group (POG) [7]. Their staging system, currently in use, is aptly named the INRG Staging System (INRGSS), and it relies heavily on imaging (Table 2) [1,4], specifically on the twenty image-defined risk factors (IDRF) of NB (Table 3) [1,2]. The IDRF serves as the basis for decisions regarding therapy, including surgical intervention, and together with clinical data, provides risk stratification and staging for NB [1,4]. It is also important to note that since 2009 COG has used a POG-CCG Intergroup Neuroblastoma Risk Classification System that includes age, INRGSS stage, MYCN status, histologic category, grade of differentiation, ploidy, and 11q status¹ all of which affect tumour aggressiveness, and that in 2021 a revision to include other indicators such as Shimada histology, mitosis karrhyohexis index, extent of primary tumour, segmental chromosomal aberrations and RNA expression signatures was underway [7]. Of all the tumour genetics mentioned above, MYCN requires specific attention because amplification of the MYCN gene is one of the most important poor prognostic factors. MYCN is associated with aggressive NB, and approximately 50% of high-risk patients have MYCN-amplified tumours [8].

Table 1. *International Neuroblastoma Staging System (INSS) Staging System [1].*

Tumour Stage	Description
1	Localized tumour with complete gross excision, with or without microscopic residual disease. Representative ipsilateral lymph nodes are negative for tumour microscopically. Nodes attached to and removed with the primary tumour may be positive.
2A	Localized tumour with incomplete gross excision. Representative ipsilateral nonadherent lymph nodes are negative for tumour microscopically.
2B	Localized tumour with or without complete gross excision, ipsilateral nonadherent lymph nodes are positive for tumour, and enlarged contralateral lymph nodes are negative microscopically.
3	Unresectable unilateral tumour that infiltrates across the midline, with or without regional lymph node involvement, or a midline tumour with bilateral extension via infiltration (unresectable) or lymph node involvement.
4	Any primary tumour with dissemination to distant lymph nodes, bone, bone marrow, liver, skin and/or other organs (except as defined in stage 4S).
4S	Localized primary tumour (as defined in stage 1, 2A, or 2B) with dissemination limited to the skin, liver and/or bone marrow in infants younger than 1 year, marrow involvement of less 10% of total nucleated cells, and MIBG* scan findings negative in the bone marrow.

*Abbreviation MIBG, metaiodobenzylguanidine

Table 2. *International Neuroblastoma Risk Group (INRG) Staging System [1].*

Tumour Stage	Description
L1	Localized tumour not involving vital structures, as defined by the list of IDRFs*, and confined to one body compartment.
L2	Local-regional tumour with presence of one or more IDRFs*.
M	Distant metastatic disease (except as defined in stage MS).
MS	Metastatic disease in children younger than 18 months, with metastasis confined to the skin, liver and/or bone marrow.

*Abbreviation IDRF, Image Defined Risk Factors. Please refer to Table 3 for a list of IDRF.

Table 3. *Description of Image Defined Risk Factors (IDRF) [1].*

Anatomic Region	Description
Multiple body compartments	Ipsilateral tumour extension within two body compartments (i.e., neck and chest, chest and abdomen, or abdomen and pelvis)
Neck	Tumour encasing the carotid artery, the vertebral artery, and/or the internal jugular vein Tumour extending to the skull base Tumour compressing the trachea
Cervicothoracic junction	Tumour encasing the brachial plexus roots Tumour encasing the subclavian vessels, the vertebral artery, and/or the carotid artery Tumour compressing the trachea
Thorax	Tumour encasing the aorta and/or major branches Tumour compressing the trachea and/or principal bronchi Lower mediastinal tumour infiltrating costovertebral junction between T9 and T12 vertebral levels
Thoracoabdominal junction	Tumour encasing aorta and/or vena cava
Abdomen and pelvis	Tumour infiltrating the porta hepatis and/or the hepatoduodenal ligament Tumour encasing branches of the superior mesenteric artery at the mesenteric root Tumour encasing the origin of celiac axis and/or the origin of the superior mesenteric artery Tumour invading one or both renal pedicles Tumour encasing the aorta and/or vena cava Tumour encasing iliac vessels Pelvic tumour crossing the sciatic notch
Intraspinal tumour extension	Intraspinal tumour extension (whatever the location) provided that more than one-third of the spinal canal in the axial plane is invaded, the perimedullary leptomenigeal spaces are not visible, or the spinal cord signal intensity is abnormal
Infiltration of adjacent organs and structures	Pericardium, diaphragm, kidney, liver, duodenopancreatic block, and mesentery

Imaging of the primary tumour in neuroblastoma

The primary tumour is most often located in the adrenal gland (48%), the extra-adrenal retroperitoneum (25%) or the thorax (16–20%) [4]. Both magnetic resonance imaging (MRI) and computed tomography (CT) may be used in the diagnosis of NB [2,4]. It is generally accepted that MRI is superior because of its sensitivity in identifying the local IDRFs such as chest wall invasion, and spinal canal involvement, and in the detection of metastatic bone and bone marrow lesions [2,4]. Indeed, for the reasons stated above, and due to the principle of as low as reasonably achievable (ALARA) radiation exposure in pediatric oncology patients [8], MRI is the imaging of choice for the diagnosis of NB according to the guidelines [1].

On imaging, NB typically appears as a solid, heterogeneous abdominal mass with calcification, that is poorly marginated and may cross the midline (Figure 1) [2,3]. NB has a tendency to encase and displace, rather than invade, anatomical structures [2,4]. On the initial diagnosis, MRI of NB follows the pattern of many solid abdominal malignancies, displaying low or intermediate intensity on T1-weighted sequences and high intensity on T2 [2,4]. There are areas within the tumour of variable contrast-enhancement [2], and NB also often shows restricted diffusion on diffusion weighted imaging [2,4]. MRI can detect areas of calcification and haemorrhage [2]. On CT, NB is characterized by poorly differentiated margins and heterogeneity, with calcification and possible extension across the midline and into adjacent cavities [2]. There may be areas of low density representing cystic necrosis [4].

Neonates and infants require special consideration because NB may have a different disease course in this age group and a unique appearance (Table 2) [2,4]. In neonates, NB originates almost exclusively in the adrenal glands, appears cystic in approximately 50% of cases, although it may also be semi-solid or solid, it is less often calcified, and it carries a better prognosis (Figure 2) [3,6,9]. It is also important to note that cystic NB, when isolated to the adrenal gland, can be confused with an adrenal hematoma, especially as calcifications may be present

in an old hematoma and in NB [3,11]. To further obscure the matter, cystic NB may present with an intra-cystic haemorrhage (Figure 2c) [11]. Serial ultrasounds can differentiate between the two, as hematomas decrease in size more quickly than cystic haemorrhagic NB. In fact, it has been suggested in the literature that neonatal NB is evaluated equally as well by US, partially due to the fact that NB often appears cystic in this age group, and is more easily monitored with serial US examinations [3].

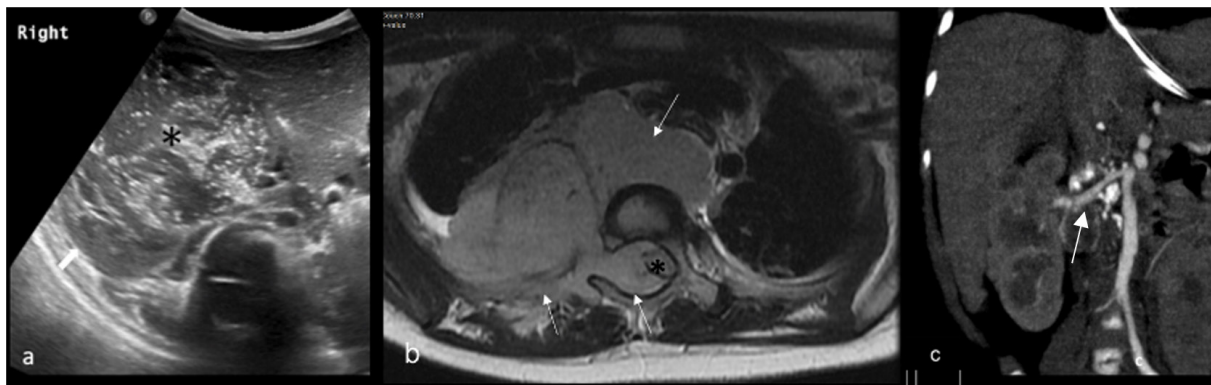


Figure 1. Typical presentations of NB. (a) Ultrasound of an adrenal NB in a 20-month-old boy. Right adrenal mass shown as a solid heterogeneous lesion with calcifications in abdominal US (black asterisk), and the right kidney is caudally displaced (white arrow). (b) A dumbbell lesion in a three-year-old girl with retroperitoneal and paravertebral NB lesions (white arrows) with extension through the neural foramina into the epidural space with severe mass effect on the spinal cord (black asterisk). Intraspinous tumour extension is an IDRF. (c) A one-year-old girl with a right adrenal NB and calcified lymph nodes surrounding the right renal artery (white arrow), shown in a coronal section of an abdominal CT with IV contrast.

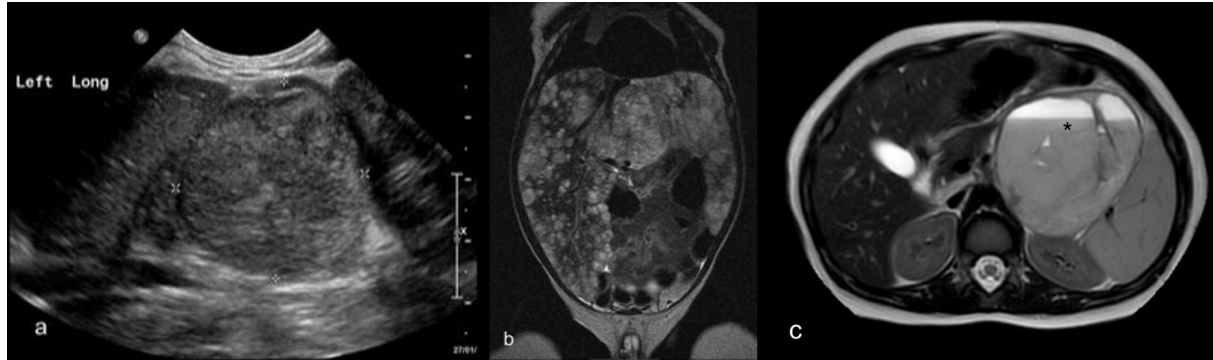


Figure 2. Typical presentation of NB in infants. (a) Ultrasound of an adrenal NB in a newborn, seen also prenatally. The left adrenal mass in the newborn shown as a solid heterogeneous lesion (between the cursors) in an abdominal US. (b) A one-month-old boy with an adrenal mass and multiple liver metastases (stage MS) shown here in a coronal T2W abdominal MRI. Note the enlarged liver with multiple T2W hyperintense lesions. (c) Cystic haemorrhagic NB in a twenty-two-month-old girl. Seen here is an axial T2W MRI image showing a cystic lesion with a fluid-fluid level (black asterisk), located in the upper left abdomen, anterior to the left kidney and the spleen. The lesion was resected and proven to be adrenal NB in pathology.

Additional less common presentations of the primary tumour

Cystic neuroblastoma beyond the neonatal period

Although cystic NB is more typical of neonatal NB, it also occasionally occurs in older pediatric age groups [2]. Cystic NB is defined as having one or more cysts within the tumour, and it may become more complex in appearance over time with solidification into a partially solid or solid lesion [3]. It is identifiable on US, CT or MRI [3]. Bilateral cystic NB is found in less than 10% of NB, and in 20% of familial NB [10]. Metastasis is less likely in cystic NB, and the most common site of metastases in cystic congenital NB is the liver (Figure 3) [6].

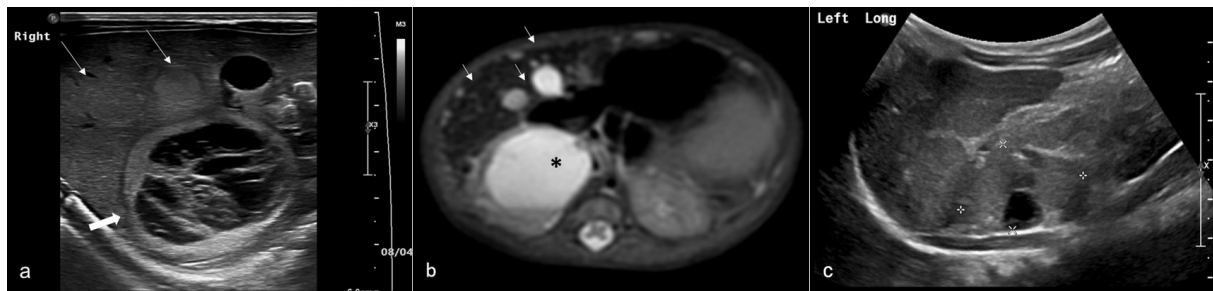


Figure 3. Bilateral adrenal cystic NB with liver metastases in a newborn. (a) Transverse US of the upper right abdomen showing a right adrenal cystic mass with thin septa and a fluid-fluid level (thick arrow), and liver metastasis seen as round isoechoic or slightly hyperechoic lesions in the liver (thin arrows). (b) An axial T2W MRI image showing a haemorrhagic cystic adrenal lesion (black asterisk) and multiple small liver metastases of varying sizes (thin white arrows). (c) Left adrenal mass with cysts within the cursors on a longitudinal US of the upper left abdomen.

Multifocal primary neuroblastoma

Multifocal primary NB is rare, but due to improvements in both our understanding and diagnosis of this disease, the incidence may increase [11,12]. Of note, although most NB is sporadic, multifocal primary NB is most often familial [13]. It is important to distinguish between multifocal primary NB and metastatic NB because multifocal primary NB is associated with more favourable biological features, and aggressive treatment can be avoided [11,12]. Indeed, multifocal NB might regress without any treatment [11]. Imaging findings that favor the diagnosis of multifocal primary NB over metastatic NB, are tumours on opposite sides of the body without distant lymph node, and bone or bone marrow metastases (Figure 4) [12]. Interestingly, it is thought that bilateral adrenal NB and stage 4S NB (similar to INRGSS stage MS), might actually be multifocal primary NB [11].

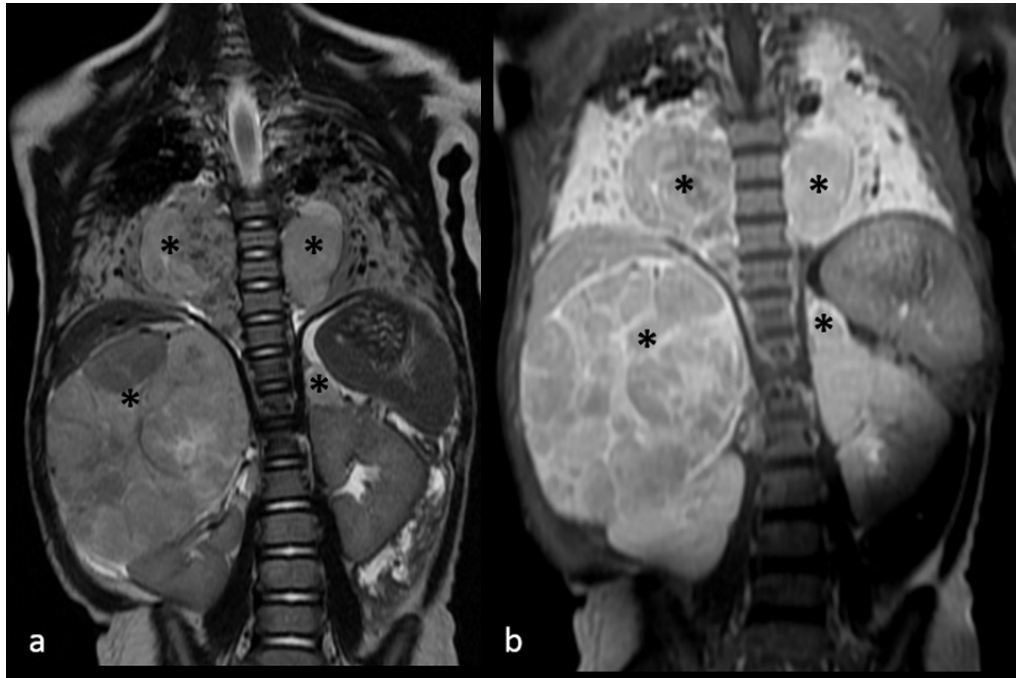


Figure 4. Multifocal NB at presentation in a four-year-old girl. (a) Coronal T2W MRI and (b) coronal T1W MRI with contrast are images of the chest and abdomen showing four discrete locations of NB (black asterisks); paravertebral lesions in the chest, one on each side of the spine, and bilateral adrenal lesions, larger on the right.

Renal neuroblastoma

Renal invasion of NB is fairly common due to the close proximity of the kidney to the adrenal gland, and indeed infiltration of the kidney is an IDRF. Renal NB (Figure 5), however, is extremely rare, and on imaging alone, it can easily be confused with Wilms tumour [14]. Key differences that may help distinguish between the two are calcifications, best seen on CT and typical of NB, and cystic components that are more likely in Wilms tumour [2]. NB is more likely to be a poorly margined mass that may extend into the chest while Wilms is usually well

circumscribed [2]. NB is generally more likely to encase and displace anatomical structures including vessels, in contrast to Wilms tumour that often invades vasculature, especially the renal vein and IVC [2]. The most common metastatic sites of the tumours also differ; NB tends to metastasize to the bone and bone marrow while Wilms tumour most often metastasizes to the lung [2]. However, metastatic sites do overlap, including the lung, and liver metastases are fairly common to both tumours [2]. Another important difference is that MIBG is usually sensitive and specific for NB, while Wilms tumour is MIBG negative [2].

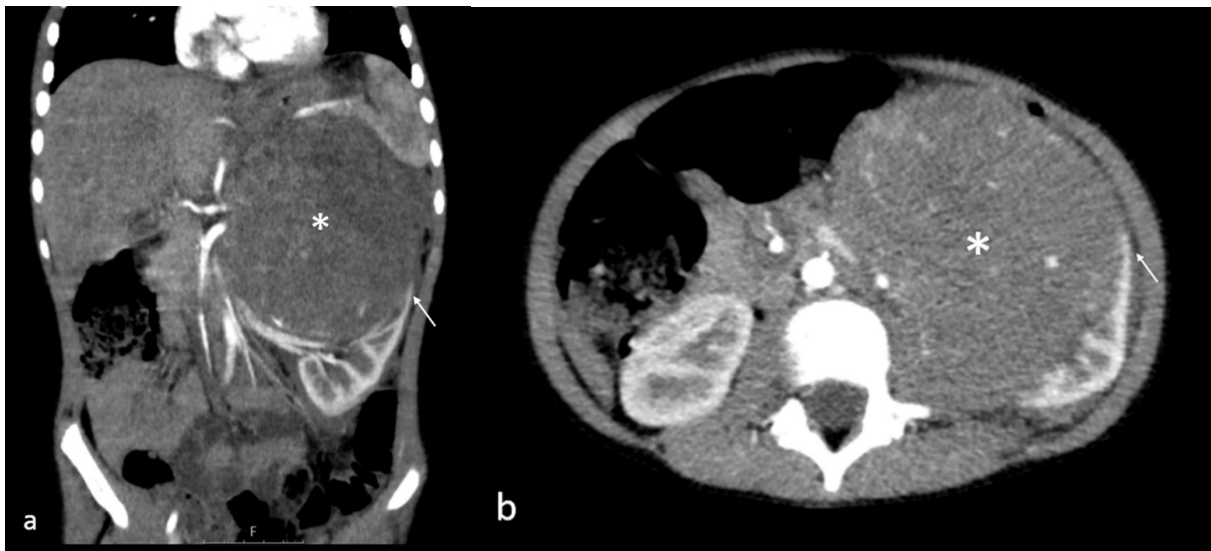


Figure 5. A five-year-old boy with a large left renal mass, treated with nephrectomy, with pathology proven primary renal NB. CT of the abdomen with contrast shows the kidney to be the origin of the large mass (white asterisk); cortical beak sign of the kidney can also be seen (thin white arrows), further affirming that the kidney is the origin of the mass in both (a) coronal and (b) axial images. Please note that invasion of the tumor into the renal pedicle is an IDRF is clearly seen in both the coronal and axial images.

Pancreatic neuroblastoma

This unusual presentation of NB may arise from neural-crest derived precursors to the enteric nervous system that assists in the formation of pancreatic ganglia or neural crest signals that regulate the proliferation of pancreatic beta cells [15]. As of the year 2020, fewer than ten cases of pancreatic NB were identified in the literature (Figure 6) [15]. Despite its rarity, radiologists must remain alert to pancreatic NB, because NB is of the most common childhood cancers [16]. Imaging alone may not distinguish between pancreatic NB and other findings such as cystic teratoma, requiring further diagnostic workup that should include pathology.

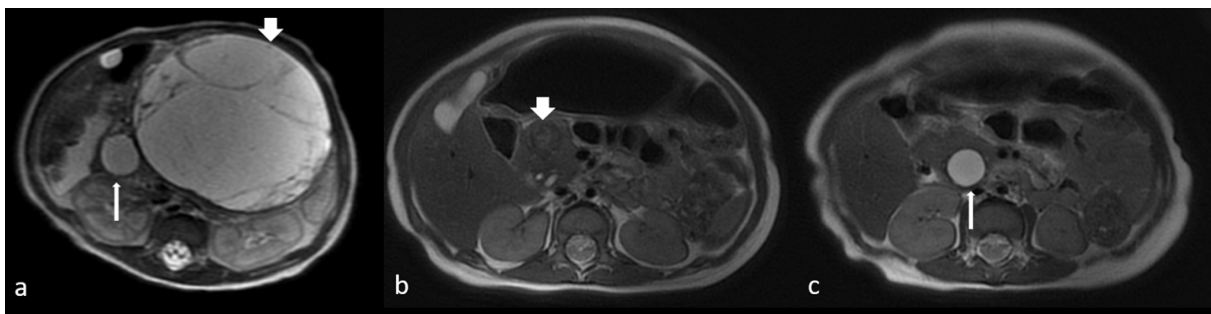


Figure 6. A 17-day old girl, was referred to US due to abdominal distention. She was diagnosed with NB, proven by pathology, and followed by the MRI studies presented and did not undergo treatment or intervention. (a) An axial T2W MRI image showed two cystic lesions in the central mid abdomen, the larger a multi septate mass (arrowhead) and the smaller a simple cyst (arrow), diagnosed as NB. Only in follow up imaging, at the age of 7 months, was it clear that the lesions were located in the pancreas. Axial T2W MRI images showed two distinct pancreatic lesions in the uncinated process (arrowhead in b) and within the pancreatic head (arrow in c). The larger mass shrank and coarse calcifications appeared. No other mass was seen, and the adrenals appeared normal (not shown). Urine dopamine and neuron-specific enolase B (NSE-B) levels remained elevated until she was 12 months old.

Olfactory neuroblastoma

Olfactory NB (ONB) or esthesioneuroblastoma is believed to arise from basal neural cells of the olfactory mucosa in the superior nasal cavity [17], in close proximity to the cribriform plate (Figure 7) [17,18]. It usually appears in the fifth and sixth decades of life, less commonly in children [17]. ONB has its own staging system, Kadish staging, but it lacks standardized treatment protocols. The natural history of the disease varies and it is often in a challenging location for surgery [18]. Radiological evaluation for staging often includes a combination of MRI, CT and PET/CT. ONB typically appears as a soft tissue mass with its focal point at the superior olfactory recess, and it frequently demonstrates localized invasion, especially into the ethmoid sinuses. Extension through the cribriform plate may give the mass a “dumbbell” appearance, and cervical lymph node metastasis is present in approximately 20-30% of the patients [17].



Figure 7. A 16-year-old boy presented with vomiting and behaviour change proceeding several months of headache, with laboratory results significant for hyponatremia due to SIADH. He was later diagnosed with NB. (a) Axial and (b) coronal T2W MRI showing an intermediate signal intensity mass filling the left superior nasal cavity and middle meatus with extension into the maxillary sinus. (c) Sagittal T1W MRI showing contrast enhancement of the same mass.

Other documented locations of neuroblastoma

Other locations of NB include bladder NB (8 cases reported by 2020) [19], sacrococcygeal NB (8 cases reported by 2020 [20], orbital NB [21], and NB within a teratoma, observed in ovarian teratomas [22], and an orbital teratoma [23].

Imaging of metastases in neuroblastoma

Approximately fifty percent of NB presentations are complicated by metastases [2], which are most frequently found in the bone and bone marrow [4], typically in the long bones of the extremities, in the skull and in the bony orbit [24]. Skull bone metastasis in NB is also known as Hutchison's syndrome, and a limping gait with irritability is also a feature attributed to this syndrome [27]. NB is of the more common childhood cancers [2], and considering the high percentage of bone metastasis, aggressive bone lesions should raise the question of NB (Figure 8). It is also important to note that in cystic congenital NB, metastasis is less likely, and if it occurs, it is most commonly in the liver [6]. Congenital NB is also associated with skin and cutaneous lesions, appearing as a 'blueberry muffin syndrome' that has a broad differential diagnosis including congenital infections and other underlying malignancies [28].

Functional imaging is crucial for assessing NB metastases, and the most commonly used are metaiodobenzylguanidine (MIBG) scintigraphy, fluorodeoxyglucose combined with Positron Emission Tomography (FDG-PET), and 8F-3,4-dihydroxyphenylalanine (F-DOPA) PET/CT [24,25]. MIBG is sensitive and specific in the detection of NB [1], but a small percentage of NB tumours do not uptake MIBG [4]. In MIBG negative tumours as well as stage 1 and 2 tumours, FDG-PET is considered superior [2,4]. Nonetheless, MIBG has a higher tumour to non-tumour uptake ratio than FDG-PET, minimizing the number of false negatives [4]. F-DOPA PET/CT has been shown to be more sensitive than MIBG in some studies and may also be recommended in MIBG negative tumours [25]. The current guidelines state that MIBG is the functional imaging of choice for NB [1].

Other scans can be considered when the presentation requires further analysis, as will be discussed in the following sections when applicable [1].

MRI is the cornerstone imaging modality for assessing both primary tumours and metastases; it is especially sensitive in the detection of metastatic bone and bone marrow lesions and spinal canal involvement [2,4].

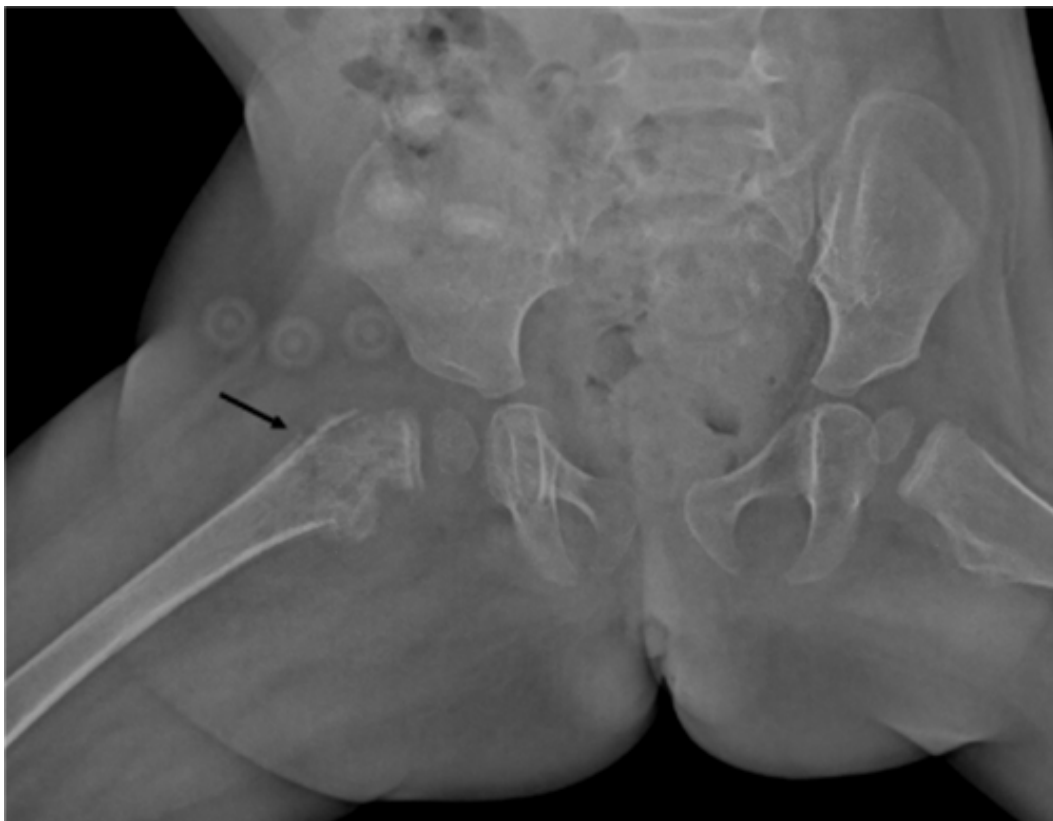


Figure 8. Femur fracture on the right in a 2-year-old girl, which was found to be metastatic NB.

Other less common metastatic presentation of neuroblastoma

Orbital metastases without a primary lesion

NB metastases to the skull, including orbital metastases (Figure 9), might be observed often because the skull represents a high proportion of the skeleton in young people [26]. A common clinical presentation of orbital invasion, for NB and other cancers, is ecchymotic orbital proptosis, but other symptoms include vision loss, edema, and restricted eye movement [27]. The radiological presentation of orbital NB usually includes thickened bones, in the sphenoid or the bones of the orbit itself, as well as periosteal reactions and lytic lesions. On MRI, orbital NB is characterized by low signal intensity on T1 and high signal intensity on T2-weighted images [27].

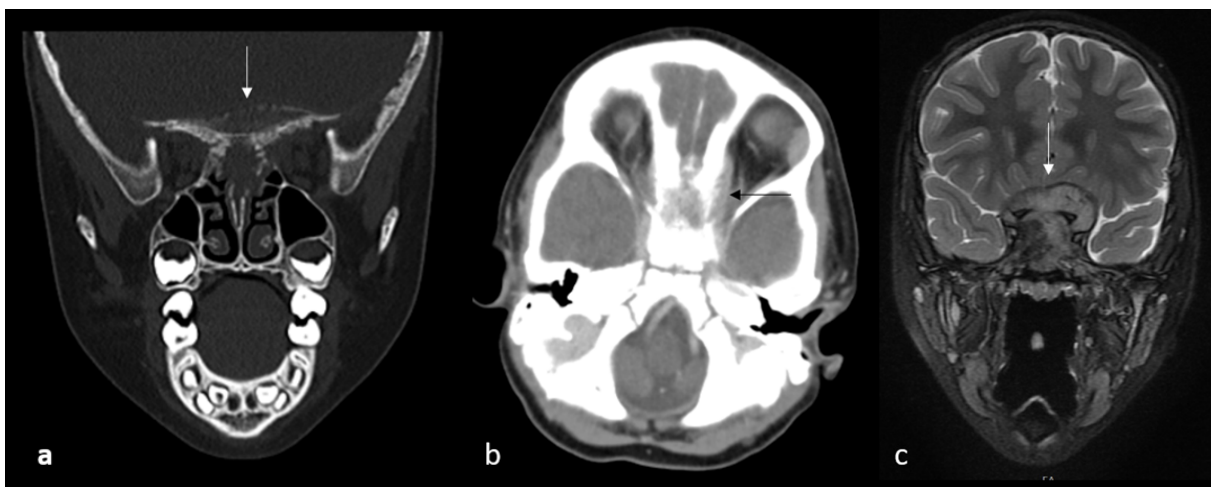


Figure 9. A CT was performed on a girl aged two years and seven months who presented with a one-month history of torticollis, neck pain and intermittent strabismus. (a) Coronal CT in bone filter revealed a bony sphenoid lesion (thin arrow). (b) Axial image shows the soft tissue window of the same sphenoid bone lesion (thin arrow). (c) Coronal T2W MRI image shows the sphenoidal lesion surrounding both pre-chiasmatic optic nerves (thin arrow).

Mandibular metastasis

Mandibular metastases (Figure 10) warrant a broad differential diagnosis that may include lymphoma, soft tissue sarcoma, osteosarcoma, primitive neuroectodermal tumour (PNET), a central malignancy of the odontogenic origin, or a metastatic tumour [28]. In such cases histopathologic evaluation of tumour tissue or the analysis of bone marrow aspirate for the presence of tumour cells is crucial for diagnosis, as well as standard laboratory tests for NB [28].

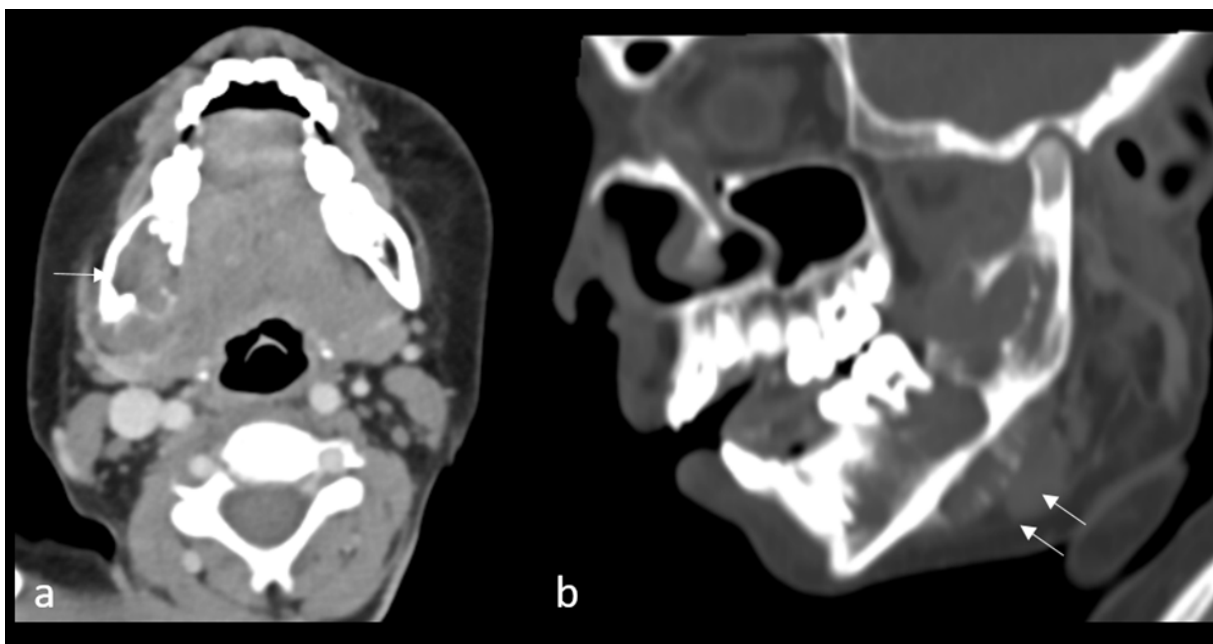


Figure 10. *Mandibular metastasis in an eight-year-old both with proven retroperitoneal NB. Axial (a) and sagittal (b) CT images of the mandible. Note the lytic lesion with an aggressive periosteal reaction (arrows).*

Lung metastasis

Lung and pleural metastases on presentation of NB are extremely rare, and are only seen in children presenting with other distant metastases, considered stage M [6, 29-31]. Lung metastases are present at diagnosis in approximately 3.6% of stage 4 NB [1,29], and are independently associated with a worse prognosis (Figure 11) [29,30]. Although CT is not a routine screening tool in the diagnosis of NB, it is the most sensitive imaging tool for the assessment of lung metastasis, and therefore should be used when lung nodules are suspected [1]. On imaging, NB lung metastases have non-specific patterns [1], but the most common finding on CT is multiple nodules of varying sizes and distributions, noncalcified, some smooth and some spiculated [31]. Calcified lung nodules have also been observed [6]. The non-specific nature and rarity of NB lung metastases, as well as the current imaging protocols, make it a challenge to find these metastases [6].

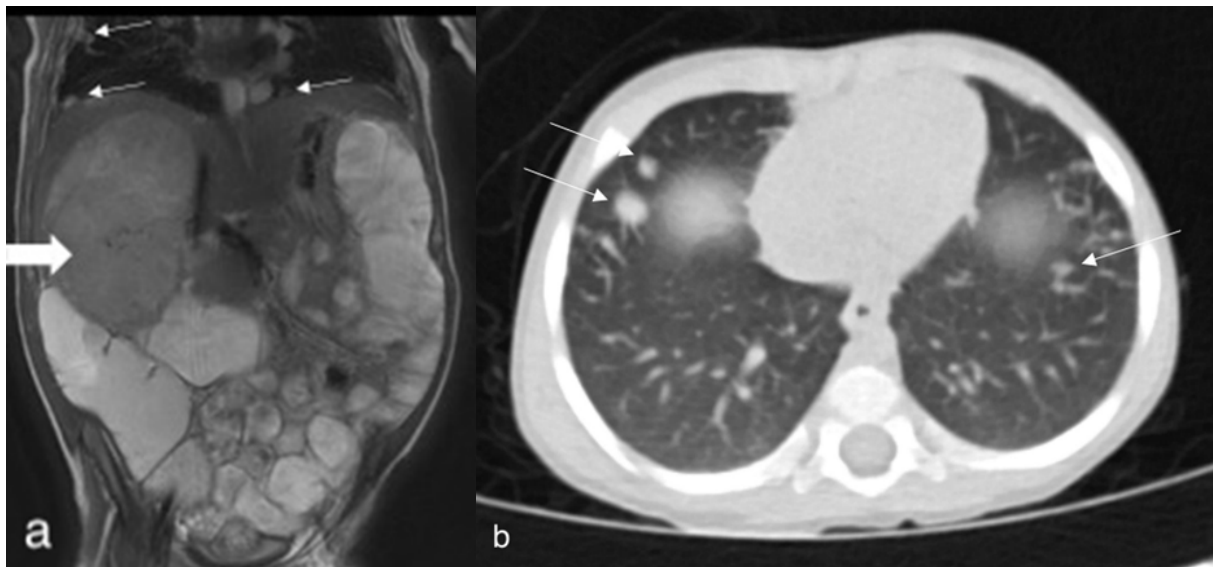


Figure 11. A fifteen-month-old boy with right adrenal NB. Initially, an MRI of the primary lesion in the right adrenal was performed. (a) A coronal T2W MRI of the primary tumour in the right adrenal (thick arrow) revealed lung lesions suspected to be metastases at presentation (thin arrows), necessitating a chest CT. (b) An axial chest CT without contrast in the lung window that showed multiple bilateral nodules, some with coarse calcifications, a characteristic of lung metastases (thin arrows).

Other documented metastatic sites

Other atypical metastases at presentation are bone marrow metastases with no primary tumour,²⁴ central nervous system metastases [26,32], pancreatic metastasis and ovarian metastasis [33].

Opsoclonus-myoclonus syndrome in neuroblastoma

Opsoclonus-myoclonus ataxia syndrome (OMAS) is a rare inflammatory disorder, often with a paraneoplastic etiology, specifically associated with NB [34]. Only about 2-3% of children with NB have OMAS, but it is suspected that approximately 50% of pediatric OMAS cases are precipitated by an underlying NB [34]. OMAS is associated with low-risk NB and favorable oncological outcomes, but the neurological sequelae, such as relapsing OMAS, is more challenging to treat [35]. Tumour resection is important to the treatment of OMAS, even if the low-risk nature of the tumour would otherwise allow for a 'wait and see' approach [35]. OMAS may be associated with a miniscule, difficult to detect, NB tumour (Figure 12) [34], underscoring the importance of searching well for NB in children who present with OMAS. In addition, NB is known to appear as long as six months after the onset of OMAS; therefore, long-term monitoring is required, including follow-up urine, serum, and MRI studies [35]. Interestingly, research that retrospectively analyzed 38 children with OMAS, suggested that ⁶⁸Ga-labelled DOTANOC PET/CT might be more sensitive than MIBG for the detection of very small NB tumours [34]. Also, a larger study showed no MIBG uptake in non-primary NB tumour sites in children and adults with OMAS [36], suggesting that functional imaging alternatives should be considered.

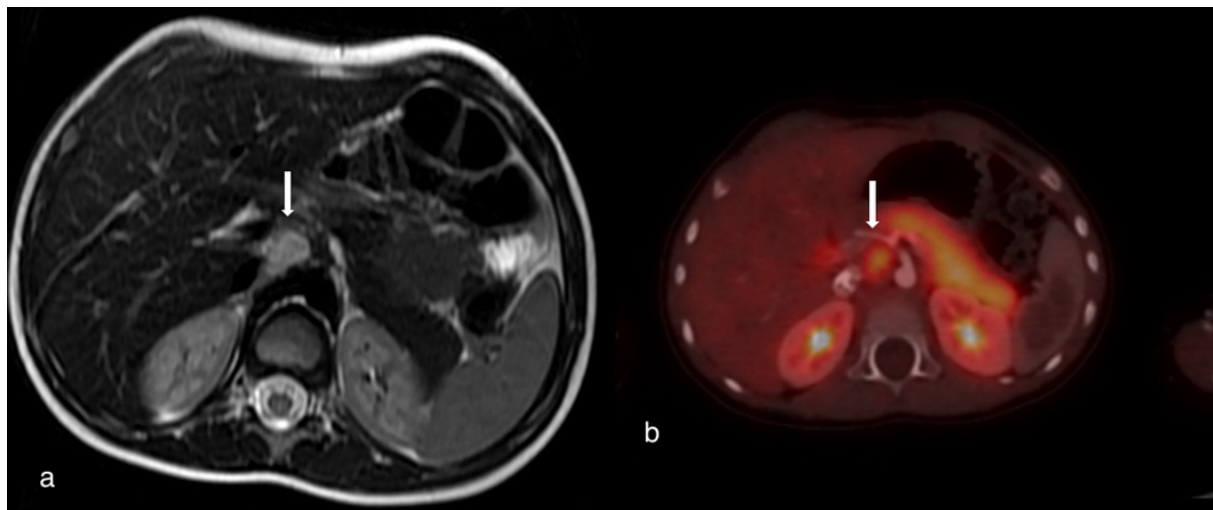


Figure 12. A five-month-old girl who presented with opsoclonus myoclonus ataxia syndrome. (a) axial T2W showed a small solid retroperitoneal lesion adjacent to the celiac trunk on the right (white arrow) with high attenuation. (b) an 18F-DOPA PET/CT shows the same solid lesion (white arrows) in a fused image.

Conclusion

The diagnosis and staging of NB are heavily reliant on imaging, and though this pediatric tumour is common, the broad range of possible imaging presentations continues to be a challenge for radiologists.

References

1. Brisse HJ, McCarville MB, Granata C, Krug KB, Wootton-Gorges SL, Kanegawa K, et al. Guidelines for imaging and staging of neuroblastic tumors: Consensus report from the International Neuroblastoma Risk Group Project. *Radiology* 2011;261:243-57. doi:10.1148/radiol.11101352.
2. Dumba M, Jawad N, McHugh K. Neuroblastoma and nephroblastoma: A radiological review. *Cancer Imaging* 2015;15(5):1-14. doi:10.1186/s40644-015-0040-6.
3. Hwang SM, Yoo SY, Kim JH, Jeon TY. Congenital adrenal neuroblastoma with and without cystic change: Differentiating features with an emphasis on the value of ultrasound. *Am J Roentgenol* 20;207:1105-11. doi:10.2214/AJR.16.16452.
4. Chen AM, Trout AT, Towbin AJ. A review of neuroblastoma image-defined risk factors on magnetic resonance imaging. *Pediatr Radiol* 2018;48:1337-47. doi:10.1007/s00247-018-4117-9.
5. Tsubota S, Kadomatsu K. Origin and initiation mechanisms of neuroblastoma. *Cell Tissue Res* 2018;372:211-21. doi:10.1007/s00441-018-2796-z.
6. Menager N, Quarello E, Capelle M, Lacroze V, Coze C, De Lagausie P, et al. Prenatal diagnosis of atypical adrenal neuroblastoma with pulmonary metastases is possible: Impact on the assessment of prenatal prognosis. *Diagn Interv Imaging* 2012;93:632-4. doi:10.1016/j.diii.2012.03.005.
7. Liang WH, Federico SM, London WB, Naranjo A, Irwin MS, Volchenboum SL, et al. Tailoring Therapy for Children With Neuroblastoma on the Basis of Risk Group Classification: Past, Present, and Future. *JCO Clin Cancer Inform* 2020;4:895-905. doi:10.1200/cci.20.00074.

8. Voss SD, Reaman GH, Kaste SC, Slovis TL. The ALARA concept in pediatric oncology. *Pediatr Radiol* 2009;39:1142-6. doi:10.1007/s00247-009-1404-5.
9. Richards ML, Gundersen AE, Williams MS. Cystic neuroblastoma of infancy. *J Pediatr Surg* 1995;30:1354-7. doi:10.1016/0022-3468(95)90504-9.
10. Alshahrani MA, Bin Saeedan M, Alkhunaizan T, Aljohani IM, Azzumeea FM.. Bilateral adrenal abnormalities: imaging review of different entities. *Abdom Radiol (NY)* 2019 44:154-79. doi: 10.1007/s00261-018-1670-5.
11. Coorens THH, Farndon SJ, Mitchell TJ, Jain N, Lee S, Hubank M, et al. Lineage-independent tumors in bilateral neuroblastoma. *N Engl J Med* 2020;383:1860-5. doi:10.1056/NEJMoa2000962.
12. Hiyama E, Yokoyama T, Hiyama K, Yamaoka H, Matsuura Y, Nishimura Si, et al. Multifocal Neuroblastoma. *Cancer* 2000;88:1955-63.
13. Skiker I, Dafiri R. Synchronous primary neuroblastoma. *Eurorad* 2008;CASE 6594:1-7. doi:10.1594/EURORAD/CASE.6594.
14. Fan R. Primary Renal Neuroblastoma — A Clinical Pathologic Study of 8 Cases. *Am J Surg Pathol* 2012;36:94-100. doi: 10.1097/PAS.0b013e318233083b.
15. Morrison ZD, Sun Y, Manalang M, Dominguez K. Primary pancreatic neuroblastoma in an infant. *J Pediatr Hematol Oncol* 2020;42:E541-3. doi:10.1097/MPH.0000000000001629.
16. Galgano S, Royal S. Primary pancreatic neuroblastoma presenting with opsoclonus-myooclonus syndrome. *Radiol Case Reports* 2016;11:36-40. doi:10.1016/j.radcr.2015.09.003.
17. Caldwell NJ, Sato TS. Ectopic primary olfactory neuroblastoma of the nasopharynx: A case report and review of the literature. *Radiol Case Rep* 2019;14:997-1002. doi:10.1016/j.radcr.2019.05.031.

18. Pacino GA, Cocuzza S, Maniaci A, Da Mosto MC, Pavone P, Spinato G. Correction to: advanced olfactory neuroblastoma in a teenager: a clinical case and short review of literature. *Childs Nerv Syst* 2020;36:485-9. doi:10.1007/s00381-020-04566-x.
19. Cai JB, Wang JH, He M, Wang FL, Xiong JN, Mao JQ, et al. Unusual presentation of bladder neuroblastoma in a child: A case report. *World J Clin Cases* 2020;8:194-9. doi:10.12998/wjcc.v8.i1.194.
20. Dey S, Ghosh A, Sil K, Saha Basu K, Chatterjee U. Congenital Sacrococcygeal Neuroblastoma: A Report of Two Cases with Summary of Prior Published Cases. *Fetal Pediatr Pathol* 2020;41:643-50. doi:10.1080/15513815.2020.1857486.
21. Inazawa N, Hatakeyama N, Hori T, Yamamoto M, Igarashi K, Tadashi H, et al. Primary orbital neuroblastoma in a 1-month-old boy. *Pediatr Int* 2014;56:122-5. doi:10.1111/ped.12239.
22. Niwa Y, Yamamuro O, Kato N, Tsuzuki T. Two cases of primary ovarian neuroblastoma arising from mature cystic teratomas. *Gynecol Oncol Case Rep* 2013;5:58-60. doi:10.1016/j.gynor.2013.04.006.
23. Chalam KV, Gupta SK, Vinjamaram S, Shah VA. Clinicopathologic reports, case reports, and small case series: congenital anomalous retinal artery associated with a leaking macroaneurysm. *Arch Ophthalmol* 2003;121:409-10. doi: 10.1001/archophth.121.3.409.
24. Botía González CM, Sirvent Cerdá SI, Azorín D. Bone metastasis of primitive occult neuroblastoma. *Eurorad* 2018;Case 15699. doi:10.1594/EURORAD/CASE.15699.
25. Piccardo A, Morana G, Puntoni M, Campora S, Sorrentino S, Zucchetta P, et al. Diagnosis, Treatment Response, and Prognosis: The Role of 18 F-DOPA PET/CT in Children Affected by Neuroblastoma in Comparison with 123 I-mIBG Scan: The First Prospective Study. *J Nucl Med* 2020;61:367-74. doi:10.2967/jnumed.119.232553.

26. Kushner BH. Neuroblastoma: A Disease Requiring a Multitude of Imaging Studies. *J Nucl Med* 2004;45:1172-88.
27. Yang WJ, Zhou YY, Zhao F, Mei ZM, Li S, Xiang Y. Orbital neuroblastoma metastasis: A case report and literature review. *Medicine (Baltimore)* 2019;98(36):e17038. doi: 10.1097/MD.00000000000017038.
28. Otmani N, Khattab M. Metastatic neuroblastoma to the mandible in a 3-year-old boy: a case report. *Med Oral Patol Oral Cir Bucal* 2007;12(3):E201-4.
29. DuBois SG, London WB, Zhang Y, Matthay KK, Monclair T, Ambros PF, et al. Lung metastases in neuroblastoma at initial diagnosis: A report from the International Neuroblastoma Risk Group (INRG) project. *Pediatr Blood Cancer* 2008;51:589-92. doi:10.1002/pbc.21684.
30. He B, Mao J, Huang L. Clinical Characteristics and Survival Outcomes in Neuroblastoma With Bone Metastasis Based on SEER Database Analysis. *Front Oncol* 2021;11:677023. doi:10.3389/fonc.2021.677023.
31. Kammen BF, Matthay KK, Pacharn P, Gerbing R, Brasch RC, Gooding CA. Pulmonary metastases at diagnosis of neuroblastoma in pediatric patients: CT findings and prognosis. *AJR Am J Roentgenol* 2001;176:755-9. doi:10.2214/ajr.176.3.1760755.
32. Matthay KK, Brisse H, Couanet D, Couturier J, Bénard J, Mosseri V, et al. Central nervous system metastases in neuroblastoma: Radiologic, clinical, and biologic features in 23 patients. *Cancer* 2003;98:155-65. doi:10.1002/cncr.11448.
33. Sakai S, Nomura K, Abe T, Hayashi K, Tsutsuno T, Mizushima H, et al. Neuroblastoma with ovarian and pancreatic metastasis. *J Pediatr Surg Case Reports* 2021;73:e101996. doi:10.1016/j.epsc.2021.101996.

34. Kumar R, Vankadari K, Mittal BR, Bansal D, Trehan A, Sahu JK, et al. Diagnostic values of ⁶⁸Ga-labelled DOTANOC PET/CT imaging in pediatric patients presenting with paraneoplastic opsoclonus myoclonus ataxia syndrome. *Eur Radiol* 2021;31:4587-94. doi:10.1007/s00330-020-07587-x.
35. Bhatia P, Heim J, Cornejo P, Kane L, Santiago J, Kruer MC. Opsoclonus-myoclonus-ataxia syndrome in children. *J Neurol* 2022;269:750-7. doi:10.1007/s00415-021-10536-3.
36. Anand S, Agarwala S, Jain V, Bakhshi S, Dhua A, Gulati S, et al. Neuroblastoma with Opsoclonus-Myoclonus-Ataxia Syndrome: Role of Chemotherapy in the Management: Experience from a Tertiary Care Center in a Resource-limited Setting. *J Pediatr Hematol Oncol* 2021;43:E924-E929. doi:10.1097/MPH.0000000000002131.

ASEAN Movement in Radiology

Tuberculosis: Important lessons from AOCR 2023, Bangkok, Thailand

Mini Pakkal, M.D.⁽¹⁾

Bushra Johari, M.D.⁽²⁾

Jin Mo Goo, M.D., Ph.D.⁽³⁾

Ki Yeol Lee, M.D., Ph.D.⁽⁴⁾

Kushaljit Singh Sodhi, M.D.⁽⁵⁾

Murali Krishna, M.D.⁽⁶⁾

Wiwatana Tanomkiat, M.D.⁽⁷⁾

From ⁽¹⁾ University of Toronto, Department of Medical Imaging, Toronto General Hospital, Toronto, Canada,

⁽²⁾ Department of Radiology, Faculty of Medicine, Universiti Teknologi MARA, Sungai Buloh, Malaysia,

⁽³⁾ Department of Radiology, Seoul National University Hospital, Seoul, Korea,

⁽⁴⁾ Department of Radiology, Korea University Ansan Hospital, Asan, Korea,

⁽⁵⁾ Department of Radiodiagnosis and Imaging, Postgraduate Institute of Medical Education and Research, Chandigarh, India,

⁽⁶⁾ Department of Radiology and Imaging Sciences, Fortis Hospitals, Vadapalani, Chennai, India,

⁽⁷⁾ Department of Radiology, Faculty of Medicine, Prince of Songkla University, Hat-Yai, Songkla, Thailand.

Address correspondence to W.T.(email: twiwadha@hotmail.com)

Received 12 August 2023 ; accepted 12 August 2023
doi:10.46475/aseanjr.v24i2.871

Abstract

The Asian Symposia at the AOCR 2023 discussed the situation and role of radiology in tuberculosis. The scientific committee of the Asian Oceanian Congress of Radiology (AOCR) established the Asian Symposia in order to discuss important and relevant health topics with participating Asian radiological societies. At the AOCR 2023 Asian Symposia I: Situation and Imaging Innovation in Tuberculosis, different views, initiatives, and ideas were presented by representatives from various societies.

Keywords: Asian Symposia, Deep learning, Digital tomosynthesis, Epidemiology, Imaging, Low-dose computed tomography, Lung screening, MRI, National TB Eradication Program (NTEP), South-East Asia, Tracheobronchial stenosis, The International Union Against Tuberculosis and Lung Disease, Tuberculosis, Ultrasound.

Main messages:

- Tuberculosis (TB) is the world's top infectious killer and 50% of TB patients are seen in Asia.
- Understanding TB as a great mimicker, radiologists play a key role in early detection of the disease.
- Tracheobronchial stenosis is an important complication of active TB necessitating a multidisciplinary approach to treatment. It is diagnosed primarily by CT as chest radiographs may be normal in 20% of the cases.
- It is important to differentiate latent from active TB from a treatment perspective. Radiologists play an active role in differentiating between these two entities.
- A chest radiograph is the first test for diagnosing tuberculosis in patients with respiratory symptoms, but its accuracy is about 49%. Disadvantages of CT are radiation exposure and expensive examination. New imaging modalities, such as mediastinal ultrasound (US), ultralow dose CT, dual-energy subtraction digital radiography, digital tomosynthesis, MRI and tuberculosis diagnosis using deep learning, are also being used.
- Malaysia is committed to the vision of the National Strategic Plan for TB Control, for Malaysia to be a TB-free country by 2035.
- The latest National TB Eradication Program (NTEP) from India is marching towards TB eradication by 2025 by translating high level political commitment to action and working with international agencies and projects.
- The Korea Disease Control and Prevention Agency implemented the 'Measures to Strengthen TB Prevention Management,' in 2019. Korea's goal is to eradicate TB by 2030.

Introduction

The Asian Symposia was established by the Asian Oceanian Congress of Radiology (AOCR) scientific committee with the aim of discussing current burning issues in important and relevant health topics pertaining to Asian countries. The symposia were held on the second day of AOCR 2023 and participation was by invitation only. Tuberculosis (TB) and Post-Covid Lung were two important topics that took the spotlight in the AOCR 2023 Asian Symposia. This article elaborates on the various national perspectives on tuberculosis.

The following societies delivered a presentation and subsequently submitted a written report summarizing the point of view of their respective country or region: the Asian Society of Thoracic Radiology (ASTR), the Korean Society of Thoracic Radiology (KSTR), the College of Radiology, Academy of Medicine of Malaysia (COR, AMM), the Asian Oceanic Society of Paediatric Radiology (AOSPR), and the Indian Radiological & Imaging Association (IRIA).

The situation in Malaysia

Bushra Johari, representing the COR, AMM, stated that the TB incidence in Malaysia in 2020 reduced to 72.4 per 100,000 people, compared to 79.0 per 100,000 people in 2015. However, TB mortality increased from 7.1 per 100,000 people in 2020 compared to 5.5 per 100,000 people in 2015. Nevertheless, Malaysia is committed to the vision of the National Strategic Plan for TB Control, for Malaysia to be a TB-free country by 2035 [1]. Malaysia acknowledges that many challenges remain in materializing this vision. The country still deals with delays in diagnosing smear-negative pulmonary TB, challenging extra-pulmonary TB cases, and treatment default and non-adherence. The programmatic management of latent TB infection (LTBI), also known as TB preventive treatment, was recently launched and will take time to mature and produce results [1].

The management of active TB differs from that of latent TB, and radiologists play an important role in delineating between active forms of TB and an indolent infection. The typical presentation of active pulmonary TB in Malaysia is comparable to the existing literature, including parenchymal disease, lymphadenopathy, pleural effusion, miliary disease and airway involvement [2].

In recent years, Malaysia has seen cases of tracheobronchial stenosis as a presentation or complication of active pulmonary TB, especially in the young adult population. The infection of the tracheobronchial tree exists in 10–40% of patients with pulmonary TB, with the complication of tracheobronchial stenosis occurring in more than 60% of the patients within six months of disease progression [3]. Tracheobronchial stenosis in TB warrants early detection and intervention. Regular Multidisciplinary Team (MDT) discussions between respiratory physicians, thoracic radiologists, interventional pulmonologists and thoracic surgeons focusing on the diagnosis of endobronchial tuberculosis and the best treatment option is essential. There is also an ongoing effort to educate primary care physicians, general practitioners, general physicians and radiologists to recognize this condition, as they remain the front liners dealing with patients at the initial disease presentation. Chest radiograph (CXR) remains the first imaging modality in patients suspected of airway tuberculosis. It can appear normal in approximately 20% of cases [4] with total lung collapse or lobar collapse manifesting on CXR when the obstruction to the airway lumen is significant. CT scans can exquisitely identify the presence of stenosis, with a full assessment of the stenotic site and features of complications from the stenosis (Figure 1). Other less common findings of active pulmonary TB seen in Malaysia include the and non-confluent and confluent clusters of micronodules (Figure 2) and the nodular reverse halo sign.



Figure 1. Coronal reconstruction of Contrast-Enhanced CT Thorax in mediastinal window demonstrates airway involvement in active pulmonary tuberculosis. There is significant narrowing of the left main bronchus compared to the right, with near total occlusion distally (arrow). The airway wall is thickened and irregular. There are multiple enlarged hypodense mediastinal and hilar lymph nodes which show calcification. Consolidation is also seen in the right and left lung.

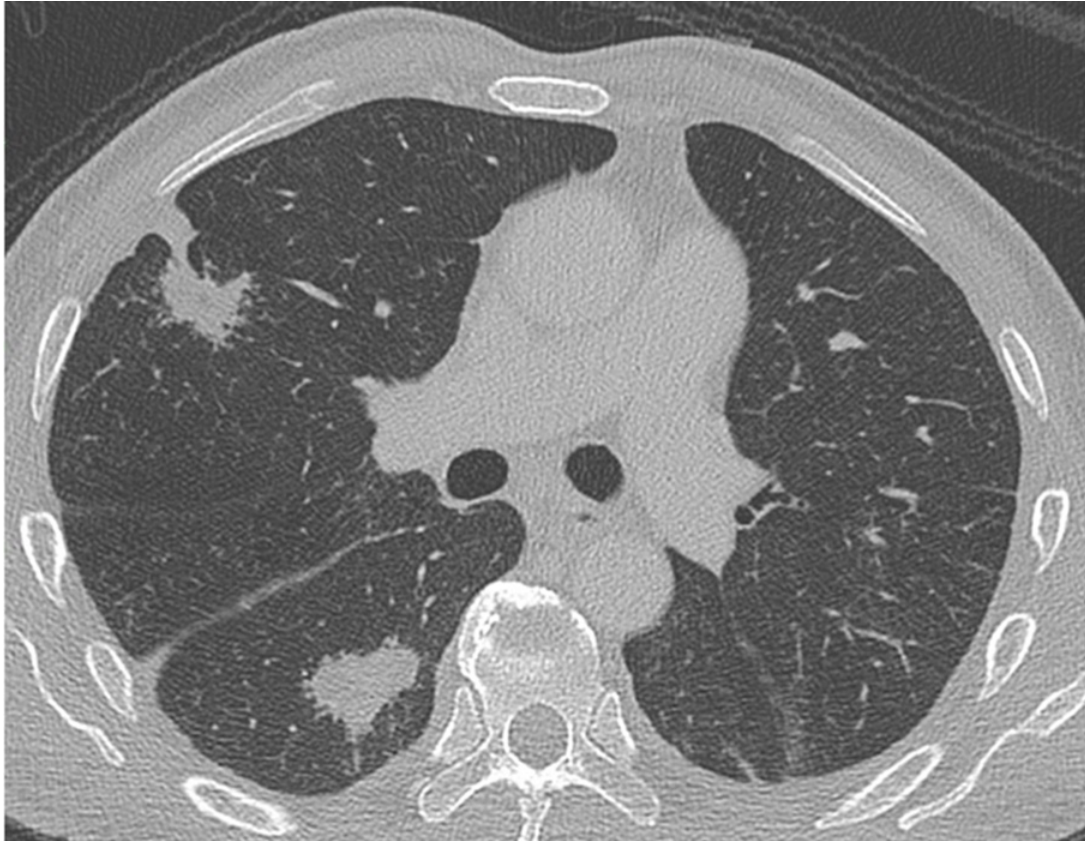


Figure 2. Axial CT Thorax in the lung window of a patient with active tuberculosis showing irregular lung lesions in the right upper and lower lobes. These macronodules were formed from the confluence of numerous tiny nodules, in keeping with the 'galaxy sign'.

Conclusion:

Malaysia recognizes that TB is still endemic and continues to be a significant public health concern. Efforts to reduce TB-related mortality and morbidity are still ongoing. Recognition of the spectrum of imaging findings of active TB is of utmost importance for us to achieve our goals and for a timely institution of treatment. Successful management of complicated active TB needs MDT discussion to ensure a good patient outcome.

General situation in India

Murali Krishna presented on behalf of the IRIA that TB is the top infectious disease killer in both India and the world alike. More than 1.9 million were affected by TB in the year 2021 [5]. The government of India had launched multiple programs to control the disease. The National TB Eradication Program (NTEP) with a goal to achieve rapid decline in the burden of TB, mortality and morbidity, while working towards the elimination of TB in India by 2025 [6].

Four strategic areas include detect, treat, prevent, and build pillars for universal coverage and social protection. The program provides various free of cost, quality tuberculosis diagnosis and treatment services across the country through the government health system. Pradhan Mantri TB Mukh Bharat Abhiyan (Prime Ministers TB Free India Program) was launched in India to provide additional nutritional support to those on TB treatment. Patients with TB would receive Rs 500 (\$8) a month for food.

The International Union Against Tuberculosis and Lung Disease (The Union) is the world's first scientific global health organization, founded in 1920, a leader in ending TB and HIV. The Union provides project implementation, operations research, technical support, and capacity building services.

The government of India has also undertaken multiple TB research projects and adopted Artificial Intelligence (AI) for improving the delivery of healthcare.

Conclusion:

India is marching towards a TB free India by 2025 through four strategies of detect, treat, prevent and build in collaborative government and private initiatives. Provision of free TB treatment, nutritional support and direct cash transfers have contributed enormously to the improvement of the situation. Constant research and innovation will contribute to the program expansion.

Situation in paediatric tuberculosis in India

Kushaljit Singh Sodhi presented on behalf of AOSPR, stated that as per the WHO estimates, every year, 10 million people fall ill with tuberculosis (TB) and nearly 1.5 million people die from TB each year, making it the world's top infectious killer [5].

The South and Southeast Asian regions have the highest number of TB estimates in the entire world, bearing nearly half of the global burden of TB disease [5]. It is now evident that five of the global high TB burdened countries are in these regions, which include India, Indonesia, Bangladesh, Myanmar and Thailand. They also account for the highest TB case fatality ratio, along with the African region. As per WHO 2022 report, 82% of global TB deaths among HIV-negative people occurred in the African and Southeast Asian regions.

A new imaging approach and future directions in TB imaging include the use of mediastinal ultrasound (US), Magnetic Resonance Imaging (MRI) and Artificial Intelligence (AI).

US imaging offers several advantages for the diagnosis of thoracic tuberculosis in children. It does not involve any radiation, is easily available, affordable, obviates need for sedation and can be performed at the bedside (portable). It is useful in the detection and characterisation of pleural effusion and in guiding aspiration and drainage procedures.

Mediastinal US has been proposed as an alternative to CXR in the detection of mediastinal lymph nodes, specifically in resource limited settings where US might be the only imaging modality [7]. A suprasternal approach or a parasternal approach can be performed. A study investigating children with pulmonary tuberculosis who had normal chest radiographs found mediastinal lymphadenopathy in 67% of children using US of the mediastinum. Limitations include operator dependence and subjectivity, but these can be overcome with experience and procedural standardization.

In paediatric TB, an enlarged abnormal lymph node is the key imaging finding in making correct and early diagnosis. MRI yields sensitivity, specificity and positive and negative predictive values of 100% for the detection of mediastinal lymph nodes >7 mm in size [8] (Figure 3).

MRI has also demonstrated perfect correlation with multidetector CT in the detection of pulmonary consolidation, nodules (>4 mm), cyst/cavity and pleural effusions [8] (Figure 4). Diffusion Weighted Imaging (DWI) - (restricted diffusion in infected lymph nodes) and contrast enhanced MRI, can demonstrate peripheral enhancement in caseating necrosis confirming the disease activity. Its use in daily clinical practice is limited by cost and availability, especially in low resource settings, but its use is advocated especially in a patient's follow-up at referral and academic centres, especially for a nodal disease.

AI would be especially useful in TB prevalent areas with limited access to radiologists. AI algorithms can be trained to recognize tuberculosis related abnormalities on chest radiographs. Various AI algorithms are available commercially today. Qin ZZ et al [9] evaluated TB detection from chest x rays for triaging in a high tuberculosis burdened setting and evaluated five AI algorithms. All five AI algorithms reduced the number of tests required by 50%, while maintaining a sensitivity above 90%. AI algorithms can be highly accurate and useful triage tools for tuberculosis detection in highly burdened regions, and potentially outperform a human reader.

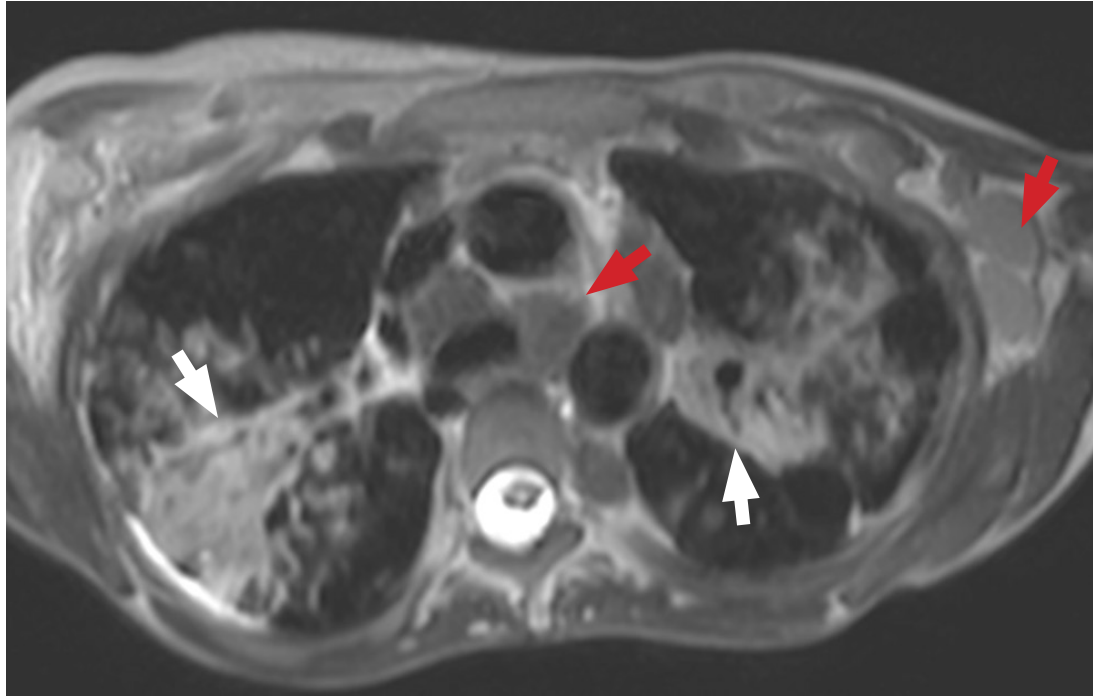


Figure 3. A 10-year-old girl with tuberculosis. Axial T2 TSE image shows areas of consolidation (white arrows) in bilateral lungs with coalescing centrilobular nodules on the right side. In addition, multiple enlarged mediastinal and axillary lymph nodes are also seen (red arrows).

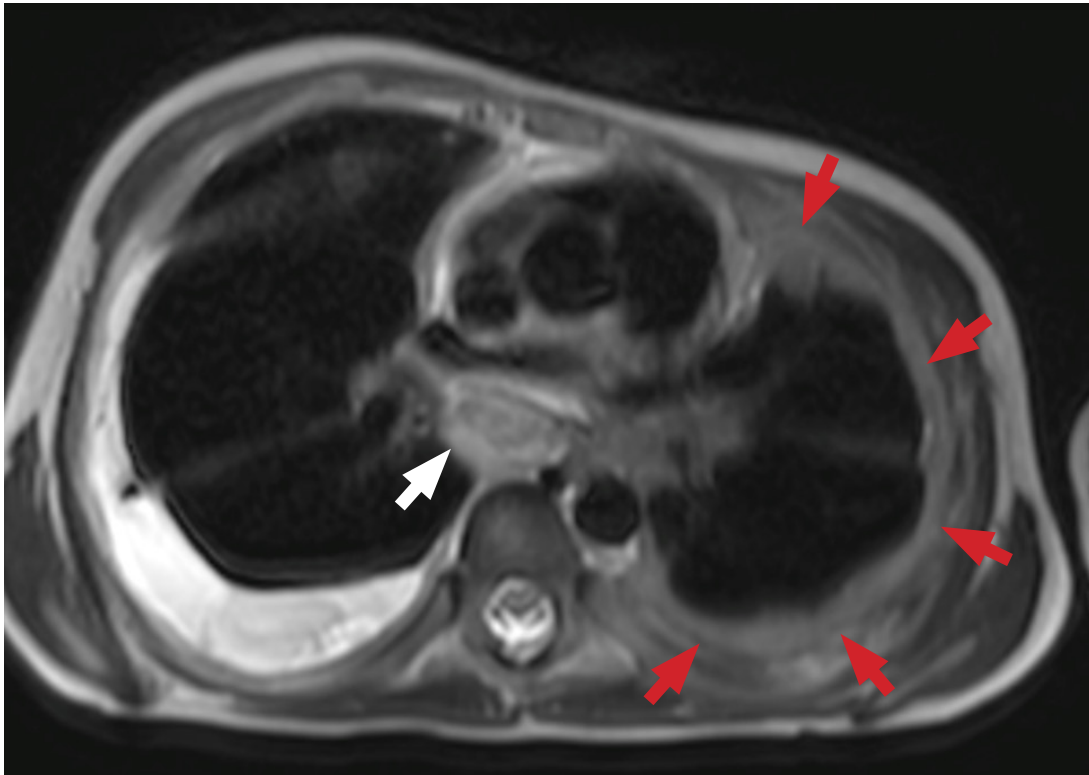


Figure 4. A 11-year-old boy with tuberculosis. Axial T2 TSE image shows a collection in the right pleural cavity. There is presence of an enlarged subcarinal lymph node seen (white arrow) with pleural thickening on the left side (red arrows).

Conclusion:

Tuberculosis still remains the most infectious global disease and fight against tuberculosis should include the optimal use of mediastinal ultrasound, MRI and Artificial Intelligence algorithms, so as to enable to detect and treat it at an earlier stage.

Situation in Korea

Ki Yeol Lee on behalf of the KSTR presented “Situation and Imaging Innovation in TB”.

TB is a serious health problem in the Republic of Korea. In 2021, among the 38 Organizations for Economic Cooperation and Development member countries (OECD), the Republic of Korea ranked highest in TB incidence (49 per 100,000 population) and third highest in TB mortality (3.8 per 100,000 population). The number of multidrug-resistant (MDR) TB cases dropped from 399 in 2020 to 371 in 2021. In 2022, to reduce the TB burden, the Korea Disease Control and Prevention Agency implemented the ‘Measures to Strengthen TB Prevention Management,’ which was established in 2019. To that end, Korea’s goal is to eradicate TB by 2030.

Latent Tuberculosis Infection (LTBI) has been used to define a state of a persistent immune response to stimulation by TB antigens through tests such as the tuberculin skin test (TST) or an interferon- γ release assay (IGRA) without clinically active TB. Recently, the WHO has suggested the removal of the word “latent”, leaving the term “TB infection” only [10, 11].

The spectrum from TB infection to TB disease includes uninfected individuals, TB infection, incipient TB, subclinical TB without signs/symptoms, subclinical TB with unrecognised signs/symptoms, and TB disease with signs/symptoms [11] (Figures 5-8).

A CXR is the first test for diagnosing tuberculosis in patients with respiratory symptoms, but its accuracy is about 49%. Disadvantages of CT are radiation exposure and expensive examination. New imaging modalities, such as ultralow dose CT, dual-energy subtraction digital radiography [12], digital tomosynthesis [13], MRI and tuberculosis diagnosis using deep learning, are also being used.

In 2021, the WHO published guidelines for the screening of TB disease. The new guidance states that among individuals aged 15 years and older in a population in which TB screening is recommended, CAD (computer-aided diagnosis) may be used in place of human readers for interpreting digital chest X-rays for screening and triage for TB disease. In addition, to automatically detect tuberculosis lesions, it is now possible to help determine the activity of pulmonary TB by scoring it [14].

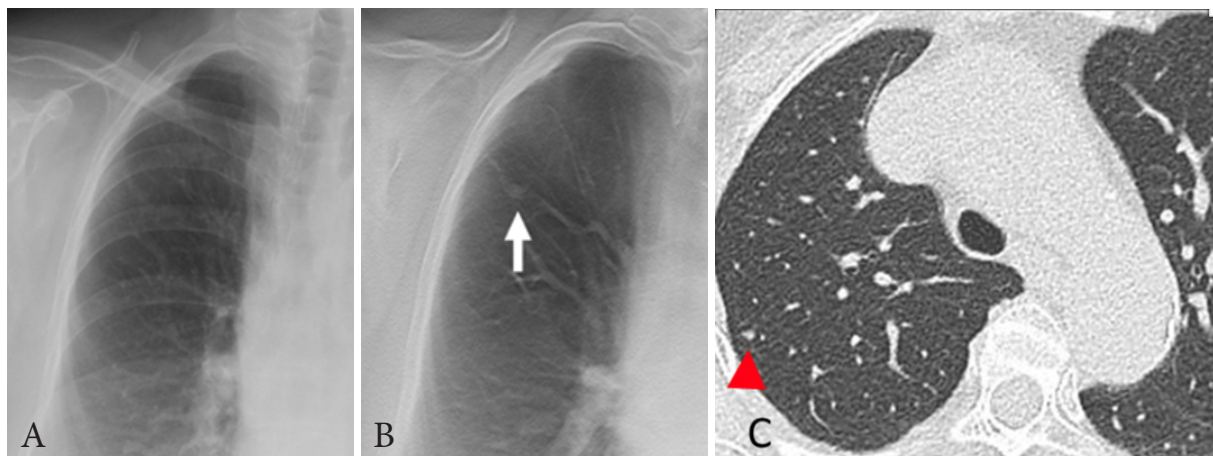


Figure 5. *A case showing tuberculosis spectrum: An asymptomatic 77-year-old female patient underwent contact screening. The chest radiograph is normal (A), but digital tomosynthesis (B) and a CT scan (C) show a small nodule on the right upper lobe. This patient tested positive on her IGRA test. In other words, she had evidence of tuberculosis infection, but she had no evidence of active TB disease clinically, bacteriologically, or radiologically. Therefore, she could be diagnosed with tuberculosis infection. She did not receive a treatment for TB infection because she was an elderly.*

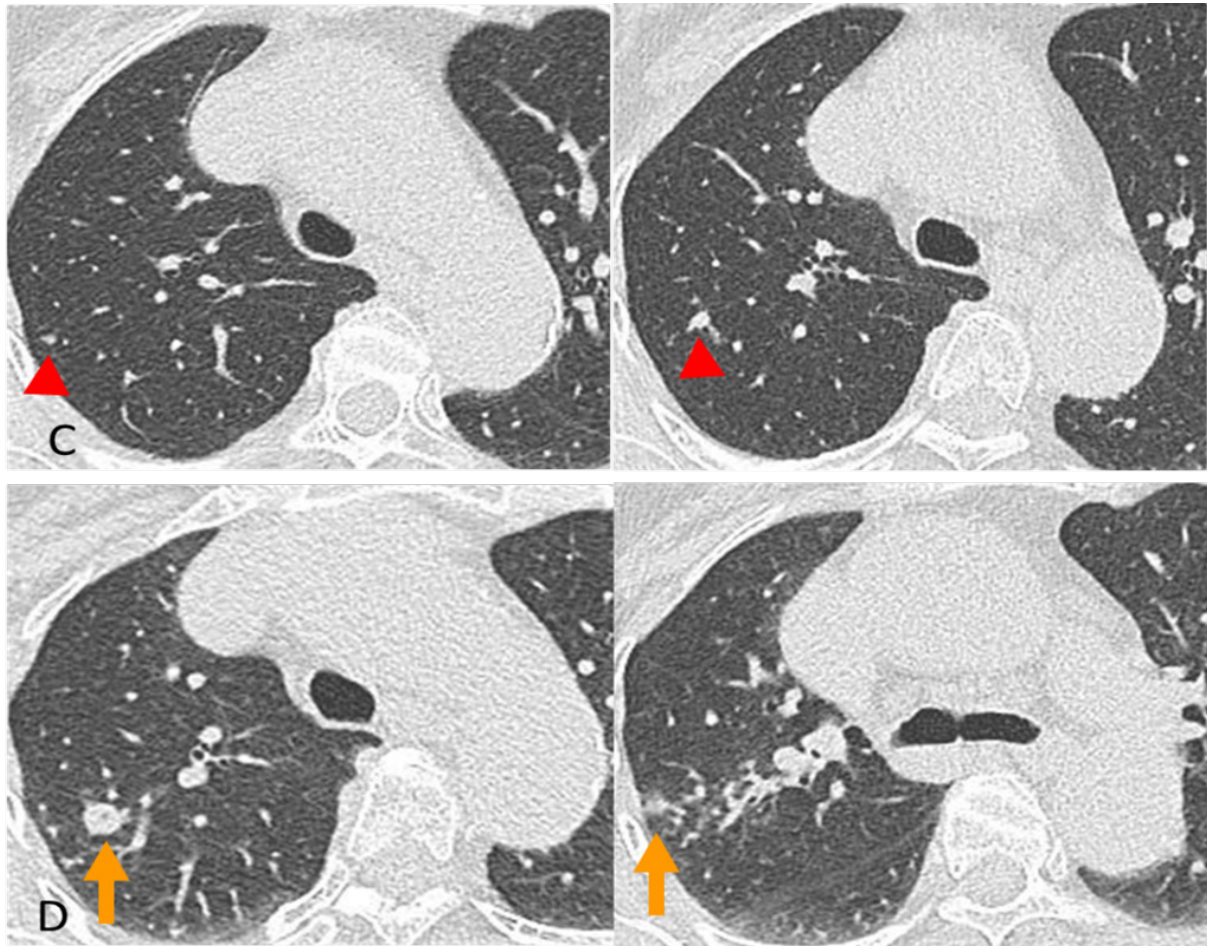


Figure 6. A case showing tuberculosis spectrum: An asymptomatic 77-year-old female patient underwent contact screening. On the CT scan performed 3 months later (D), the existing nodules of the right upper lobe enlarged, and centrilobular nodules and tree-in-bud are newly observed around the nodules of the right upper lobe. In the perspective of the new TB spectrum, this patient's condition can be considered as an incipient TB, in which, without intervention, it may develop into active TB disease in the near future. (Courtesy of Yeon Joo Jeong, Pusan National University Hospital, Korea).

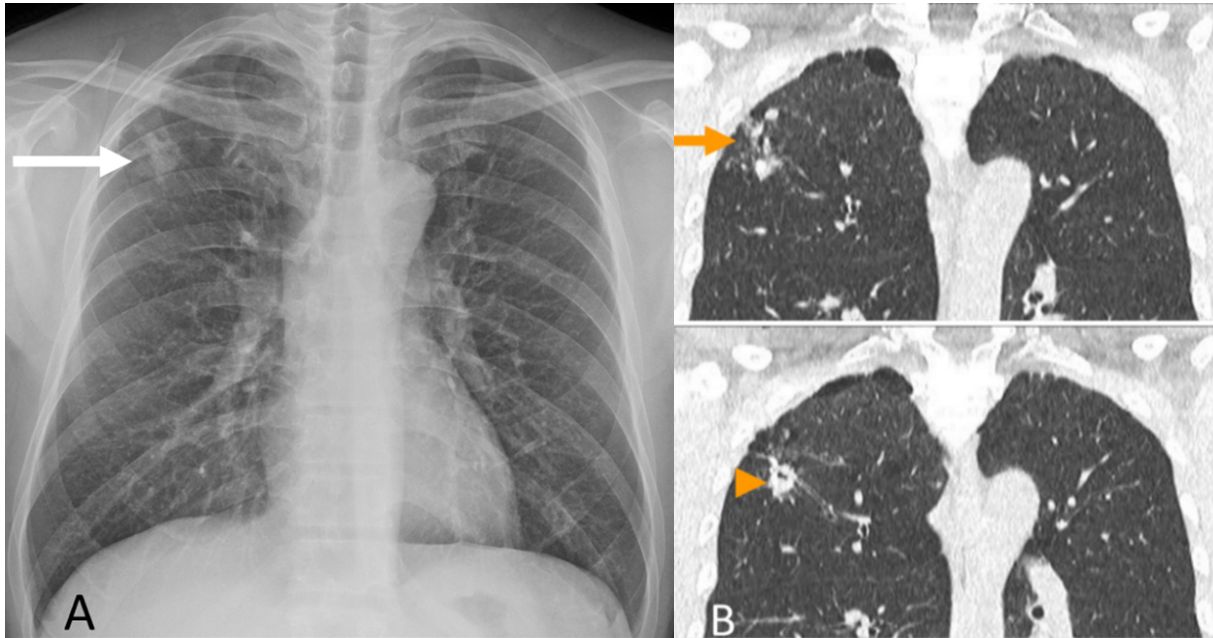


Figure 7. *Detection of subclinical tuberculosis on ultra-low dose CT: 51-year-old male patient diagnosed with rectal cancer and underwent ultra-low dose CT for metastasis work up. A chest radiograph shows ill-defined nodular opacities in the right upper lung zone (arrow, A). An ultra-low dose CT performed on the same day (B) shows small nodules in the right upper lobe (arrow) and a cavitary nodule (arrowhead). This case is subclinical tuberculosis, for which ultra-low dose CT is very useful for diagnosing early tuberculosis.*

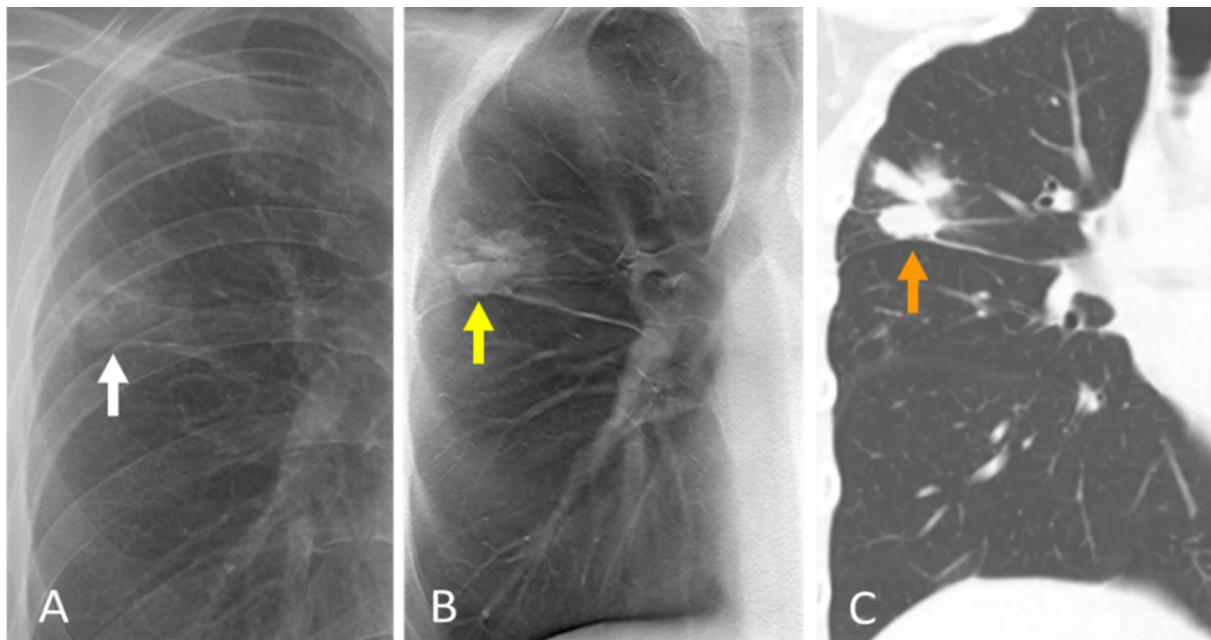


Figure 8. *Detection of patchy consolidation on digital tomosynthesis: a 27-year-old male patient diagnosed with MDR TB. Suspicious focal patchy consolidation is seen in the right upper lung zone on the chest radiograph (arrow in A). The patchy consolidation is more clearly visible on digital tomosynthesis (arrow in B) in the right upper lobe than in the chest radiograph. Coronal chest CT imaging on the same day confirms this lesion as a patchy air-space consolidation in the right upper lobe (C).*

Conclusion:

The evolution of the definition of “tuberculous infection” includes the continuum of stages, existing TB infection and diseases. Recently, the WHO has adopted the term “TB infection” to better denote “a continuum” in the process, which follows inhalation of bacilli and may lead to the clinically manifested TB disease.

Digital tomosynthesis has a promising role for improving the diagnostic accuracy of chest x-rays in the detection of TB. The clinical implementation of an optimized MRI protocol with the motion correction technique is feasible for imaging pulmonary TB. In addition, automated detection of TB in chest x-rays may facilitate screening and evaluation efforts in TB prevalent areas that are difficult to access by radiologists.

Acknowledgements

This paper was prepared by Professors Mini Pakkal and Jin Mo Goo, Chairperson(s) of the Asian Symposia Asian I: Situation and Imaging Innovation in Tuberculosis, with the support of Associate Professor Wiwatana Tanomkiat, scientific chair of AOCR2023 on the basis of the presentations and summary reports delivered at the symposia by:

- a. Professor Bushra Johari, representing the College of Radiology, Academy of Medicine of Malaysia (COR, AMM),
- b. Professor Kushaljit Singh Sodhi, Professor, Department of Radio diagnosis & Imaging, Post Graduate Institute of medical education & Research, Chandigarh, India represented the Asian Oceanic Society of paediatric radiology (AOSPR),
- c. Professor L Murali Krishna presented on behalf of the Indian Radiological & Imaging Association and
- d. Professor Ki Yeol Lee, Korea University Medicine on behalf of the Korean Society of Thoracic Radiology Ki Yeol Lee, M.D., Ph.D., Korea University Medicine on behalf of the Korean Society of Thoracic Radiology.

The paper was provided to the presenters for feedback. It was approved by Associate Professor Wiwatana Tanomkiat, scientific chair of AOCR on 14th August 2023.

References

1. Malaysian Health Technology Assessment Section (MaHTAS), Medical Development Division, Ministry of Health Malaysia. Clinical Practice Guidelines: Management of Tuberculosis. 4th ed. Putrajaya, Malaysia: Federal Government Administrative Centre; 2021 [cited 2023 Aug 15]. Available from: <http://www.moh.gov.my>.
2. Nachiappan AC, Rahbar K, Shi X, Guy ES, Mortani Barbosa EJ Jr, Shroff GS, et al. Pulmonary Tuberculosis: Role of Radiology in Diagnosis and Management. *Radiographics* 2017;37:52-72. doi: 10.1148/rg.2017160032.
3. Khvilivitzky K, Trivedi PN, McFadden PM. Tuberculous tracheobronchial stenosis: avoiding resection-when less is more. *J Thorac Dis* 2017;9:E779-82. doi: 10.21037/jtd.2017.08.104.
4. Neke NS. Endobronchial tuberculosis: an overview. *Ann Pak Inst Med Sci [Internet]*. 2013 [cited 2023 Aug 15];9:105-9. Available from: <https://www.pakmedinet.com/28727>.
5. The WHO Global Tuberculosis Report 2022 [Internet]. Geneva: WHO; 2023 [cited 2023 Aug 15]. Available from: <https://www.who.int/teams/global-tuberculosis-programme/tb-reports/global-tuberculosis-report-2022>.
6. Ministry of Health and Family Welfare, Government of India [Internet]. India TB Report 2022 . New Delhi: Central TB Division; 2022 [cited 2023 Aug 15]. Available from: <http://tbcindia.gov.in/WriteReadData/IndiaTBReport2022/TBAnnulReport2022.pdf>.
7. Bosch-Marcet J, Serres-Créixams X, Borrás-Pérez V, Coll-Sibina MT, Guitet-Juliá M, Coll-Rosell E. Value of sonography for follow-up of mediastinal lymphadenopathy in children with tuberculosis. *J Clin Ultrasound* 2007; 35:118-24. doi: 10.1002/jcu.20304.

8. Sodhi KS, Khandelwal N, Saxena AK, Singh M, Agarwal R, Bhatia A, et al. Rapid lung MRI in children with pulmonary infections: Time to change our diagnostic algorithms. *J Magn Reson Imaging* 2016;43:1196-206. doi: 10.1002/jmri.25082.
9. Qin ZZ, Ahmed S, Sarker MS, Paul K, Adel ASS, Naheyan T, et al. Tuberculosis detection from chest x-rays for triaging in a high tuberculosis-burden setting: an evaluation of five artificial intelligence algorithms. *Lancet Digit Health* 2021;3:e543-54. doi: 10.1016/S2589-7500(21)00116-3.
10. World Health Organization. WHO operational handbook on tuberculosis. Module 1: prevention . tuberculosis preventive treatment. Geneva: WHO; 2020.
11. Migliori GB, Ong CWM, Petrone L, D'Ambrosio L, Centis R, Goletti D. The definition of tuberculosis infection based on the spectrum of tuberculosis disease. *Breathe (Sheff)* 2021;17:210079. doi: 10.1183/20734735.0079-2021.
12. Sharma M, Sandhu MS, Gorski U, Gupta D, Khandelwal N. Role of digital tomosynthesis and dual energy subtraction digital radiography in detection of parenchymal lesions in active pulmonary tuberculosis. *Eur J Radiol* 2015; 84:1820-7. doi: 10.1016/j.ejrad.2015.05.031.
13. Mok J, Yeom JA, Nam SW, Yoo JM, Lee JW, Lee G, et al. Role of digital tomosynthesis in the context of tuberculosis contact investigation: comparisons with digital radiography. *Acta Radiol* 2022; 63:901-8.
14. Lee S, Yim JJ, Kwak N, Lee YJ, Lee JK, Lee JY, et al. Deep learning to determine the activity of pulmonary tuberculosis on chest radiographs. *Radiology* 2021;301:435-42. doi: 10.1148/radiol.2021210063.



Memorial

Received 21 August 2023 ; accepted 22 August 2023
doi:10.46475/aseanjr.v24i2.872

Professor Emeritus Chaleow Piyachon, 1938-2023

Professor Emeritus Chaleow Piyachon passed away on May 27, 2023, following an arduous struggle from complications of appendicitis and septicaemia. Professor Piyachon was born in 1938 in the central province of Singburi, Thailand. He graduated from Chulalongkorn University Hospital before receiving radiology training in the School of Medicine, University of Pittsburgh, USA.

After completion of the radiology programme, Professor Piyachon returned to Thailand, Bangkok and then to Chiang Mai, where he served as an instructor in the early days of Department of Radiology, Faculty of Medicine, Chiang Mai University. He was promoted as the head of the department, subsequent to the title of Director of Maharaj Nakorn Chiang Mai Hospital and Director of the Northern Thai Cancer Foundation, the latter position which he held until his final days. His academic achievements spanned from his devoting lessons, well-known textbooks, and numerous research papers. His particular interest was directed toward angiography, cardiovascular imaging, and emergency radiology.



Professor Chaleow Piyachon (left) with his son (right) and grandson (middle)

Apart from the great depths in radiologic interests, his leisure time had been spent profoundly on the domain of art, craft and architecture, particularly that of Northern Thailand. He was involved in various books regarding Northern Thai or Lanna culture, as an author and photographer. Consequently, Chiang Mai University acknowledged his passion and contribution by appointing him as the Head of the University's Centre for the Promotion of Arts and Culture for a while. He was also an enthusiast in watercolour, oil painting, gardening, archaeology, and alternative medicine.

His legacies have been inherited by his cherished pupils and colleagues, along with his family for generations after. Professor Piyachon married Mrs. Nuanjan Wibulsanti and was a father of three sons. He was and is always the best grandfather of two boys, one who has been following his footsteps by pursuing the career in diagnostic radiology at the moment.

This article serves as commemorative statement from our society to the Professor Piyachon's contribution to the radiologic academia, his perseverance toward the medical career, and his unwavering passion.

Pavarit Piyachon, M.D.

ASEAN

This journal provide 4 areas of editorial services: language editing, statistical editing, content editing, and complete reference-citation check in 8 steps:

Step	Services to authors	Services providers
I	Manuscript submitted	Editor
II	Language editing/ A reference-citation check	Language consultant/Bibliographer
III	First revision to ensure that all information remains correct after language editing	Editor
IV	Statistical editing	Statistical consultant
V	Content editing*	Three reviewers
VI	Second revision	Editor
VII	Manuscript accepted/ rejected	Editor/Editorial board
VIII	Manuscript published	Editorial office

*Content editing follows a double-blind reviewing procedure

JOURNAL OF RADIOLOGY